



**POLITECNICO
DI TORINO**

MASTER OF SCIENCE THESIS

Development and validation of a NG-H₂ engine numerical model embedding detailed chemistry in Converge

Author: LUCA FERRETTI

Supervisors:

Daniela Misul

Mirko Baratta

Rainer Rothbauer

Torino, 18/11/2018

Alla mia famiglia che mi ha
sempre supportato

Table of Contents

1. Abstract.....	6
2. What is CFD?.....	7
2.1 Introduction	7
2.2 Basic Concepts of Fluid Flow	8
2.2.1 Introduction	8
2.2.2 Continuity equation.....	9
2.2.3 Momentum equation	10
2.2.4 Energy Equation	12
2.2.5 Equation of State.....	13
2.3 The Numerical Method	14
2.3.1 Discretization Approaches	15
Finite Element Method	15
Finite Volume Method	15
Finite Difference Method	15
2.4 Turbulence Modelling	17
2.4.1 Reynolds-Averaged-Navier-Stokes (RANS) Equations.....	18
2.5 CFD Software Used (CONVERGE)	21
2.5.1 Grid Control	22
Grid Scaling	22
Fixed Embedding.....	22
Adaptive Mesh Refinement (AMR)	23
3. Experimental Data Analysis.....	25
3.1 Introduction	25
3.2 Engine Characteristics.....	25
3.2.1 Fuel Supply	26
3.3 Experimental Data Treatment.....	27
3.3.1 Trapped Mass Problem.....	27
3.3.2 Heat Release Rate (HRR).....	28
3.3.3 Integrated Heat Release (IHR).....	29
3.3.4 Statistic Methods	30
3.4 Operating Points Considered	31
3.4.1 Operating point 4600x7.9x1 CH ₄	31
3.4.2 Operating point 4600x7.9x1 CH ₄ +H ₂	32

3.4.3 Operating point 2000x14x1 CH ₄	33
4. The Model.....	35
4.1 Regions and Geometry	35
4.2 Boundary Conditions	38
4.3 Regions Initialisations.....	39
4.5 Combustion Modelling.....	39
4.5.1 Chemical kinetics.....	40
4.6 CONVERGE Combustion Models	42
4.6.1 SAGE Details Chemistry Kinetic Solver	42
4.7 Chemical Reaction Mechanisms	44
4.7.1 GRI-Mech 3.0	44
4.7.2 USC-Mech II	47
4.8 Ignition Modelling: Source and Sink	48
4.9 Turbulence Modelling	50
4.9.1 k - ϵ Models.....	51
Standard and RNG k - ϵ Models	51
4.10 Mesh Settings.....	53
4.10.1 Base Mesh Settings.....	53
4.10.2 Fixed Embedding Settings	53
4.10.3 Adaptive Mesh Refinement Settings	53
5. Results.....	55
5.1 Introduction	55
5.2 Operating point 4600x7.9x1 (NG).....	55
5.2.1 Base Simulation.....	56
5.2.2 Boundary Conditions Manipulation.....	58
5.2.3 Mesh Sensitivity	61
AMR Sub Grid Criterion Velocity equal to 2	61
AMR Sub Grid Criterion Velocity equal to 1 m/s	63
Comparisons	64
5.2.4 Schmidt Number Sensitivity.....	68
Schmidt Number Equal to 0.75.....	69
Schmidt Number Equal to 0.70.....	71
Comparisons	73
5.2.5 Reaction Multiplier Sensitivity	75

SAGE Reaction Multiplier Equal to 1.05.....	75
SAGE Reaction Multiplier Equal to 1.1.....	77
Comparisons	79
5.2.6 LHV Correction	80
5.3 Operating Point 4600x7.9x1 (NG+15%H₂).....	83
5.3.1 Base Simulation.....	83
5.3.2 New Reaction Mechanism: USC Mech	85
5.3.3 Boundary Conditions Manipulation.....	87
5.3.4 LHV Sensitivity	89
LHV Equal to 54 MJ/kg	90
LHV equal to 55 MJ/kg	92
LHV equal to 56 MJ/kg	94
Comparisons	96
5.4 Operating Point 2000x14x1 (NG).....	98
5.4.1 Base Simulation.....	98
5.4.2 New Boundary Conditions	101
5.4.3 Schmidt Number Sensitivity.....	103
Schmidt Number equal to 0.75.....	103
Schmidt Number equal to 0.70.....	105
Comparison	107
5.4.4 LHV Correction	108
6. Conclusion and Future Developments.....	111
Acknowledgment.....	113
Acronyms.....	114
List of Figures.....	116
List of Tables.....	120
Bibliography.....	121

1. Abstract

This thesis project is a combustion modelling study and development of a natural gas engine by means of a CFD (*Computational Fluid Dynamics*) software called CONVERGE. The sophisticated software used, introduced a new concept of automatic mesh generation, useful to save time, with a complex code which can also refine the grid locally basing on particular rules. The project supports an European research, named *Gas-on*, with the specific aim to reduce the engine emissions trough the usage of alternative fuels, such as methane (CH_4) and methane with the addition of percentages of hydrogen (H_2), in order to reduce the carbon pollutant generated by engines. The thesis project, with the consequential model validation, has been carried out at the CFD company *Convergent Science GmbH* in Austria and all the experimental data has been provided by the *Politecnico di Torino* university, especially from the DENERG laboratory of the university itself. The project itself is a model validation of the *FIAT FIRE 1.4 16V Turbo CNG* engine focusing on the SAGE Detailed Chemistry combustion model by means the usage of specific reaction mechanisms that fit perfectly the reactions accomplished by the oxidation of the methane, or methane with the addition of percentage of hydrogen, in air. The thesis can be subdivided in two main parts according with the topic that is being discussed. The first part is a review of all the fluid governing equations, with which the software computes the results of each simulation, and a brief description of how the software and the automatic mesh generation work in order to give some technical information regarding the base concepts on which the software is based on and the user-friendly usage of the CONVERGE interface. In the second part all the results obtained will be shown and described in detail with a particular focus on the modifications carried out in order to obtain the model validation. This second part can be also split in two parts where the former is a model validation of two specific engine operating points with the usage of the NG fuel and the latter is a model validation of one of these two operating points with the addition of a 15% of hydrogen in the fuel composition.

2. What is CFD?

2.1 Introduction

Computational fluid dynamics or CFD is a branch of fluid mechanics that use numerical analysis and data structure to solve and analyze problems that involve fluid flows, heat transfer and associated phenomena such as chemical reactions. Computers are used to perform the calculations required to simulate the interaction of liquids and gases with surfaces defined by boundary conditions.

From the 1960 the aerospace industry has integrated CFD technique into their design for the simulation of jet engines and the manufacture of the aircraft. More recently, on account of the development of the calculation power of computers, the method has been applied also to the design of internal combustion engines (ICE), turbines and furnaces. Nowadays, the CFD method is more popular and it is becoming a fundamental tool in the design of industrial products and processes.

Moreover, there are numerous advantages of CFD approach to fluid system design, such as ability to study systems where the experiments are difficult or impossible to perform, ability to study systems with very hazardous conditions or more than the normal performance limits, considerable reduction of lead times and costs of new design and practically unlimited level of details of results.

CFD codes usually are made by numerical algorithms that can deal with fluid flow problems. Furthermore, all the commercial CFD software include sophisticated interfaces for the users to make the input problems parameters simple and to examine the results.

All the codes generally are structured by three main elements:

- **Pre-processor:** it consists in an operator-friendly interface where it is easy to insert the inputs of a flow problem and the succeeding transformation of these inputs in an appropriate format for the solver. The activities allowed in the pre-processor interface are many, such as definition and/or modification of the geometry, grid generation (or the subdivision of the domain in a number of smaller sub-domains), definition of fluid properties, selection of the physical and chemical phenomena that are going to be modelled and specification of appropriate boundary conditions.
- **Solver:** it is structured by three main steps with which it solves the equations of the fluid problem, such as integration of the governing equations of fluid flow, discretisation of the domain transforming the integral equations into a system of algebraic equations and solution of these equations by an iterative method. There are three distinct streams of numerical solution techniques: *finite differences method*, *finite element method* and *finite volume method*.
- **Post-processor:** it makes the result visualisation and analysis easy for the user and the main characteristics that are implemented on are: vector plots, domain geometry and grid display, 2D and 3D surface plots and view manipulation.

Before going deeper on the thesis project, the governing equations of a CFD code will be described.

[1]

2.2 Basic Concepts of Fluid Flow

2.2.1 Introduction

In physics, a fluid is a substance that continually deform (flows) under an applied shear stress. Fluids are a subset of the phases of matter and include liquids, gases, plasma and some types of plastic solid. Fluids are substances that have zero shear module, or, in simpler terms, a fluid is a substance which cannot resist any shear force applied to it. Although the term “fluid” includes both the liquid and the gas phases and they follow the same laws of motions, there are still several differences between them.

The main forces that cause a fluid flow are gravity, rotation, shear, surface tension and pressure differences. Usually they are associated to two fundamental forces: *surface forces* (e.g. shear force or pressure differences) and *body forces* (e.g. gravity and rotation force).

Although the fluids behaviour is similar between gases and liquids, their microscopical properties differ significantly. The most important proprieties which have a considerable impact on the fluid's characteristics are *density* and *viscosity*, while others, such as Prandtl number, specific heat, and surface tension affects fluids only in certain condition for example where there is a huge difference of temperature. Obviously, fluids proprieties are functions of others thermodynamic variables such as temperature and pressure. At the same time, fluid flow is likewise able to influence these variables, for example the speed: if the system has a low speed, laminar flow occurs where the inertia of the fluid is not taken in account because of a low value; on the other hand, if the system has a high velocity the inertia becomes important and the particles start to follow random rules of motion transforming the laminar flow in a turbulent flow. Usually the transition between laminar and turbulent flow is defined by the Reynolds number that is a ratio between the inertia factor and the viscosity factor. If the inertia factor is preponderant, and consequently the Reynolds number is high, the particles has a random motion and we can obtain a turbulent flow, otherwise if the viscosity factor has a more important impact, the Reynolds number has a low value and we can obtain a laminar flow. Another important variable needed during a flow study is the Mach number: it is a ratio between the fluid velocity and the sound velocity in that particular fluid conditions of pressure and temperature. It is possible to determine five different fluid behaviours considering the Mach number:

1. $Mach < 0.3$ the flow may be considered incompressible;
2. $Mach > 0.3$ the flow may be considered compressible;
3. $Mach < 1$ the flow is subsonic;
4. $Mach > 1$ the flow is supersonic and shock waves are possible to find;
5. $Mach > 5$ the flow is hypersonic and the high velocity can generate high temperatures that affect the fluid chemical properties.

All these properties and distinctions have an important influence on the fluid that they can affect the solution method or the mathematical nature of the problem.

[1]

In the majority of flows the viscosity become an important factor only near the walls, according to that hypothesis the fluids are considered, in the others parts of the domain, as inviscid. There are some different viscosity laws in literature but, in this project thesis, the Newton's law of viscosity has been considered.

The fundamental CFD governing equations are three and they depend on three fundamental physical concepts such as the mass conservation, the second Newton's law ($F = ma$) and energy conservation.

Respectively, the conservation of the mass flow is called *Continuity Equation*, the momentum conservation of a fluid flow is named *Momentum Equation* and the energy conservation of a fluid flow is called *Energy Equation*. Additionally, to make these laws easier for comprehension, it is necessary to describe the relationship between fluid properties such as the equation of state, which considers the thermodynamic variables pressure, density and temperature.

[2]

Finally, before starting with the governing equation description, it is useful to explain the two main approaches that can be found in literature:

- **Lagrangian Approach:** or *Infinitesimal fluid element model*, it is a way to looking at a fluid motion where the observer follows an individual fluid parcel as it moves through the domain (space) and time. It is useful for the study of pollutants or discrete entities such as bubbles, parcels and unburned materials. The equations taking out from the physical principles applied on a control volume, using this approach, are in integral form and they can be manipulated in order to acquire partial differential equations;
- **Eulerian Approach:** or *Finite Control Volume Model*, it is a way to looking at a fluid focuses on specific locations in the domain (space) through which the fluid flows at time passes. Also, with this method, partial differential equation form is easily to obtain directly from the fundamental equations.

2.2.2 Continuity equation

The first method considered is *Eulerian Approach*. Considering a finite control volume Ω and its contour $\partial\Omega$, the mass that evolves in time is defined by:

$$m_{\Omega} = \int_{\Omega} \rho \, dV \quad (2.1)$$

In order to figure the mass flow going in or out from the contour out, a mass variation has been considered, where the flow velocity is v , the elemental surface area vector is dS and the elemental volume inside the finite control volume is dV .

$$\frac{dm_{\Omega}}{dt} = - \int_{\Omega} \rho \, v \, dV \quad (2.2)$$

The second term is negative because if the system has a positive fluid flow, the mass variation tends to decrease in the control volume.

Applying the divergence theorem to the mass variation equation, we obtain the continuity equation:

$$\frac{\partial \rho}{\partial t} + \nabla \cdot (\rho v) = 0 \quad (2.3)$$

Considering the *Lagrangian Approach* the following equation describe the mass variation:

$$\delta m = \rho \, \delta V \quad (2.4)$$

The mass conservation principle asserts that, according to the Lagrangian approach, if the parcel is moving with the flow motion, the mass variation is equal to zero.

$$\frac{D(\delta m)}{Dt} = 0 \quad (2.5)$$

Where the first term is the time rate of change of mass of a fluid while is moving through the space and the time. This kind of derivation is called *substantial derivative*.

Combining the equations 4 and 5, dividing by δV and adding the operator $\nabla \cdot \mathbf{v}$, that physically means the volume time rate of change of a moving fluid, the continuity equation is found:

$$\frac{D\rho}{Dt} + \rho \nabla \cdot \mathbf{v} = 0 \quad (2.6)$$

2.2.3 Momentum equation

The momentum equation is based on the second Newton law, it is a vector equation and it can be written with three scalar relations along the three cartesian axes (x, y, z). As previously mentioned, the forces stakes are *body forces* and *surface forces*. In particular, the body forces are applied on the control volume by distance such as magnetic, gravitational, and electric forces, on the other hand, the surface forces are applied directly on the surface of the fluid element such as pressure forces.

The Lagrangian Approach and the x-axes direction have been taken in account for the momentum equation derivation. Focusing on the second term of the second Newton's law, it can be manipulated as a body force obtaining the following relations:

$$F_x = ma_x \quad (2.7)$$

$$\text{body force}_x = \rho f_x dx dy dz$$

Where $dx dy dz$ is the fluid volume taken in account.

At this point the surface forces are considered and the figure 2.1 shows the force distribution on a fluid element.

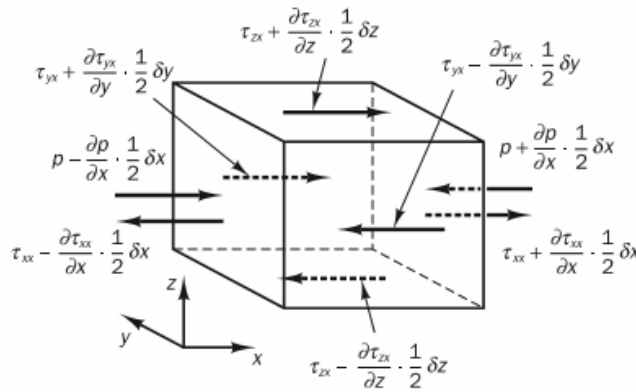


Figure 2.1: Stress components in the x-direction.

The sum along the x-direction on the East and West surfaces is:

$$\begin{aligned} & \left[\left(p - \frac{\partial p}{\partial x} \frac{1}{2} \delta x \right) - \left(\tau_{xx} - \frac{\partial \tau_{xx}}{\partial x} \frac{1}{2} \delta x \right) \right] \delta x \delta z + \left[- \left(p + \frac{\partial p}{\partial x} \frac{1}{2} \delta x \right) + \left(\tau_{xx} + \frac{\partial \tau_{xx}}{\partial x} \frac{1}{2} \delta x \right) \right] \delta y \delta z \\ & = \left(- \frac{\partial p}{\partial x} + \frac{\partial \tau_{xx}}{\partial x} \right) \delta x \delta y \delta z \end{aligned} \quad (2.8.a)$$

The net force in the x-direction on the North and South surfaces is:

$$-\left(\tau_{xy} - \frac{\partial \tau_{xy}}{\partial y} \frac{1}{2} \delta y\right) \delta x \delta z + \left(\tau_{yx} + \frac{\partial \tau_{yx}}{\partial y} \frac{1}{2} \delta y\right) \delta x \delta z = \frac{\partial \tau_{yx}}{\partial y} \delta x \delta y \delta z \quad (2.8.b)$$

And the force in the x-direction on the Top and Bottom surfaces is:

$$-\left(\tau_{zx} - \frac{\partial \tau_{zx}}{\partial z} \frac{1}{2} \delta z\right) \delta x \delta y + \left(\tau_{zx} + \frac{\partial \tau_{zx}}{\partial z} \frac{1}{2} \delta z\right) \delta x \delta y = \frac{\partial \tau_{zx}}{\partial z} \delta x \delta y \delta z \quad (2.8.c)$$

Where τ_{xx} is the shear stress in the x-direction, while τ_{xy} and τ_{zx} are the stresses in the other directions.

The total force per unit volume can be obtained summing the 2.8.a, 2.8.b and 2.8.c divided by the volume $\delta x \delta y \delta z$:

$$\frac{\partial(-p + \tau_{xx})}{\partial x} + \frac{\partial \tau_{yx}}{\partial y} + \frac{\partial \tau_{zx}}{\partial z} \quad (2.9)$$

Now the body forces are possible to add; focusing on the second term of the equation 2.7, the surface forces previously deviated are allowed to sum:

$$F_x = \left(-\frac{\partial p}{\partial x} + \frac{\partial \tau_{xx}}{\partial x} + \frac{\partial \tau_{yx}}{\partial y} + \frac{\partial \tau_{zx}}{\partial z}\right) dx dy dz + \rho f_x dx dy dz \quad (2.10)$$

Furthermore, the mass of the fluid element is fixed making possible substitute: the mass as $m = \rho dx dy dz$ and the acceleration as the time rate of change of the fluid velocity, obtaining:

$$ma_x = \rho dx dy dz \cdot \frac{Dv}{Dt} \quad (2.11)$$

Where $\frac{Dv}{Dt}$ is a substantial derivative according to the Lagrangian Method considered.

Finally, combining the equations 2.11, 2.10 and 2.7 the x-direction term of the momentum equation is obtained:

$$\rho \frac{Dv_x}{Dt} = \frac{\partial(-p + \tau_{xx})}{\partial x} + \frac{\partial \tau_{yx}}{\partial y} + \frac{\partial \tau_{zx}}{\partial z} + \rho f_x \quad (2.12.a)$$

For the other direction (y and z), the same procedure has been followed and it has been obtained respectively:

$$\rho \frac{Dv_y}{Dt} = \frac{\partial(-p + \tau_{yy})}{\partial y} + \frac{\partial \tau_{xy}}{\partial x} + \frac{\partial \tau_{zy}}{\partial z} + \rho f_y \quad (2.12.b)$$

$$\rho \frac{Dv_z}{Dt} = \frac{\partial(-p + \tau_{zz})}{\partial z} + \frac{\partial \tau_{xz}}{\partial x} + \frac{\partial \tau_{yz}}{\partial y} + \rho f_z \quad (2.12.c)$$

The momentum equation can also be written in a compact form:

$$\rho \frac{Dv}{Dt} = \rho f + \nabla \cdot P_{ij} \quad (2.13)$$

Where P_{ij} is called stress tensor, which is a representative matrix of all the applied forces per unit volume to the control volume and it contain the normal and the shear stresses.

[1]

2.2.4 Energy Equation

“The Energy Equation is derived by the *first law of thermodynamics*, which asserts that the rate of change of energy of a fluid particle is equal to the rate of heat addition to the fluid particle plus the rate of work done on the particle. “[1]

Considering a finite control volume Ω and its contour $\partial\Omega$, the scalar total energy is considered as a sum of all the mechanical energies. The first law of thermodynamics can be written as:

$$\frac{\partial E_t}{\partial t} + \nabla \cdot E_t v = \frac{\partial Q}{\partial t} - \nabla \cdot q + \rho f + \nabla \cdot (P_{ij} \cdot v) \quad (2.14)$$

Where, on the left hand side there are the rate of total energy on the control volume and the energy lost by convection. On the other side there are respectively the rate of heat per unit volume, the rate of heat lost by conduction, the work done by the body forces and the work done by the surface forces.

E_t is the sum of all the mechanical energies per volume unit:

$$E_t = \rho \left(e + \text{potential energy} + \frac{v^2}{2} + \dots \right) \quad (2.15)$$

Where e is the internal energy.

The term $\nabla \cdot q$ is defined by the *Fourier's law* that make a relation between the gradient temperature and the heat through a parameter named *thermal conductivity* λ .

$$q = -\lambda \nabla T \quad (2.16)$$

Extending the equation 2.14 to the Cartesian coordinate system the equation can be written:

$$\begin{aligned} \frac{\partial E_t}{\partial t} - \frac{\partial Q}{\partial t} - \rho(f_x v_x + f_y v_y + f_z v_z) + \frac{\partial}{\partial x}(E_t v_x + p v_x - v_x \tau_{xx} - v_y \tau_{xy} - v_z \tau_{xz} + q_x) \\ + \frac{\partial}{\partial y}(E_t v_y + p v_y - v_x \tau_{xy} - v_y \tau_{yy} - v_z \tau_{yz} + q_y) \\ + \frac{\partial}{\partial z}(E_t v_z + p v_z - v_x \tau_{xz} - v_y \tau_{yz} - v_z \tau_{zz} + q_z) \end{aligned} \quad (2.17)$$

Assuming that just the kinetic and internal energy are noteworthy and by means of the continuity equation the left hand side of the equation 2.14 can be written as:

$$\frac{\partial E_t}{\partial t} + \nabla \cdot E_t v = \rho \frac{D}{Dt} \left(\frac{E_t}{\rho} \right) = \rho \frac{De}{Dt} + \rho \frac{D}{Dt} \left(\frac{v^2}{2} \right) \quad (2.18)$$

Doing a scalar product on the equation 2.13 we can obtain:

$$\rho \frac{Dv}{Dt} \cdot v = \rho f \cdot v + \nabla p \cdot v + \tau_{ij} \cdot v \quad (2.19)$$

Combining the equations 2.18 and 2.19 and substituting into 2.14, it holds:

$$\rho \frac{De}{Dt} + p(\nabla \cdot v) = \frac{\partial Q}{\partial t} - \nabla \cdot q + \nabla \cdot (\tau_{ij} \cdot v) - (\nabla \cdot \tau_{ij}) \cdot v \quad (2.20)$$

The last two terms of the equation above can be combined in one single term that is called dissipation function (Φ). It is useful because it represents, in a fluid transformation due to the viscosity, the rate

of mechanical energy consumed. Furthermore, considering the continuity equation and the enthalpy definition (e.g. $h = e + \frac{p}{\rho}$) the equation 2.20 can be written:

$$\rho \frac{Dh}{Dt} = \frac{Dp}{Dt} + \frac{\partial Q}{\partial t} - \nabla \cdot q + \emptyset \quad (2.21)$$

[8] [7]

2.2.5 Equation of State

The Equation of State, which describes the matter under a given sets of physical conditions, is a relation between two or more state variables.

As previously introduced, the motion of a fluid in three dimensions is described by a system of partial differential equations such as Energy Equation, Momentum Equation and Mass Conservation Equation. This system usually is very difficult or impossible to solve analytically, in fact, at the moment, a general solution does not exist.

Since this system contains five equations governed by thermodynamic variables such as p, T, h and e and the motion field (v_x, v_y, v_z), a relationship between the thermodynamic variables is necessary to find and it can be obtained through the assumption of thermodynamic equilibrium.

Considering a fluid as a perfect gas, which means that the intermolecular forces of the gas are insignificant, the equation of state is the easiest one and it can be written:

$$p = \rho RT \quad (2.22)$$

Where R is the gas constant.

When the fluid considered is under particular condition, such as very high temperature or pressure, the intermolecular forces are not negligible anymore and a new equation of state has to be found. In literature several equations of state are easy to find and each one describes the fluid behaviour in different and extreme condition.

On the other hand, if the fluid considered is a liquid the density variation with pressure or temperature is almost zero and for this reason liquid are called *incompressible fluids*. Without density variation there is no linkage between energy equation, momentum equation and mass conservation equation and it is impossible to find a correlation between the thermodynamic variables. The flow field usually can be solved just considering the mass conservation and the momentum equation and the energy equation can be solved only if the aim of the study is to consider the heat transfer.

[7]

2.3 The Numerical Method

As the chapter above presented, the fluid motion is described by partial differential equations or integro-differential equations which are impossible to solve analytically. In order to obtain the solution from this system numerically, a discretization method, which approximates the differential equations by a system of algebraic equations which can be solved with a computer, is needed. The approximation is applied to small domains in space and/or in time in order to make the results of the numerical solution at discrete position in space and time. Despite the accuracy of experimental data depends on the quality of the tools used, the accuracy of numerical solutions is dependent on the quality of discretization used.

The governing equations are exact but, since their solution is impossible to find, the approximations are unavoidable, especially on some phenomena such as turbulences and combustions where even the numerical solution is not available and a method is needed. Which means that the results will not represent exactly the reality but something that is close enough to be considered as acceptable. During a validation of a model, make a more accurate discretization in some regions is possible and that makes the model more representative of the reality in a particular case. That typically increases the costs in terms of time of the model validation, but compromises are always necessary.

Usually the numerical solution method is characterized by different sections:

- **Mathematical Model (or Functional):** it represents the partial differential equation governing the phenomena studied and the boundary condition of that case. That are exact and they need an approximation to be solved. The equations have to be appropriate to the specific case studied (e.g. turbulent, 2D and 3D).
- **Discretization Method:** as previously introduced, it is the approximation method which describe the partial differential equation with algebraic equations. Several methods are present in literature and the most important are the *Finite Element Method*, the *Finite Difference Method* and the *Finite Volume Method*.
- **Coordinates and Basis Vector System:** There are many types of coordinate that could be used and they can be written in several forms. The main coordinate systems that can be selected are *Cylindrical*, *Cartesian*, *Curvilinear*, *Spherical*, *Orthogonal* or *non-Orthogonal*. In order to choose the coordinate system who fits perfectly the case studied, the flow target is needed to know. The coordinate system also may influence the discretization method and the grid type to be used.
- **Numerical Grid:** The discrete locations at which the variables have to be calculated are defined by the numerical grid which is essentially a discrete representation of the geometric domain on which the problem has to be solved. It divides the solution domain into a finite number of subdomains (elements, control volumes etc.). The main options of grid dimension and shape are the *Structured (regular) Grid* that is subdivided in families with the property that members of a single family do not cross each other and cross the member of the other family only once, *Block-structured Grid* that has two or more level subdivision of solution domain and *Unstructured Grid* that is the most flexible type of grid. The accuracy of the results of a CFD code depends on the number of cells presents in the domain. In short, the higher number of cells is present in the domain, the higher the accuracy of the results will be. Obviously, a big number of cells make the time calculation really high so a compromise between the accuracy and the running time has to be found. With some CFD codes is also possible make a refinement in some regions of the domain in order to have more precise result in that particular region without influence the running time too much.

- **Solution Method:** this method usually makes an action of sequential linearization of the equations in order to make possible their solution with an iterative method.
- **Convergence Criteria:** Finally, one needs to set the convergence criteria for the iterative method. Usually, there are two levels of iterations: inner iterations, within which the linear equations are solved, and outer iterations, that handles the non-linearity and coupling of the equations. Deciding when to stop the iterative process on each level is important, from both the accuracy and efficiency points of view.

[2] [8]

2.3.1 Discretization Approaches

A fundamental topic, that makes the comprehension of the approximation applied on the domain easier, is the discretization. Indeed, the main approaches will be described below.

Finite Element Method

“The domain is broken into a set of discrete volumes or finite elements that are generally unstructured; in 2D, they are usually triangles or quadrilaterals, while in 3D tetrahedra or hexahedra are most often used. The main feature of this method is that the equations are multiplied by the weigh function before they are integrated over the entire domain. In the simplest *Finite Element Methods*, the solution is approximated by a linear shape function within each element in a way that guarantees continuity of the solution across element boundaries. Such a function can be constructed from its values at the corners of the elements. The weight function is usually of the same form. This approximation is then substituted into the weighted integral of the conservation law and the equations to be solved are derived by requiring the derivative of the integral with respect to each nodal value to be zero; this corresponds to selecting the best solution within the set of allowed functions (the one with minimum residual). The result is a set of non-linear algebraic equations. An important advantage of finite element methods is the ability to deal with arbitrary geometries; there is an extensive literature devoted to the construction of grids for finite element methods. The grids are easily refined; each element is simply subdivided. Finite element methods are relatively easy to analyse mathematically and can be shown to have optimality properties for certain types of equations”. [2]

Finite Volume Method

“The *Finite Volume Method* is similar to the *Finite Element Method* in many ways. This method uses the integral form of the conservation equations as its starting point. The solution domain is subdivided into a finite number of contiguous control volumes, and the conservation equations are applied to each of them. At the centroid of each control volume lies a computational node at which the variable values are to be calculated. Interpolation is used to express variable values at the control volume surface in terms of the nodal values. Surface and volume integrals are approximated using suitable quadrature formulae. As a result, one obtains an algebraic equation for each control volume, in which a number of neighbour nodal values appear. The *Finite Volume Method* can accommodate any type of grid, so it is suitable for complex geometries. The grid defines only the control volume boundaries and need not be related to a coordinate system”. [2]

Finite Difference Method

“The *Finite Difference Method* is the easiest method to use for simple geometries. The starting point is the conservation equation in differential form. The solution domain is covered by a grid. At each grid point, the differential equation is approximated by replacing the partial derivatives by approximations

in terms of the nodal values of the functions. The result is one algebraic equation per grid node, in which the variable value at that and a certain number of neighbour nodes appear as unknowns. In principle, the FD method can be applied to any grid type. However, in all applications of the *Finite Difference Method* known has been applied to structured grids. The grid lines serve as local coordinate lines. Taylor series expansion or polynomial fitting is used to obtain approximations to the first and second derivatives of the variables with respect to the coordinates. On structured grids, this method is very simple and effective. The disadvantage of *Finite Difference Methods* is that the conservation is not enforced unless special care is taken. Also, the restriction to simple geometries is a significant disadvantage in complex flows". [2]

2.4 Turbulence Modelling

As previously introduced, the turbulence is a fundamental factor on the description and on the study of a fluid flow problem. It is based on the *Reynolds Number*, who is defined as a ratio between the inertia factor and the viscosity factor. It can be written as the following relation:

$$Re = \frac{u \cdot l}{\nu} \quad (2.23)$$

With the *Reynolds Number*, we can describe the transition between two different kind of fluid flow: *Laminar* and *Turbulent*.

A *Laminar flow* is obtained when the particles are adjacent to the walls following the same direction of the pipe or the surface where the flow is going through.

Conversely, a *Turbulent flow* is found when the particles have a random behaviour and the perfect description of the position and the motion of that particles is almost impossible.

The transition between these two kind of fluid motions is defined by critical Reynolds Number value (Re_{cr}). Generally speaking, if the inertia factor (Reynolds Number numerator) is preponderant, which means that the Reynolds Number value is above instead the critical one, the particles have a chaotic and unpredictable motion. On the other hand, if the viscosity factor (Reynolds Number denominator) is more important, the particles have an adjacent motion to the walls with the consequence to be described perfectly by the mass conservation equation.

“In literature are present many proprieties of a turbulent flow, the most important are:

- Turbulent flows are highly unsteady. A plot of the velocity as a function of time at most points in the flow would appear random to an observer unfamiliar with these flows.
- They are three-dimensional. The time-averaged velocity may be a function of only two coordinates, but the instantaneous field fluctuates rapidly in all three spatial dimensions.
- They contain a great deal of vorticity. Indeed, vortex stretching is one of the principal mechanisms by which the intensity of turbulence is increased.
- Turbulence increases the rate at which conserved quantities are stirred. Stirring is a process in which parcels of fluid with differing concentrations of at least one of the conserved properties are brought into contact. The actual mixing is accomplished by diffusion. Nonetheless, this process is often called *turbulent diffusion*.
- By means of the processes just mentioned, turbulence brings fluids of differing momentum content into contact. The reduction of the velocity gradients due to the action of viscosity reduces the kinetic energy of the flow; in other words, mixing is a dissipative process. The lost energy is irreversibly converted into internal energy of the fluid.
- It has been shown in recent years that turbulent flows contain coherent structures-repeatable and essentially deterministic events that are responsible for a large part of the mixing. However, the random component of turbulent flows causes these events to differ from each other in size, strength, and time interval between occurrences, making study of them very difficult.
- Turbulent flows fluctuate on a broad range of length and time scales. This property makes direct numerical simulation of turbulent flows very difficult.”[2]

In order to predict the complex turbulent behaviour, scientist and engineers developed several turbulent mathematical models useful to approximate the differential equations system. By means the turbulent models, the results have not to be too far from the reality otherwise they would not be acceptable. To make it possible, there are different models that fit just on some particular cases but a general one does not exist yet. These turbulent models can be subdivided in six categories and most of which can be divided in sub-categories.

- “The first involves the use of correlations such as ones that give the friction factor as a function of the Reynolds number or the Nusselt number of heat transfer as a function of the Reynolds and Prandtl numbers. This method, which is usually taught in introductory courses, is very useful but is limited to simple types of flows, ones that can be characterized by just a few parameters. Since it can be applied only to simple cases, this method does not need the power calculation of a computer to be solved.
- The second uses integral equations which can be derived from the equations of motion by integrating over one or more coordinates. Usually this reduces the problem to one or more ordinary differential equations which are easily solved. The methods applied to these equations are those for ordinary differential equations.
- The third is based on equations obtained by averaging the equations of motion over time (if the flow is statistically steady), over a coordinate in which the mean flow does not vary, or over an ensemble of realizations (an imagined set of flows in which all controllable factors are kept fixed). This approach is called one-point closure and leads to a set of partial differential equations called the **Reynolds-averaged Navier-Stokes (or RANS) equations**. These equations do not form a closed set so this method requires the introduction of approximations (turbulence models). The most famous approximations or extra terms are the *k-epsilon model* and the *Reynolds stress model*. With the using of this turbulence model a high computational power is needed.
- The fourth type of method is called two-point closure. It uses equations for the correlation of the velocity components at two spatial points or, more often, the Fourier transform of these equations. These methods are rarely used except for homogeneous turbulence.
- The fifth is **Large Eddy Simulation (LES)** and solves for the largest scale motions of the flow while approximating or modelling only the small-scale motions. It can be regarded as a kind of compromise between one-point closure methods and direct numerical simulation.
- Finally, there is **Direct Numerical Simulation (DNS)** in which the Navier-Stokes equations are solved for all of the motions in a turbulent flow. Also for this method, the computational costs are considerably high.” [2] & [8]

Looking at this category list from the top to the bottom, the models consider more and more turbulent motions and fewer approximations. Which means that these methods are more exact but the computation time increases significantly.

2.4.1 Reynolds-Averaged-Navier-Stokes (RANS) Equations

RANS model (or Reynolds-Average-Navier-Stokes model) was proposed by Osborne Reynolds more than one century ago. This method is very useful to determine the proprieties of a turbulent flow such as the mean velocity, the average body forces (or its distribution), the degree of mixing between two incoming streams of fluid or the amount of a substance that has reacted. The complexity of turbulence

makes it unlikely that any single Reynolds-averaged model will be able to represent all turbulent flows, so turbulence models have to be regarded as engineering approximations rather than scientific laws.

Since the thesis project is focused on the combustion and the model validation of a real engine, this model will be the only one described and used on this thesis work.

In a statistically steady flow, every variable can be written as the sum of a time averaged value and a fluctuation about that value:

$$\phi(x_i, t) = \bar{\phi}(x_i) + \phi'(x_i, t) \quad (2.24)$$

Where

$$\bar{\phi}(x_i) = \lim_{T \rightarrow \infty} \frac{1}{T} \int_0^T \phi(x_i, t) dt \quad (2.25)$$

where t is the time and T is the averaging interval.

If the flow is unsteady, time averaging cannot be used and it must be replaced by ensemble averaging:

$$\bar{\phi}(x_i) = \lim_{N \rightarrow \infty} \frac{1}{N} \sum_{n=1}^N \phi(x_i, t) \quad (2.26)$$

where N is the number of members of the ensemble and must be large enough to eliminate the effects of the fluctuations. This type of averaging can be applied to any flow. We use the term Reynolds averaging to refer to any of these averaging processes. From Eq. 2.24, it follows that $\bar{\phi}' = 0$. Thus, averaging any linear term in the conservation equations simply gives the identical term for the averaged quantity. From a quadratic nonlinear term, we get two terms: the product of the average and a covariance:

$$\overline{u_i \phi} = \overline{(\bar{u}_i + u'_i)(\bar{\phi} + \phi')} = \bar{u}_i \bar{\phi} + \overline{u'_i \phi'} \quad (2.27)$$

The last term is zero only if the two quantities are uncorrelated; this is rarely the case in turbulent flows and, as a result, the conservation equations contain terms such as $\overline{\rho u'_i u'_j}$, called the Reynolds stresses, and $\overline{\rho u'_i \phi'}$, known as the turbulent scalar flux, among others. These cannot be represented uniquely in terms of the mean quantities. The averaged continuity and momentum equations can, for incompressible flows without body forces, be written in tensor notation and Cartesian coordinates as:

$$\frac{\partial(\rho \bar{u}_i)}{\partial x_i} = 0 \quad (2.28)$$

$$\frac{\partial(\rho \bar{u}_i)}{\partial t} + \frac{\partial}{\partial x_j} (\rho \bar{u}_i \bar{u}_j + \overline{\rho u'_i u'_j}) = \frac{\partial \bar{p}}{\partial x_i} + \frac{\partial \bar{\tau}_{ij}}{\partial x_j} \quad (2.29)$$

where the τ_{ij} are the mean viscous stress tensor components:

$$\bar{\tau}_{ij} = \mu \left(\frac{\partial \bar{u}_i}{\partial x_j} + \frac{\partial \bar{u}_j}{\partial x_i} \right) \quad (2.30)$$

Finally, the equation for the mean of a scalar quantity can be written:

$$\frac{\partial(\rho \bar{\phi})}{\partial t} + \frac{\partial}{\partial x_j} (\rho \bar{u}_j \bar{\phi} + \overline{\rho u'_j \phi'}) = \frac{\partial}{\partial x_j} \left(\Gamma \frac{\partial \bar{\phi}}{\partial x_j} \right) \quad (2.31)$$

The Reynolds-Average-Navier-Stokes equations is impossible to solve analytically because of the Reynolds stress and turbulent scalar flux. In order to make it solvable, some approximations have to be introduced. In the majority of cases the approximations include the Reynolds stress tensor and they

are called *turbulence models*. Every turbulence models add new transport equations that make the solution possible. The most important turbulence models are four:

1. *Mixing length model* is the only one who make the solution possible without adding a new transport equation.
2. *Spalart-Allmaras model* who needs an extra transport equation.
3. *k- ϵ , k- ω* who need two more transport equations. In particular the k- ϵ turbulence model has been used in this thesis project.
4. *Reynolds stress model* who needs seven extra equations.

[2]

2.5 CFD Software Used (CONVERGE)

In this thesis work the CONVERGE CFD Software has been adopted. CONVERGE is a revolutionary computational fluid dynamics (CFD) program that eliminate the manually grid generation from the simulation process. CONVERGE has been developed by expert engine simulation engineers and it has been imagined to the use for both engine and non-engine simulation. “Unlike many CFD programs, CONVERGE automatically generates a perfect orthogonal and structured grid at runtime based on simple user-defined grid control parameters. With the CONVERGE program is possible to simulate three-dimensional, incompressible or compressible, transient or steady-state, chemically reacting flows in complex geometries with stationary or moving surfaces. CONVERGE can perform calculations with any number of species and chemical reactions, as well as transient liquid sprays and laminar or turbulent flows.” [6]

“Traditionally, boundary-fitted grids transform the vertices and cells in the interior domain to conform to the shape of the geometry. There are two main disadvantages to using a traditional boundary fitted grid. First, whether structured or unstructured, fitting a grid to a complex geometry prevents the usage of simple orthogonal grids. This in turn eliminates the benefit of numerical accuracy and computational efficiency associated with the orthogonal grids. Second, generating a traditional boundary-fitted grid for a complex moving geometry can be time consuming and difficult.” [6]

“CONVERGE uses a different, better strategy: an innovative boundary-fitted approach eliminates the need for the computational grid to coincide with the geometry of interest. This method has two significant advantages. First, the type of grid used is chosen for computational efficiency instead of geometry. This allows the use of simple orthogonal grids, which simplifies the numeric of the solver. Second, the grid generation complexity and the time required are greatly reduced, as the complex geometry only needs to be mapped onto the underlying orthogonal grid. Users are required to provide only a file containing the surface geometry represented as a closed triangulated surface. This file is easily written in Stereo Lithography (STL) format in most CAD packages. Given a proper STL file for the geometry of interest, it will take few minutes to prepare a surface for even complex geometries. Note that this user time is not spent creating a grid, as CONVERGE performs the grid generation internally at runtime. Users time is spent uniquely identifying various portions of the surface so that you can specify mesh motion and boundary conditions.” [6]

“At runtime, CONVERGE uses the given triangulated surface to cut the cells that are intersected by the surface. There are many benefits of generating the grid internally by the code at runtime rather than requiring you to generate the grid as an input to the code. Runtime grid generation allows the grid to be changed during the simulation. Possible changes include scaling the cell size of the entire domain, locally refining or coarsening during the simulation, and adaptively refining the mesh. Another major advantage of runtime grid generation is the ability of CONVERGE to regenerate the grid near moving boundaries during the simulation without any input from you. This means that setting up a case with a moving boundary is no more difficult than setting up a stationary case.” [6]

“In addition to its novel approaches to grid generation and boundary treatment, CONVERGE includes state-of-the-art numerical techniques and models for physical processes including turbulence, spray, combustion, conjugate heat transfer, and cavitation. With these models, CONVERGE can simulate a wide variety of flow problems. The models in CONVERGE have been extensively validated for internal combustion engine cases.” [6]

2.5.1 Grid Control

CONVERGE has different tools to control the grid generation before and during the simulation, these main features are three and they are described above:

- Grid scaling.
- Fixed embedding.
- Adaptive mesh refinement.

Grid Scaling

Grid scaling refers to changing the base grid size at specified times during the simulation. That is very important to reduce the runtime of a simulation; the coarser the mesh is, the faster the simulation will be. At the same time, if the mesh is too coarse the resolution of the results will not be acceptable so a compromise has to be found. In order to determine the base grid size via dx_base , dy_base and dz_base , CONVERGE use the $grid_scale$ parameter according to the following relation:

$$scaled\ grid = dx_base / 2^{grid_scale} \quad (2.32)$$

Where $grid_scale$ is the scaling parameter and $scaled_grid$ is the new value of base grid size. Generally speaking, a $grid_scale$ of 0 will leave the base cells unchanged, a negative value will coarsen the base grid and a positive value will refine the base grid. CONVERGE also scales the dy_scale and the dz_scale following the same previous equation.

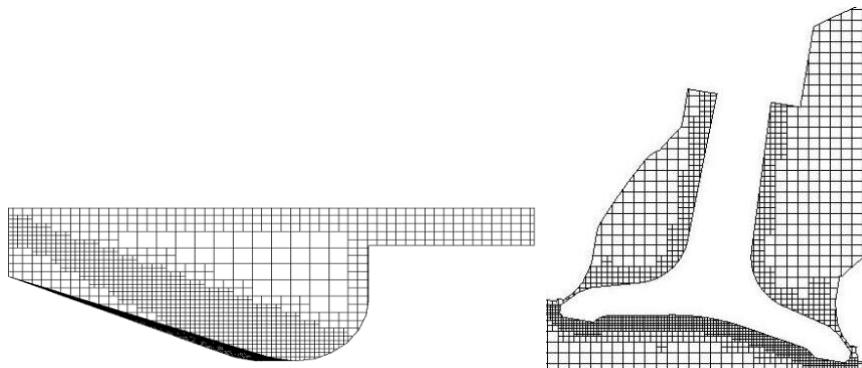
[6]

Fixed Embedding

The Fixed Embedding tool is useful to refine the mesh just in specific locations of the domain where a finer resolution is needed. For example, during a spray simulation, it is possible to add an area of fixed embedding by the nozzle to solve the complex flow behaviour. At the same time, fixed embedding allows the rest of the domain to remain with a coarse grid in order to minimize simulation time. For each fixed embedding, users need to specify an embedding scale that indicates how CONVERGE will refine the grid in that specific location. The $embed_scale$ parameter scales the base sizes (dx_base , dy_base and dz_base) according to

$$dx_embed = dx_base / 2^{embed_scale} \quad (2.33)$$

[6]



(a): A grid generated using a nozzle embedding.

(b): Typical example of Boundary Embedding which refines the grid around the boundary. For moving surfaces, the embedding will move with the surface.

Figure 2.2: Examples of Fixed Embedding

Adaptive Mesh Refinement (AMR)

“The Adaptive Mesh Refinement (AMR) automatically refine the grid basing on fluctuating and moving conditions such as temperature and/or velocity. This option permits to have a very high refined grid to accurately simulate complex phenomena such as high-velocity flow and flame propagation without slowing the simulation using a globally refined mesh. Ideally, a good AMR algorithm will add higher grid resolution where the flow field is most under-resolved or where the sub-grid field is the largest. Generally speaking, the AMR algorithm will add a grid refinement when the gradient of velocity or temperature between two cells is higher that the value specified, in this way it is possible to capture some complex phenomena behaviour that would be impossible to catch without a global grid refinement. “[6]

For a scalar, a sub-grid field is defined as the difference between the actual field and the resolved field or

$$\phi' = \phi - \bar{\phi} \quad (2.34)$$

Where ϕ is the actual scalar field, $\bar{\phi}$ is the resolved scalar field and ϕ' is the sub-grid scalar field. The sub-grid for any scalar can be expressed as infinite series given by

$$\phi' = -\alpha_{[k]} \frac{\partial^2 \bar{\phi}}{\partial x_k \partial x_k} + \frac{1}{2!} \alpha_{[k]} \alpha_{[l]} \frac{\partial^4 \phi}{\partial x_k \partial x_k \partial x_l \partial x_l} - \frac{1}{3!} \alpha_{[k]} \alpha_{[l]} \alpha_{[m]} \frac{\partial^6 \phi}{\partial x_k \partial x_k \partial x_l \partial x_l \partial x_m \partial x_m} \dots \quad (2.35)$$

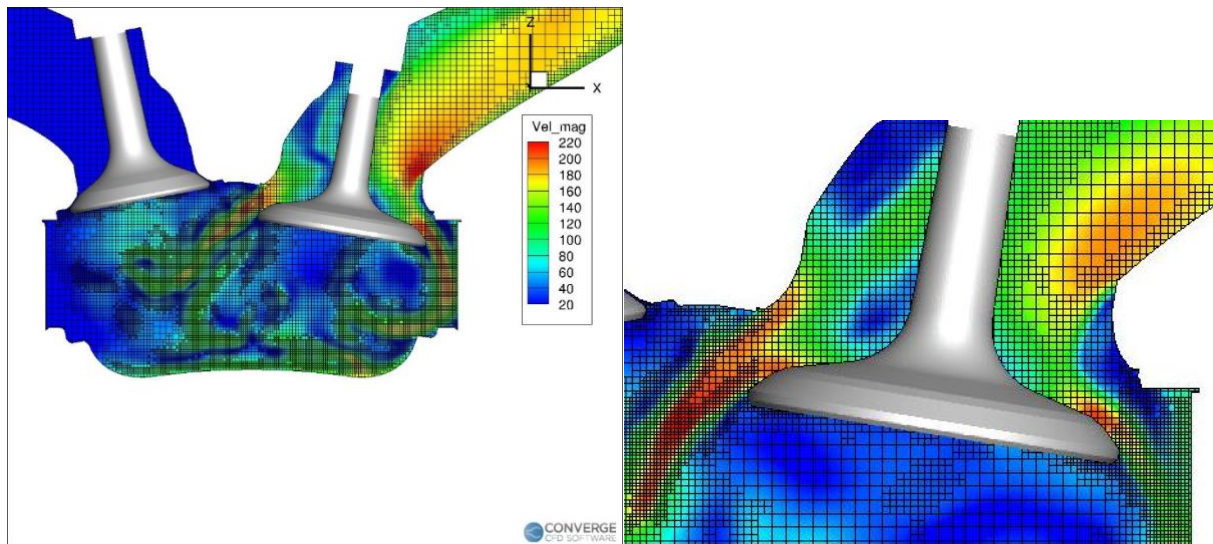
where α is $dx_{[k]}^2/24$ for a rectangular cell and the brackets, $[]$, indicate no summation. Since it is not possible to evaluate the entire series, only the first term (the second-order term) in the series is used to approximate the scale of the sub-grid. A cell is embedded if the absolute value of the sub-grid field is above a user-specified value. Conversely, a cell is released (i.e., the embedding is removed) if the absolute value of the sub-grid is below 1/5th of the user-specified value. With CONVERGE is also possible to limit the number of embedded cells specifying a maximum number of cells. If the number of cells reaches the maximum value, CONVERGE uses the AMR routine to decide where to put the embedding in a manner that best resolves the flow field and meets the maximum number of cells. To make optimal use of all of the cells when the cell limit is reached, CONVERGE will adjust the user-specified sub-grid value criteria as needed. [6]

The same it is allowed with a minimum number of cells, if the number of cells counted is less than the specified value, CONVERGE will automatically add embedding. With the maximum and the minimum value of cells, a range can be maintained in order to optimize the simulation run-time.

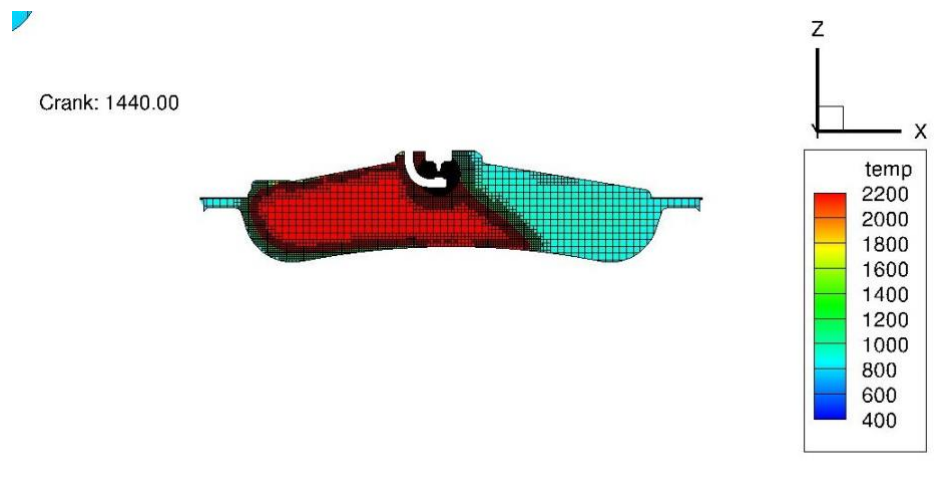
CONVERGE also allows to enable AMR for any or as many fields such as velocity, number of parcels per cell, temperature, void fraction, species, passives, or boundary (y^+); in all of them a different embedding scale and different sub-grid criterion is possible to set for each condition. In addition to the field control, users can specify the time when the AMR will start and when it will end for each field.

Sometimes, in some simulations could happened that the sub-grid quantities near the solid walls trigger the AMR. Since the flow near the wall is slow, it is not physically interest. CONVERGE avoid the refinement near the walls with the y^+ restriction with a target value that can be set and CONVERGE automatically will remove refinement from AMR to maintain the desired target value.

[6]



(a): AMR through the valves.



(b): AMR during the combustion.

Figure 2.3: Adaptive Mesh Refinements (AMR) examples.

3. Experimental Data Analysis

3.1 Introduction

This project thesis aim, as previously introduced, is the validation of a CFD model 1.4 litre internal combustion engine (ICE) supplied with natural gas (NG) and NG plus percentages of hydrogen, using CONVERGE. The experimental data have been provided by *Politecnico di Torino* University. This project is focused on the combustion simulation using SAGE detailed chemistry model.

In this chapter the engine considered will be described focusing on the treatment of the experimental data in order to define all the variables needed to compare the model with the measurements and, consequently, obtain the model validation.

3.2 Engine Characteristics

The engine considered is a Fiat FIRE 1.4 litre 16V turbo CNG, assembled by “Centro Ricerche FIAT” (CRF) and installed in the Energy Department Laboratory of Politecnico di Torino. The engine is optimised for the natural gas combustion and, with this project thesis, the NG+H₂ combustion will be also modelled.



Figure 3.1: Engine on the test bench.

The following table (Table 3.1) shows the main engine characteristics.

Cycle	4 strokes (OTTO)
Valves	16V with two cam-shaft
Intake valve opening (IVO)	3° before TDC
Intake valve closing (IVC)	37° after BTC
Exhaust valve opening (EVO)	37° after BTC
Exhaust valve closing (EVC)	3° before TDC
Cylinders	4 in line
Bore	72 mm
Stroke	84 mm
Displacement	1368 cm ³
Compression Ratio	9.8

Table 3.1: Engine main Characteristics

3.2.1 Fuel Supply

ICEs are the most important technology used for the transportation, unfortunately they produce air pollution, due to the fossil fuels burning. Nowadays, these emissions are controlled and they have to remain above to a certain limit in order to be defined inside a safety range.

In this project two different fuel compositions will be analysed. The first validation will carry out with the Natural Gas fuel composition (NG) where the species considered are the followings:

- CH₄ = 98%
- C₂H₆ = 1%
- CO₂ = 1%

Considering this fuel composition is an approximation because the real NG composition is composed by hundred species. Since these species have a very low percentage value, they can be negligible in order to decrease the simulation runtime avoiding the calculation of useless species chemical reactions.

After the authentication of NG model, the second validation will be to add 15 % of hydrogen in the previous fuel composition obtaining the following composition:

- CH₄ = 83.3%
- C₂H₆ = 0.85%
- CO₂ = 0.85%
- H₂ = 15%

These two fuel compositions have a low carbon level, which means that their burned residuals will be with less carbon pollution such as carbon-monoxide, carbon-dioxide and unburned hydrocarbons. That is really important since the health of the world environment is decreasing because of burned emissions as the ones cited before. This problem became an everyday issue so the study of new and alternative fuels able to decrease or, ideally, to completely eliminate pollution is fundamental.

3.3 Experimental Data Treatment

The experimental data have been provided by the Politecnico di Torino and the measurements have been taken directly on the Energy Laboratory of the university, where the engine is installed. The measurements are subdivided per engine operating point and they have been provided as a TDMS (Technical Data Management Streaming) file extension.

This file extension is not readable directly by Excel so their conversion has been carried out with Add-In Excel Tool.

Once the conversion is done, it is possible to read the files and start with the treatment of the data themselves. First of all, it is important to underline that the engine is designed with 4 cylinders but the CFD analysis will take place just on the first one because the boundary conditions are referred just on that one.

The most important data to extract from the measurement sheets are: the pressure in the cylinder which can be found as P_Cyl1 in the sheet *TAF*, the ensemble average pressure that can be found as P_Cyl_ens in the sheet *P_Cyl1_ens*, the air mass flow rate (\dot{m}_a) which can be found as M_A in the sheet *LFstatistic*, the fuel mass flow rate (\dot{m}_f) that can be found as M_F in the sheet *LFstatistic* and the air fuel ratio (α) which can be found as a in the sheet *LFstatistic*.

Below a brief description of the main parameters and problems useful to define which are the main variables with which the validation has been carried out.

3.3.1 Trapped Mass Problem

The Trapped Mass is defined as the mass that stand in the combustion chamber when the system is closed by means the closure of the engine valves. Generally speaking, after the aspiration phase, when the air and the fuel pass throw the valves and finally arrive in the cylinder with a moderate value of turbulence, the intake valve close itself and the air/fuel mass remained in the chamber is precisely called trapped mass.

The trapped mass can be calculated in different ways and, in this chapter, two methods will be described.

First of all, the fuel mass has to be calculated with the follow relation who determine it by using the experimental fuel mass flow rate \dot{m}_f , available on the experimental data sheets:

$$m_{f,exp} = \frac{\dot{m}_f [kg/h] / 3600}{n[rpm] / 60} \cdot \frac{1}{2} \quad (3.1)$$

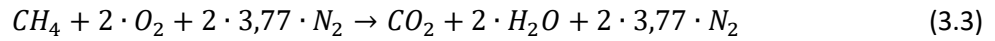
Where n is the engine velocity.

The trapped mass, now, is possible to be calculated. The first method showed does not take in account the combustion residues and it is easy to determine with the equation 3.2:

$$m_{cyl,exp} = (1 + \alpha) \cdot m_{f,exp} \quad (3.2)$$

Where α if the air/fuel ratio available on the experimental data sheets.

Conversely, the second method takes in account the combustion residues, in particular the CO₂ mass fraction. The hypothesis made during this calculation is that the CO₂ mass fraction, present in the chamber, can be considered equal to the model one. In this way, it is possible to take the CO₂ mass fraction value directly from the CONVERGE output files, precisely from the *species_mass_region1.out* file. The CO₂ value has to be taken inside of the range between the intake valve closing (IVC) crank angle, exhaust valve opening (EVO) crank angle and before the spark advance (SA) crank angle in order to find the system closed and not during the combustion phase. The mass fraction of CO₂ in the exhausts (x_{CO_2}) can be computed by considering the following combustion balance equation:



Where the 3,77 value is the average molar ratio of nitrogen over oxygen. So, it is possible to write:

$$M_{CH_4} = (M_{CO_2} + 2 \cdot M_{H_2O} + 2 \cdot 3,77 \cdot M_{N_2}) \quad (3.4)$$

The fuel mass can be written as:

$$m_{f,model}(1 + \alpha) = \frac{m_{f,model}}{M_{CH_4}} (M_{CO_2} + 2 \cdot M_{H_2O} + 2 \cdot 3,77 \cdot M_{N_2}) = m_{exh,model} \quad (3.5)$$

And

$$\frac{m_{CO_2}}{m_{exh}} = x_{CO_2} = \frac{M_{CO_2}}{M_{CH_4}(1+\alpha)} = \frac{44.01 \left[\frac{kg}{mol} \right]}{16.01 \left[\frac{kg}{mol} \right] \cdot (1+\alpha)} \quad (3.6)$$

The mass fraction can be therefore obtained by:

$$x_{r,model} = \frac{M_{CO_2}}{x_{CO_2} \cdot m_{cyl,exp}} \quad (3.7)$$

Where $m_{cyl,exp}$ has been calculated with the equation 3.2.

Finally, the trapped mass can be computed with a correction on the equation 3.2 as the following relation shows:

$$m_{cyl,exp} = (1 + \alpha) \cdot (1 - x_{r,model}) \cdot m_{f,exp} \quad (3.8)$$

For this thesis work the second method has been considered.

Afterwards, the model trapped mass calculated by CONVERGE has to be compared with the experimental one just computed. The model trapped mass value can be taken on the *thermo_region1.out* file and it has to be taken, as previously described, between the IVC crank angle, EVO crank angle and before SA crank angle.

[8]

3.3.2 Heat Release Rate (HRR)

Heat Release Rate (HRR) is the rate of the instantaneous heat generation by fire. It is typically measured in Joules per second or Watts. During the combustion this variable is really significant because it shows how the combustion is going and the quantity of energy that is producing. Since it is calculated considering the crank angles referred to the combustion phase, this shows also when the combustion begins and for how many crank angles it lasts. This is fundamental to comprehend if the air/fuel mix is

burning correctly or not and it can also be compared with the experimental data, making easier the model validation.

In order to compute the HRR, the range between the IVC crank angle and the EVO crank angle has to be considered in order to be able to define this period of the chamber a closed system.

As it is known, during a combustion or a simple fuel burn, some losses throw the walls are always present, for this reason a distinction between the *Gross-HRR* and the *Net-HRR* is essential. They can be expressed respectively:

$$HRR_{gross} = \frac{dQ_b}{d\theta} = \frac{k}{k-1} p \frac{dV}{d\theta} + \frac{k}{k+1} V \frac{dp}{d\theta} + \frac{dQ_t}{d\theta} \quad (3.9)$$

$$HRR_{net} = \frac{dQ_b}{d\theta} - \frac{dQ_t}{d\theta} = \frac{k}{k-1} p \frac{dV}{d\theta} + \frac{k}{k+1} V \frac{dp}{d\theta} \quad (3.10)$$

Where k is the heat capacity ratio, $\frac{dQ_b}{d\theta}$ is the heat provided by the fuel burning and $\frac{dQ_t}{d\theta}$ are the heat losses.

Noteworthy is the fact that, the HRR is calculated from the pressure, which means that a variation of the pressure value produces a variation of the heat generated. This variable is really sensitive, so a slightly pressure variation produces a high HRR variation which makes that variable really important on a combustion study.

Since the calculation or the prediction of the heat losses is difficult or impossible to define, the Net-HRR will be considered in this thesis project.

The evaluation of the heat capacity factor is made by the Michael F.J. Brunt methodology [13] which cites:

$$k = 1.338 - 6 \cdot 10^{-5} \cdot T + 6 \cdot 10^{-8} \cdot T^2 \quad (3.11)$$

3.3.3 Integrated Heat Release (IHR)

Another fundamental parameter, useful to monitor the combustion phase, is the Integrated Heat Release (IHR) who is measured in Joule and it is defined as the HRR integral. This variable shows which is the total energy in the chamber, useful if compared with the measurements. The IHR can be obtained integrating the HRR (equation 3.10) between the EVO crank angle and the SA crank angle:

$$IHR = \int_{\theta_{SA}}^{\theta_{EVO}} \left(\frac{dQ_b}{d\theta} - \frac{dQ_t}{d\theta} \right) d\theta \quad (3.12)$$

Thanks to this parameter, compute the crank angle where the 10%, 50 % and 90% of the fuel mass in the chamber is burned, is useful to understand and visualise the combustion duration in terms of crank angles.

In order to compute the crank angle related to the 10, 50 and 90 percent of burned mass, an Octave script has been coded, in which every single point of the integrated heat release has been divided to the maximum value of this parameter. In this way we can obtain a percentage of the energy normalised to the maximum value that corresponds to the burned mass fraction. The final results are called CA10, CA50 and CA90 that correspond to crank angles where the burned mass is 10%, 50% and 90% respectively.

Additionally, the burn duration can be easily calculated with a subtraction between CA90 and CA10 and the result is in terms of crank angles. The burn duration is determined just between 10% and 90% of burned mass because the 5%, 1% or 95%, 99% are really difficult to compute, so the combustion duration is taken just from these two values.

$$\text{Burn Duration [CAD]} = CA90 - CA10 \quad (3.13)$$

3.3.4 Statistic Methods

Engines, especially Natural Gas engines, are characterized by a phenomenon called cycle to cycle variability (CCV). This phenomenon is a remarkable fluctuation of the combustion intensity which is reflected on the pressure profile decreasing or increasing the pressure peak cycle per cycle. The CCV is depended by the turbulence and by a myriad of other parameters such as environment temperature, pressure, humidity etc., so a representative cycle, to compare to the simulations, is required. For this reason, statistical examinations are obligatory and the most common one is the *Ensemble Average* method. The *Ensemble Average* is a mean of all the Experimental cycles that has been measured, however that does not represent a real cycle. For this purpose, and since the number of cycles simulated in this project thesis are not high, the ensemble average cannot be used and the model validation is referred to a real cycle which represent the closest experimental cycle to the *ensemble average*.

The calculation of the closest cycle to the *ensemble average* has been carried out by an Octave Script, in which every single point of the ensemble average is compared to all the experimental cycle and just the cycle with more similar values has been considered. After this analysis the obtained cycle is the “*reference cycle*” with who it has been possible compare the simulations results.

With the same script, also the *maximum cycle* and the *minimum cycle* has been calculated. They represent the validity range, made by the CCV, with who is possible to determine if the simulation results can be considered acceptable or not.

In order to add a new parameter to the analysis, in the same script, a calculation of all the pressure peaks has been appended. The result of this computation is a cloud of points that characterize all the experimental pressure maximum values. In this way, find a trend line or determine if the simulation pressure peaks location is right should be easier and also visible by a simple plot.

From now all the parameters needed has been described thus, now the engine operating points considered will be define with plots visualisation.

[8]

3.4 Operating Points Considered

In this thesis work three cases have been analysed:

Engine speed [rpm]	Engine load (BMEP) [bar]	Fuel [-]	Lambda [-]
4600	7.9	CH ₄	1
4600	7.9	CH ₄ +H ₂	1
2000	14	CH ₄	1

Table 3.2: Operating points considered

3.4.1 Operating point 4600x7.9x1 CH₄

This operating point is characterized by the followings features:

- *Spark advance*: 25 CAD before Top Dead Centre (TDC).
- *Air/fuel ratio α* : 17.32.
- *Fuel mass flow rate \dot{m}_f* : 9.8545 kg/h.
- *Air mass flow rate \dot{m}_a* : 170.66 kg/h.
- *Number of experimental cycles*: 100.

This operating point has a high velocity but an average load.

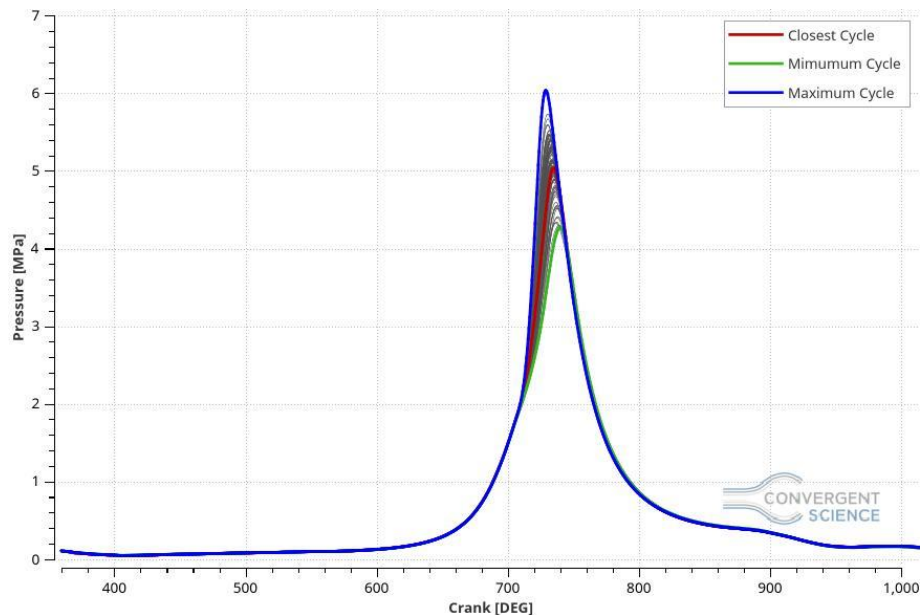


Figure 3.2: 4600x7.9 CH₄ Experimental Pressure plot.

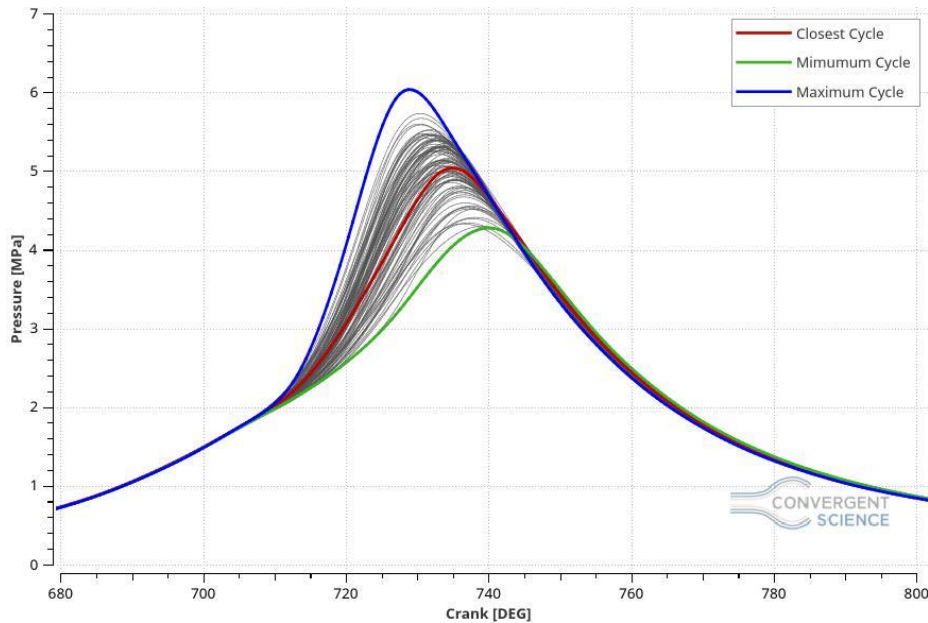


Figure 3.3: Experimental data zoom on the pressure peaks.

In the Figure 3.1 we can see that this operating point is characterized by a relevant cycle to cycle variability. In this picture has been marked the reference cycle, or the closest cycle to the ensemble average, the maximum and the minimum cycle and all the others 100 cycles presents in the experimental data.

It is also easy to visualize the validity range, mentioned above, made by the three highlighted cycles, where the simulation pressure curve has to be inside to be defined acceptable.

Finally, the scatter plot has been determined to be able to define which is the validity range of the pressure peak locations. Also the linear regression of the 100 experimental cycles pressure peaks has been determined, which represents a straight line, called trend line, that shows the line in which the simulation peak locations have to be able to define the model valid. The statistic validity range is defined by an R^2 equal to 0.8643 which means that the cloud of points has a linear relation and it is not random.

These considerations will be the same for all the other operating points.

3.4.2 Operating point 4600x7.9x1 CH₄+H₂

This operating point has many characteristics:

- *Spark advance*: 23 CAD before Top Dead Centre (TDC).
- *Air/fuel ratio α* : 17.81.
- *Fuel mass flow rate \dot{m}_f* : 9.48 kg/h.
- *Air mass flow rate \dot{m}_a* : 168.64 kg/h.
- *Number of experimental cycles*: 100.

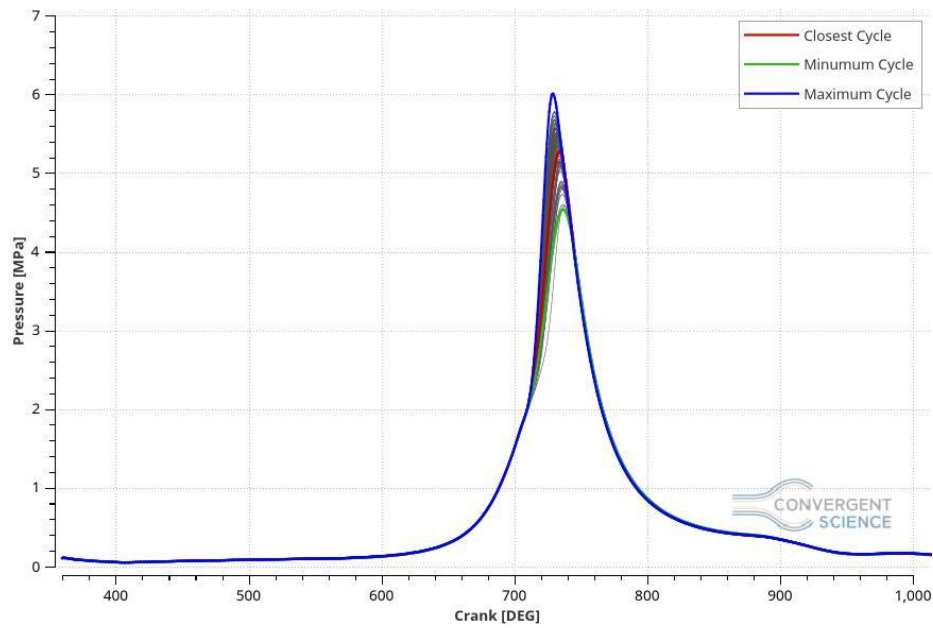


Figure 3.4: 4600x7.9 CH₄+H₂, Experimental Pressure plot.

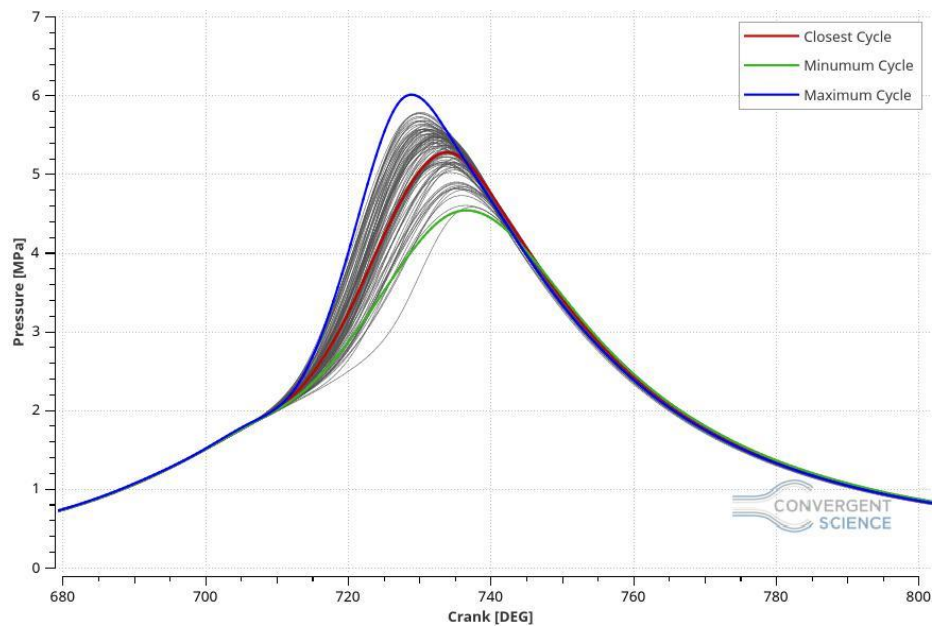


Figure 3.5: Experimental data zoom on the pressure peaks.

3.4.3 Operating point 2000x14x1 CH₄

This operating point has the following characteristics:

- Spark advance: 20 CAD before Top Dead Centre (TDC).
- Air/fuel ratio α : 17.27.
- Fuel mass flow rate \dot{m}_f : 6.48 kg/h.
- Air mass flow rate \dot{m}_a : 111.89 kg/h.
- Number of experimental cycles: 100.

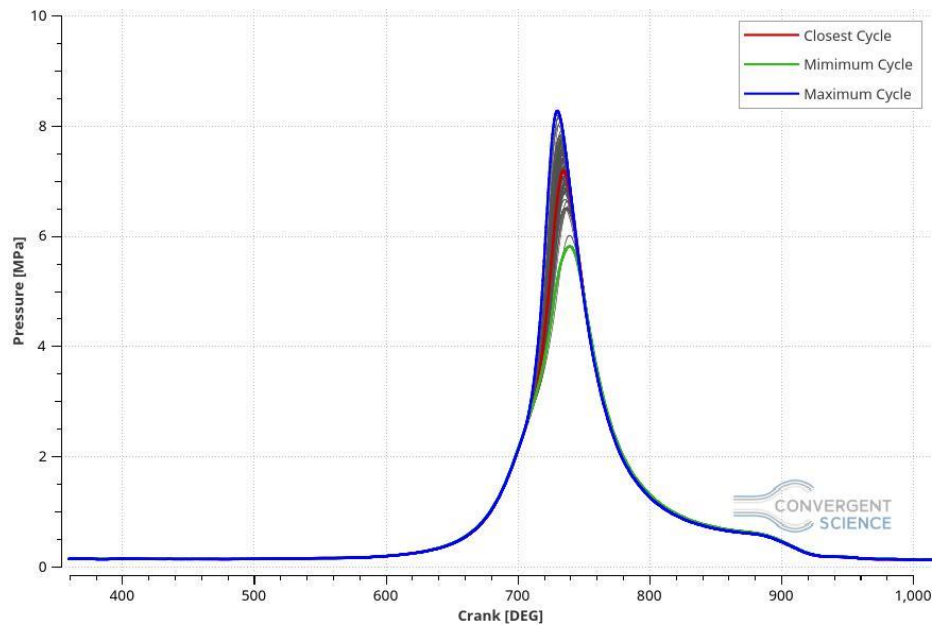


Figure 3.6: 2000x14 CH₄, Experimental Pressure plot.

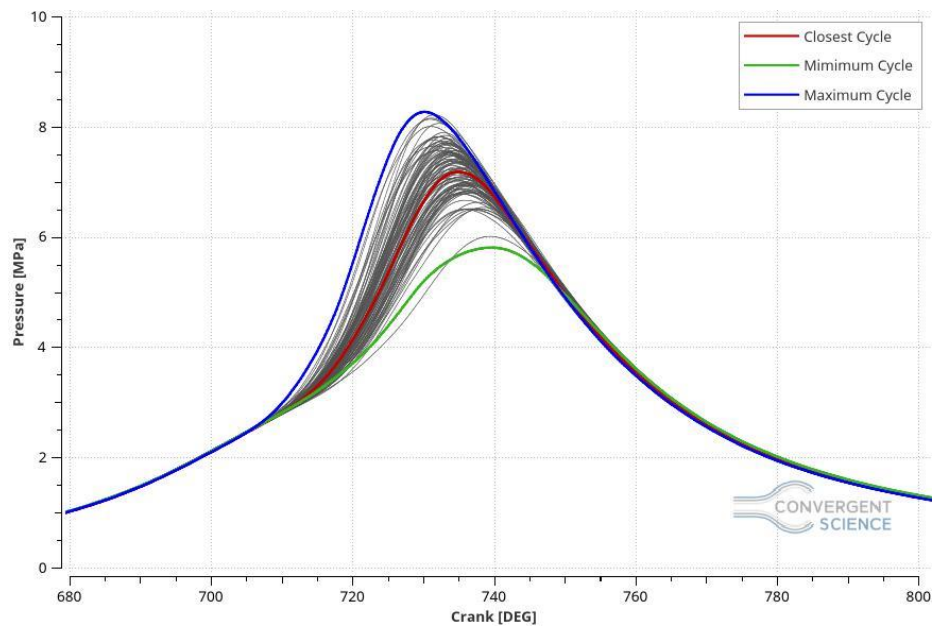


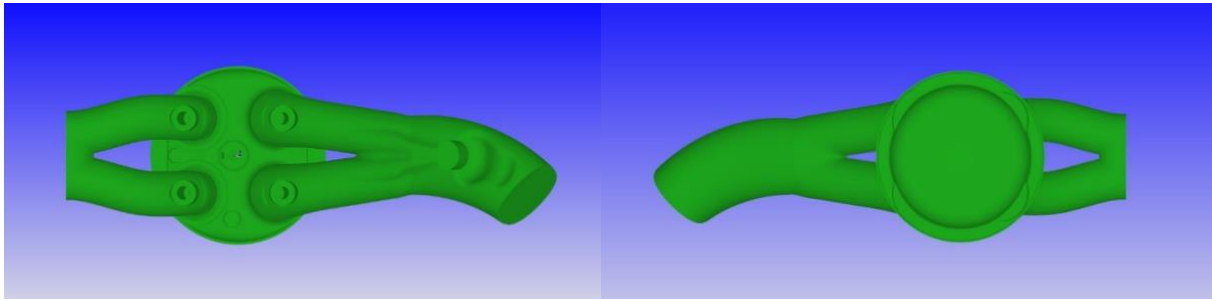
Figure 3.7: Experimental data zoom on the pressure peaks.

4. The Model

In this chapter all the case setup characteristics will be explained focusing on the features used on this particular thesis work. The following case set up features refer to the final one and, if necessary, some modifications will be described in the next chapter.

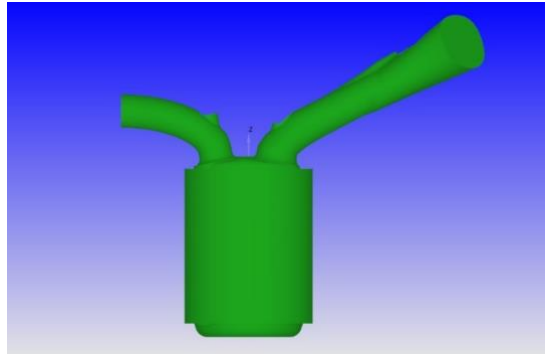
4.1 Regions and Geometry

The geometry of the engine analysed has been provided by CRF (Centro Ricerche Fiat) as a CAD file and as a STL file (Standard Triangulation Language). The STL file describes only the surface geometry of the three-dimensional object with triangles, defining, in a three-dimensional Cartesian coordinate, the vertices of the triangles.

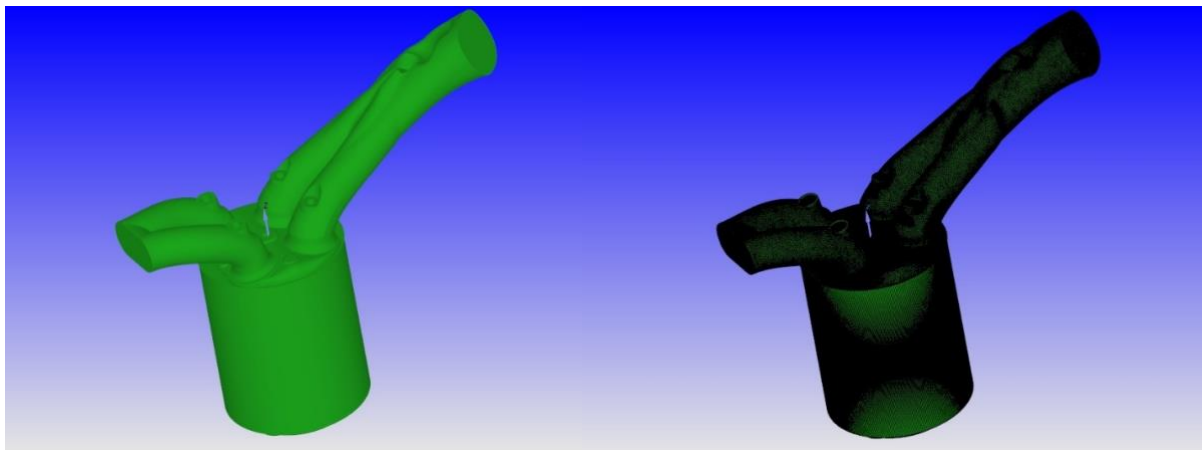


(a): Engine Geometry top view.

(b): Engine Geometry bottom view.



(c): Engine Geometry side view.



(d): CAD Engine Geometry isometric view.

(e): STL Engine Geometry isometric view.

Figure 4.1: Engine Geometry.

The geometry shown in the figure 4.2 can be subdivided in three different regions:

- **Intake System:** it is the volume of geometry who includes the intake run, the intake valves top, the intake valves angle and the inflow of the engine. In CONVERGE it has been defined as *region0*.
- **Cylinder:** it is the volume of geometry who contains the liner, the head, the piston, the spark plug, the spark plug electrode and valves bottom of the engine. In CONVERGE it has been named as *region1*.
- **Exhaust System:** it is the volume of geometry who contains the exhaust port, the exhaust valves top, the exhaust valves angle and the outflow of the engine. It has been called *region2*.

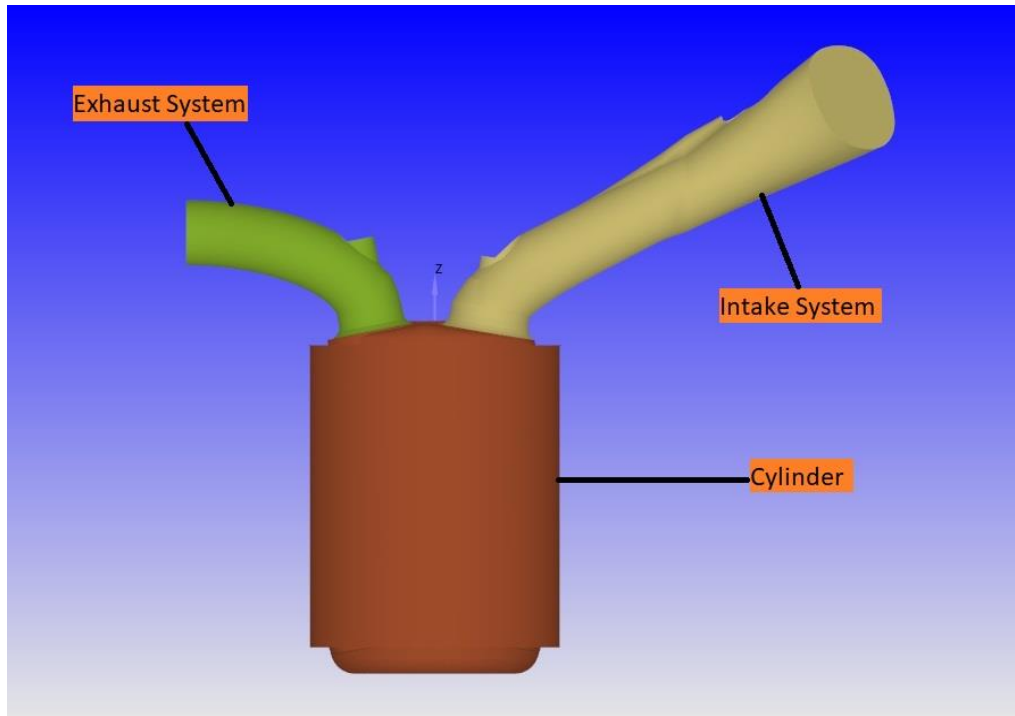


Figure 4.2: Engine Regions.

Finally, every single component of the engine has to be assigned to a different boundary in order to permit different settings for each of them. When the boundaries are created, they have to be given to the regions where they are located. The table 4.1 shows all the boundaries created and in which region they are assigned.

Boundary Name	Region
Head	Cylinder
Liner	Cylinder
Piston	Cylinder
Spark Plug	Cylinder
Spark Plug Electrode	Cylinder
Inflow	Intake System
Outflow	Exhaust System
Exhaust Port Top	Exhaust System
Exhaust Valve Bottom	Cylinder
Exhaust Valve Angle	Exhaust System
Exhaust Valve Top	Exhaust System
Intake Port Top	Intake System
Intake Port Bottom	Intake System
Intake Valve Bottom	Cylinder
Intake Valve Angle	Intake System
Intake Valve Top	Intake System

Table 4.1: Boundary Names and Assignment.

4.2 Boundary Conditions

In Computational Fluid Dynamics (CFD) problems, the *Boundary Conditions* are a set of input parameters or conditions which define the initial values to set and solve the differential equations cited above (chapter 2.2 *Basic Concepts of Fluid Flow*).

In this particular case the boundary conditions have been computed by a Matlab script which has been provided by Politecnico di Torino University. This script is based on the experimental data, measured with particular sensors directly in the Energy department of the University itself and, through them, the Inflow and the outflow boundary condition has been calculated.

For the inflow temperature, a constant value has been used considering it as an average temperature value of all the examination carried out on the test bench. Unfortunately, this is an approximation. In the reality the temperature is a fluctuant value that should be measured and used during a CFD model validation to make the model more realistic.

All the temperatures of the other boundaries have been measured with sensors on the test bench and their value has been set in the CFD model.

Name	Boundary type	Temperature [K]
Head	Wall	448.81
Liner	Wall	448.81
Piston	Wall	448.81
Spark Plug	Wall	550
Spark Plug Electrode	Wall	600
Inflow	Inflow	353
Outflow	Outflow	828
Exhaust Port	Wall	498.81
Exhaust Valve Bottom	Wall	498.81
Exhaust Valve Angle	Wall	498.81
Exhaust Valve Top	Wall	498.81
Intake Port Top	Wall	340
Intake Port Bottom	Wall	340
Intake Valve Bottom	Wall	340
Intake Valve Angle	Wall	340
Intake Valve Top	Wall	340

Table 4.2: Temperature Boundary Conditions.

4.3 Regions Initialisations

A fundamental part of the case setup is the initialisation of the regions which defines the engine geometry. This setting is useful to establish all the thermodynamic and chemical characteristics of each region. In addition to the pressure and temperature, also the species mass fraction present at the simulations start time have to be set.

Since the simulation start time is fixed at 130 CAD, exactly before the exhaust valve opening (EVO), the region initialisation values have to be referred at that crank angle. Precisely, the intake and exhaust system pressure value have to be equal to the boundary condition pressure one at that CAD, while the cylinder pressure has to be equal to the experimental data pressure value at that CAD. For the same reason, the species composition in the regions has to be: in the intake system the fuel composition previously described (chapter 3.1.1 *Fuel Supply*) and in the exhaust system and cylinder the burned species composition.

4.5 Combustion Modelling

“The Combustion is a high-temperature exothermic redox chemical reaction between a fuel, also called reductant, and an oxidant, usually air (atmospheric oxygen). This reaction produces a large amount of energy which can be used to make work and move objects like cars and all the machines where a thermal engine is installed. It produces residues and gaseous products, generally called smoke.” [11]

There are many types of combustion processes, such as gaseous fuel combustion, liquid fuel combustion, spray combustion, solid fuel combustion and pulverised fuel combustion. [8]

In the engineer applications the combustion is one of the main phenomena used, for this purpose it is essential to comprehend this phase in all of its details in order to be able to predict its behaviour under different conditions such as temperature, pressure and turbulence differences. CFD models can simulate this phase very well thanks to many different combustion models that are implemented in the code and with whom predict the combustion behaviour can be possible.

Referring to the type of fuel used, the combustion of internal combustion engines can be subdivided in two categories:

- *Spark ignition engine (S.I.):* they use fuels with relatively high ignition delays for example low reactivity, such as petrol, methanol, ethanol, natural gas and LPG. The fuel, premixed with the combustion air generally outside the cylinder, can be compressed (with $\varepsilon \cong 10$) without this giving rise to combustion reactions. The combustion process must be started by means of an electric spark, capable of bringing a small portion of the mixture to $T=10^3$ K: from this first ignition core the combustion propagates gradually to the rest of the charge under a turbulent regime condition.
- *Compression ignition engine (C.I. or Diesel engine):* they use fuels with relatively short ignition delays for example high reactivity, such as diesel fuel and biodiesel. The fuel cannot be pre-mixed with compressed air without this giving rise to combustion reactions. In order to control the combustion process, the fuel is therefore introduced at the end of the compression in the cylinder, where in contact with the high temperature combustion air, it spontaneously ignites without the necessity of an external priming.

With the energy produced by the combustion, with a consequently rapid increasing of the pressure in the chamber, the piston is pushed down generating work on the engine shaft.

In this thesis work the engine is a NG one so the first type of combustion will be modelled.

In the spark ignition engines, the combustion can be subdivided in three phases:

- First phase, where the first portion of fuel burns by the spark electrical energy, produce, as a consequence, an increasing of pressure in the cylinder.
- The turbulent combustion phase is a turbulent combustion behaviour with a very high velocity which can be considered as instantaneous, since the piston, and consequently the volume of the chamber, does not change.
- The combustion completion phase where the flame front reaches the walls and all the others zones of the chamber.

4.5.1 Chemical kinetics

During an engine study, the deep comprehension of how the combustion works is needed to be able to predict its behaviour in every conditions.

Even considering the simplest fuel (CH₄), the oxidation process of the molecule is extremely complex. It is a process that passes through a large number of intermediate reactions with possible different pathways that can be followed by the molecule up to the full oxidation.

The rate at which chemical reactions proceed depends on the concentration of reacts and temperature. This field is called *Chemical Kinetics* and, in this chapter, it will be described.

Most of the chemical reactions of interest in combustion are binary reactions, where two reactant molecules, M_a and M_b, with the capability of reacting together, collide and generate two product molecules, M_c and M_d.



An example of such a reaction is the oxidation of the hydrogen by which water steam is generated.



The law of mass action asserts that “the rate at which product species are produced and the rate at which reactant species are removed is proportional to the product of the concentrations of a reactant species, with the concentration of each species raised to the power of its stoichiometric coefficient ν_i ” [12]. Consequently, for the reaction (4.1), R^+ is the forward direction reaction rate and it holds:

$$R^+ = -\frac{d[M_a]^+}{dt} = \frac{d[M_c]^+}{dt} = k^+[M_a][M_b] \quad (4.3)$$

And the R^- is the backward direction reaction rate:

$$R^- = -\frac{d[M_c]^-}{dt} = \frac{d[M_a]^-}{dt} = k^-[M_c][M_d] \quad (4.4)$$

Where k^+ and k^- are the rate constants in the forward and reverse directions.

The net rate of production of products and deletion of reactant is written:

$$R^+ - R^- = k^+[M_a][M_b] - k^-[M_c][M_d] \quad (4.5)$$

All of these results can be written in a generally form as follow.

$$\sum_{i=1}^n \nu_{R_i} M_{R_i} = \sum_{i=1}^m \nu_{P_i} M_{P_i} \quad (4.6)$$

Where ν_i is the stoichiometric coefficient of the species M, R and P are the reactant and the products respectively, n is the number of reactant species and m is the number of product species. With this nomenclature the forward and backward reaction rate will be:

$$R^+ = k^+ \prod_{i=1}^n [M_{R_i}]^{\nu_{R_i}} \quad (4.7a)$$

$$R^- = k^- \prod_{i=1}^m [M_{P_i}]^{\nu_{P_i}} \quad (4.7b)$$

Deriving all in the time difference the removal net rate of reactant species and the net rate of production of product species are:

$$-\frac{d[M_{R_i}]}{dt} = \nu_{R_i}(R^+ - R^-) \quad (4.8a)$$

$$-\frac{d[M_{P_i}]}{dt} = \nu_{P_i}(R^+ - R^-) \quad (4.8b)$$

The rate constant k follows the Arrhenius form:

$$k = A \exp\left(-\frac{E_A}{RT}\right) \quad (4.9)$$

Where A is the preexponential factor which is a function of temperature that, usually, it is determined experimentally and E_A is the activation energy. The term $-\frac{E_A}{RT}$ is called Boltzmann factor which defines the amount of collision that have an energy greater than the activation energy.

[12]

4.6 CONVERGE Combustion Models

“In CONVERGE many combustion models are implemented, including models for general combustion, premixed combustion, non-premixed combustion, turbulent combustion and diesel combustion. In CONVERGE also several emissions models are present.” [6]

The most predictive and accurate combustion model is *SAGE detailed chemistry solver* which is the model used for this thesis project and, below, a description will take place.

Many others combustion models are implemented in CONVERGE and they are called *simplified combustion models* which are less predictive and accurate than SAGE but they require an inferior computational computer power and, usually, they provide acceptable results as well.

The most important simplified combustion models can be subdivided in *Premixed turbulent combustion models* and *Non-premixed turbulent combustion models*. The main former models are:

- Chemical Equilibrium (CEQ);
- G-Equation;
- Extended Coherent Flame Model (ECFM);
- Flamelet Generated Manifold (FGM).

On the other hand, the main *Non-premixed turbulent combustion models* are:

- Characteristic Time Combustion (CTC);
- Shell ignition;
- Chemical Equilibrium (CEQ);
- Representative Interactive Flamelet (RIF);
- Extended Coherent Flame Model with 3 zones model (ECFM3Z).

4.6.1 SAGE Details Chemistry Kinetic Solver

In this thesis project will be describes just the *SAGE Details Chemistry Kinetic Solver* since it is the only combustion model used.

SAGE needs a chemical reaction mechanism, which is a set of elementary reactions that describe as overall chemical reaction, in order to know all the species and the reaction to solve. SAGE calculates the reactions rate for each elementary reaction while the CFD solver solves the transport equations. In this way, the combustion of different fuels can be modelled changing the reactions mechanism.

In SAGE the forward constant rate k is expressed by the Arrhenius form:

$$k^+ = A T^b \exp\left(\frac{E_a}{RT}\right) \quad (4.10)$$

Where, as previously mentioned, A is the pre-exponential factor, b is the temperature exponent, E_a is the activation energy and R is the universal gas constant. The reverse constant rate can be also calculated from the equilibrium coefficient k_{cr} :

$$k^- = \frac{k^+}{k_{cr}} \quad (4.11)$$

The k_{cr} coefficient can be determined by thermodynamics proprieties and it holds:

$$k_{cr} = k_{pr} \left(\frac{P_{atm}}{RT} \right)^{\sum_{m=1}^M \nu_{mr}} \quad (4.12)$$

Where P_{atm} is the atmospheric pressure, R is the gas constant and T is the temperature.

k_{pr} is obtained by:

$$k_{pr} = \exp \left(\frac{\Delta S_r^0}{R} - \frac{\Delta H_r^0}{RT} \right) \quad (4.13)$$

Where S is the entropy, H is the enthalpy and Δ refers to the change that occur to pass from the reactants to the products, especially:

$$\frac{\Delta S_r^0}{R} = \sum_{m=1}^M \nu_{mr} \frac{S_m^0}{R} \quad (4.14)$$

and

$$\frac{\Delta H_r^0}{RT} = \sum_{m=1}^M \nu_{mr} \frac{H_m^0}{RT} \quad (4.15)$$

Finally, with the following information, the mass and the energy conservation governing equations can be solved.

$$\frac{d[X_m]}{dt} = \dot{\omega}_m \quad (4.16)$$

$$\frac{dT}{dt} = \frac{V \frac{dP}{dt} \sum_m (\bar{h}_m \dot{\omega}_m)}{\sum_m ([X_m] \bar{c}_{p,m})} \quad (4.17)$$

Where V is the volume, P is the pressure, \bar{h}_m is the molar specific enthalpy and $\bar{c}_{p,m}$ is the molar constant-pressure specific heat. The above equations are resolved in each computational time step and the species are updated appropriately. It is important to note that the temperature obtained from equation 4.17 is used to update only the velocity coefficients because SAGE solves the system of velocity equations and is not used to update the cell temperature. The cell temperature is updated after the detailed chemistry calculation has been converted using the calculated species concentrations.

[6]

4.7 Chemical Reaction Mechanisms

The *Chemical Reaction Mechanism*, as previously described is a set of elementary reactions that describe as an overall chemical reaction, which means that inside of that file only the most relevant reaction will take place in order to have the same account of energy and emissions of the complete reaction.

Since this thesis work is a continuation of a previous project, the reaction mechanism used will not be validate and the authentication can be found on “Combustion modelling of a NG engine using detailed chemistry in CONVERGE” by Lorenzo Testa.

The reaction mechanisms used are:

- GRI-Mech 3.0;
- USC-Mech II.

Inside of a reaction mechanism file is present a significant variety of chemical reactions with all the species referred to and, for each species, all the thermodynamic parameters and the rate of coefficient expressions.

4.7.1 GRI-Mech 3.0

The GRI-Mech 3.0 mechanism has been developed for a NG engine so it fits perfectly with this project case. It has been studied and obtained at *The University of California at Berkeley, Stanford University, The University of Texas at Austin, and SRI International*. It is made by 325 chemical reactions with 53 species [8]. Usually the mechanisms are composed by three different files:

- The *mech.dat* in which a list of all the species and the chemical reactions with their relative activation energy are present;

```

! GRI-Mech Version 3.0 7/30/99  CHEMKIN-II format
! See README30 file at anonymous FTP site unix.sri.com,
directory gri;
! WorldWideWeb home page http://www.me.berkeley.edu/gri_mech/
or
! through http://www.gri.org , under 'Basic Research',
! for additional information, contacts, and disclaimer
ELEMENTS
O H C N AR
END
SPECIES
H2      H      O      O2      OH      H2O      HO2      H2O2
C      CH      CH2      CH2(S)  CH3      CH4      CO      CO2
HCO      CH2O      CH2OH      CH3O      CH3OH      C2H      C2H2      C2H3
C2H4      C2H5      C2H6      HCCO      CH2CO      HCCOH      N      NH
NH2      NH3      NNH      NO      NO2      N2O      HNO      CN
HCN      H2CN      HCNN      HCNO      HOCN      HNCO      NCO      N2
AR      C3H7      C3H8      CH2CHO      CH3CHO
END
!THERMO
! Insert GRI-Mech thermodynamics here or use in default file
!END
REACTIONS
2O+M<=>O2+M                                1.200E+
17      -1.000      .00
H2/ 2.40/ H2O/15.40/ CH4/ 2.00/ CO/ 1.75/ CO2/ 3.60/ C2H6/
3.00/ AR/ .83/
O+H+M<=>OH+M                                5.000E+
17      -1.000      .00
H2/2.00/ H2O/6.00/ CH4/2.00/ CO/1.50/ CO2/2.00/ C2H6/3.00/
AR/ .70/
O+H2<=>H+OH                                3.870E+04      2.700
6260.00
O+HO2<=>OH+O2                                2.000E+
13      .000      .00
O+H2O2<=>OH+HO2                            9.630E+06      2.000
4000.00
O+CH<=>H+CO                                5.700E+

```

Figure 4.3: GRI-Mech 3.0 partial mech.dat file.

- The *therm.dat* in which all the thermodynamic properties of the species mentioned before are current;

```

THERMO
  300.000 1000.000 5000.000
! GRI-Mech Version 3.0 Thermodynamics released 7/30/99
! NASA Polynomial format for CHEMKIN-II
! see README file for disclaimer
O      L 1/900  1      G  200.000
3500.000 1000.000  1
  2.56942078E+00-8.59741137E-05 4.19484589E-08-1.00177799E-11
  1.22833691E-15  2
  2.92175791E+04 4.78433864E+00 3.16826710E+00-3.27931884E-03
  6.64306396E-06  3
 -6.12806624E-09 2.11265971E-12 2.91222592E+04 2.05193346E+00
  4
O2     TPIS89O  2      G  200.000
3500.000 1000.000  1
  3.28253784E+00 1.48308754E-03-7.57966669E-07
  2.09470555E-10-2.16717794E-14  2
 -1.08845772E+03 5.45323129E+00 3.78245636E+00-2.99673416E-03
  9.84730201E-06  3
 -9.68129509E-09 3.24372837E-12-1.06394356E+03 3.65767573E+00
  4
H      L 7/88H  1      G  200.000
3500.000 1000.000  1
  2.50000001E+00-2.30842973E-11 1.61561948E-14-4.73515235E-18
  4.98197357E-22  2
  2.54736599E+04-4.46682914E-01 2.50000000E+00
  7.05332819E-13-1.99591964E-15  3
  2.30081632E-18-9.27732332E-22 2.54736599E+04-4.46682853E-01
  4
H2     TPIS78H  2      G  200.000
3500.000 1000.000  1
  3.33727920E+00-4.94024731E-05 4.99456778E-07-1.79566394E-10
  2.00255376E-14  2
 -9.50158922E+02-3.20502331E+00 2.34433112E+00
  7.98052075E-03-1.94781510E-05  3
  2.01572094E-08-7.37611761E-12-9.17935173E+02 6.83010238E-01
  4
OH     RUS 78O  1H  1      G  200.000

```

Figure 4.4: GRI-Mech 3.0 partial therm.dat file.

- The *transport.dat* where additional parameters are present and with whom the diffusivity calculation of each species will be more accurate.

The figures 4.3, 4.4 and 4.5 show the mechanism internal file structure and the same format has been used for the USC-Mech II mechanism.

AR	0	136.500	3.330	0.000	0.000
0.000					
C	0	71.400	3.298	0.000	0.000
0.000 ! *					
C2	1	97.530	3.621	0.000	1.760
4.000					
C2O	1	232.400	3.828	0.000	0.000
1.000 ! *					
CN2	1	232.400	3.828	0.000	0.000
1.000 ! OIS					
C2H	1	209.000	4.100	0.000	0.000
2.500					
C2H2	1	209.000	4.100	0.000	0.000
2.500					
C2H2OH	2	224.700	4.162	0.000	0.000
1.000 ! *					
C2H3	2	209.000	4.100	0.000	0.000
1.000 ! *					
C2H4	2	280.800	3.971	0.000	0.000
1.500					
C2H5	2	252.300	4.302	0.000	0.000
1.500					
C2H6	2	252.300	4.302	0.000	0.000
1.500					
C2N	1	232.400	3.828	0.000	0.000
1.000 ! OIS					
C2N2	1	349.000	4.361	0.000	0.000
1.000 ! OIS					
C3H2	2	209.000	4.100	0.000	0.000
1.000 ! *					
C3H4	1	252.000	4.760	0.000	0.000
1.000					
C3H6	2	266.800	4.982	0.000	0.000
1.000					
C3H7	2	266.800	4.982	0.000	0.000
1.000					
C4H6	2	357.000	5.180	0.000	0.000
1.000					

Figure 4.5: GRI-Mech 3.0 partial transport.dat file.

4.7.2 USC-Mech II

The USC-Mech II mechanism is larger than the GRI which means that contains a superior amount of chemical reactions and consequently the simulation run time is higher. It has been developed by Hai Wang, Xiaoqing You, Ameya V. Joshi, Scott G. Davis, Alexander Laskin, Fokion Egolfopoulos and Chung K. Law, USC Viterbi-Southern University of California. The mechanism contains 111 species and 784 elementary chemical reactions. As previously mentioned the structure of the mechanism files is the same of the GRI-Mech 3.0. [8]

4.8 Ignition Modelling: Source and Sink

A source or a sink term is a scalar function that provides information about the origination or absorption of quantities such as energy, momentum, turbulent kinetic energy, turbulent dissipation rate, species, and passives. CONVERGE allows for the addition of source or sink terms to various transport equations at a specified locations and times within the domain.

The source types are many:

- Energy;
- Momentum U (in the x direction);
- Momentum V (in the y direction);
- Momentum W (in the z direction);
- TKE;
- EPS;
- Species;
- Passive;
- User;
- Porous.

In this thesis work the Energy source type has been used.

Using the energy source type means that the energy value of the source (spark in this case) has to be defined. The maximum temperature value has to be set with the referred starting crank angle and ending crank angle.

The source shapes are many and the most common are:

- Box;
- Sphere;
- Cylinder;
- Circle.

In this specific case the Sphere shape had been used, in particular two spheres of two different dimensions.

The source phenomenon can be subdivided in three different steps, *breakdown*, *arc*, and *glow*, and in order to create a consistent model, according with this phenomenon, two different shapes sizes has been modelled. Thus, to accurately simulate the total spark plug discharge, specify two energy sources between the two electrodes of the spark plug with the following timing considerations are necessary:

- *Breakdown* which occurs earlier and it has a shorter duration;
- *Arc/Glow* which occur after breakdown and it has a longer duration.

The figure 4.6, according with this concept, shows which is the source energy release, while the figure 4.7 shows how the implementation of this concept on the spark plug geometry looks like.

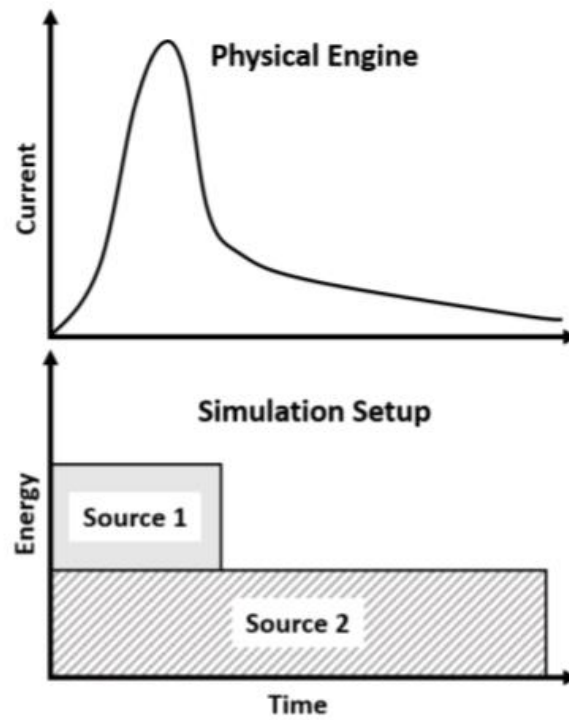
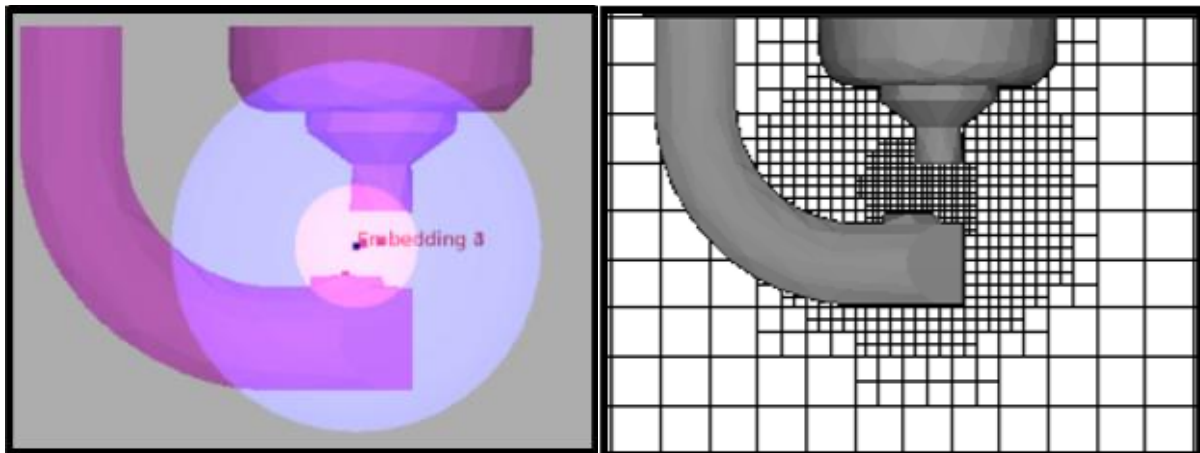


Figure 4.6: Source model.



(a): Source model on the geometry.

(b): additional fixed embedding.

Figure 4.7: Ignition model on the spark plug.

[6]

4.9 Turbulence Modelling

Turbulence significantly increases the rate of mixing of momentum, energy and species. For most of the applications, obtain an accurate CFD simulation results without including a turbulence model, is really difficult.

Turbulent mixing is a convective process that results from the presence of turbulent eddies and flow. These vortexes are fundamental and if a CFD solver does not contain a discretized domain able to solve the smallest eddy length scales, the software cannot catch entirely the phenomenon. Currently, it is not practical to resolve all of the length scales in a typical CFD simulation, and thus turbulence models are used to account for the additional mixing.

As previously mentioned, in this thesis project only the RANS (Reynolds-Average-Navier-Stokes) equations has been used with the RNG (Renormalization Group) $k - \varepsilon$ as turbulence model. This model is based on two RANS model equations with whom the flow variables, for example the velocity, are splitted into an ensemble average and a fluctuating term as follows:

$$u_i = \bar{u}_i + u'_i \quad (4.18)$$

Where u_i is the instantaneous velocity, \bar{u}_i is the ensemble average velocity and u'_i is the fluctuating velocity.

In order to compute the RANS transport equations and averaging, the equation 4.18 has to be substitute into the mass conservation equation and the momentum equation, obtaining as follow:

$$\frac{\partial \bar{\rho}}{\partial t} + \frac{\partial \bar{\rho} \bar{u}_i}{\partial x_i} = 0 \quad (4.19)$$

and

$$\frac{\partial \bar{\rho} \tilde{u}_i}{\partial t} + \frac{\partial \bar{\rho} \tilde{u}_i \tilde{u}_j}{\partial x_j} = -\frac{\partial \bar{P}}{\partial x_i} + \frac{\partial}{\partial x_j} \left[\mu \left(\frac{\partial \tilde{u}_i}{\partial x_j} + \frac{\partial \tilde{u}_j}{\partial x_i} \right) - \frac{2}{3} \mu \frac{\partial \tilde{u}_k}{\partial x_k} \delta_{ij} \right] + \frac{\partial}{\partial x_j} (-\bar{\rho} \widetilde{u'_i u'_j}) \quad (4.20)$$

Where \tilde{u}_i is called Favre average and it can be written as:

$$\tilde{u}_i = \frac{\overline{\rho u_i}}{\bar{\rho}} \quad (4.21)$$

The ensemble average velocity of the equation generates new terms named Reynolds stresses which represent the turbulence effect. These stresses are expressed as follow:

$$\tau_{ij} = -\bar{\rho} \widetilde{u'_i u'_j} \quad (4.22)$$

And they are already included in the equation 4.20.

The RANS model, basing on the same concept, can be subdivided in many ways to express and compute the Reynolds stress:

- $k - \varepsilon$ Models;
- $k - \omega$ Models;
- RANS Boundary Conditions;
- RANS input Parameters.

In this thesis work, only the $k - \varepsilon$ Models will be used and described.

4.9.1 k - ε Models

The k - ε models are based on the RANS model and, specifically, they use an effective turbulent viscosity as model Reynolds stress term. In this way, the turbulent convective mixing will be modelled with an additional turbulent diffusion.

The k - ε models are many and any of them use a different concept to compute the additional Reynolds stress. The main models are:

- Standard and RNG k - ε Models;
- Rapid Distortion RNG k - ε Model;
- Realizable k - ε Model.

Traditionally the *Standard and RNG k - ε Model* is the most important and used, consequently in this thesis project, it will be the only one described.

[6]

Standard and RNG k - ε Models

The relation that express the Reynolds stress with the *Standard and RNG k - ε Models* is:

$$\tau_{ij} = -\bar{\rho} \widetilde{u'_i u'_j} = 2\mu_t S_{ij} - \frac{2}{3} \delta_{ij} \left(\rho k + \mu_t \frac{\partial \tilde{u}_i}{\partial x_i} \right) \quad (4.23)$$

Where k is the kinetic energy and it is written as:

$$k = \frac{1}{2} u'_i u'_i \quad (4.24)$$

Where the μ_t is the turbulent viscosity and it is defined as:

$$\mu_t = c_\mu \rho \frac{k^2}{\varepsilon} \quad (4.25)$$

In the equation 4.25 there is the parameter ε that is called dissipation of turbulent energy and it a value modifiable in order to tune a particular flow.

The strain tensor S_{ij} holds:

$$S_{ij} = \frac{1}{2} \left(\frac{\partial \tilde{u}_i}{\partial x_j} + \frac{\partial \tilde{u}_j}{\partial x_i} \right) \quad (4.26)$$

This model uses the turbulent conductivity and turbulent diffusion terms to take in account the presence of turbulence in mass transport and energy transport. The turbulent diffusion and conductivity terms can be written:

$$D_t = \left(\frac{1}{Sc_t} \right) \mu_t \quad (4.27)$$

And

$$k_t = \left(\frac{1}{Pr_t} \right) \mu_t c_p \quad (4.28)$$

Where D_t is the turbulent diffusion, Sc_t is the Schmidt Number which is a value usually fixed at 0.78 but in some cases increase or decrease it could help because it decreases or increases the diffusivity, k_t is the turbulent conductivity, and Pr_t is the Prandtl Number which is usually fixed at 0.9.

Since the RANS $k - \varepsilon$ model requires two additional transport equations to be able to solve the turbulent viscosity of the equation 4.25, one equation for the turbulent kinetic energy k and one equation for the dissipation of turbulent kinetic energy ε are necessary. The turbulent kinetic energy transport equation holds:

$$\frac{\partial \rho k}{\partial t} + \frac{\partial \rho k u_i}{\partial x_i} = \tau_{ij} \frac{\partial u_i}{\partial x_j} + \frac{\partial}{\partial x_j} \frac{\mu + \mu_t}{Pr_k} \frac{\partial k}{\partial x_j} - \rho \varepsilon + \frac{C_s}{1.5} S_s \quad (4.29)$$

Where parameter 1.5 is an empirical value.

While, the transport equation for the dissipation of turbulent kinetic energy is:

$$\frac{\partial \rho \varepsilon}{\partial t} + \frac{\partial (\rho u_i \varepsilon)}{\partial x_i} = \frac{\partial}{\partial x_j} \left(\frac{\mu + \mu_t}{Pr_\varepsilon} \frac{\partial \varepsilon}{\partial x_j} \right) + C_{\varepsilon 3} \rho \varepsilon \frac{\partial u_i}{\partial x_i} + \left(C_{\varepsilon 1} \frac{\partial u_i}{\partial x_j} \tau_{ij} - C_{\varepsilon 2} \rho \varepsilon + C_s S_s \right) \frac{\varepsilon}{k} + S - \rho R \quad (4.30)$$

Where S is called user-supplied source and S_s is the source term which represents discrete phases interaction as the spray. The $C_{\varepsilon 1}$ terms are constant which represent the compression and expansion phase. On the other hand, for the *RNG $k - \varepsilon$ Model* R can be written as:

$$R = \frac{c_\mu \eta^3 \left(1 - \frac{\eta}{\eta_0}\right) \varepsilon^2}{(1 - \beta \eta^3) k} \quad (4.31)$$

Where η is:

$$\eta = \frac{k}{\varepsilon} S_{ij} = \frac{k}{\varepsilon} \sqrt{2 S_{ij} S_{ij}} \quad (4.32)$$

[6]

4.10 Mesh Settings

In this thesis project, since it is a continuation of a previous work, as already cited above, the best compromise shown has been used. In particular, the “*fine*” mesh has been modelled changing some values in order to fit it to this different case.

4.10.1 Base Mesh Settings

The base mesh chosen is defined by a mesh size equal to: $dx = 0.004\text{ m}$, $dy = 0.004\text{ m}$, $dz = 0.004\text{ m}$.

4.10.2 Fixed Embedding Settings

The fixed embedding features are shown in the table 4.2 and the lowest value of mesh size is 1 mm.

Name	Type	Mode	Scale
Head	Boundary	Permanent	2 (2 layers)
Liner	Boundary	Permanent	2 (2 layers)
Piston	Boundary	Permanent	2 (2 layers)
Intake Valve Top	Boundary	Cyclic (340-600 deg)	3 (2 layers)
Intake Valve Angle	Boundary	Cyclic (340-600 deg)	3 (2 layers)
Intake Valve Bottom	Boundary	Permanent	3 (2 layers)
Exhaust Valve Top	Boundary	Cyclic (130-380 deg)	3 (2 layers)
Exhaust Valve Angle	Boundary	Cyclic (130-380 deg)	3 (2 layers)
Exhaust Valve Bottom	Boundary	Permanent	3 (2 layers)
Spark Plug 1	Sphere (r=0.005 m)	Cyclic (690-750 deg)	4
Spark Plug 2	Sphere (r=0.003 m)	Cyclic (690-730 deg)	5
Intake Port Top	Boundary	Cyclic (340-600 deg)	2 (2 layers)
Intake Port Bottom	Boundary	Cyclic (340-600 deg)	2 (2 layers)
Exhaust Port	Boundary	Cyclic (130-380 deg)	2 (2 layers)
Cylinder	Cylinder	Permanent	2

Table 4.3: Fixed Embedding Settings.

4.10.3 Adaptive Mesh Refinement Settings

For what matters the AMR settings the main characteristics are shown in the following table 4.3 and the minimum mesh size referred to these settings is 0.5 mm.

	Mode	Max. Embedding Level Velocity	Sub-Grid Criterion Velocity	Max. Embedding Level Temperature	Sub-Grid Criterion Temperature
Cylinder	Permanent	4	3.5	4	2.5
Intake System	Permanent	3	3.5	-	-
Exhaust System	Cyclic (380- 720 deg)	2	3.5	2	2.5

Table 4.4: Adaptive Mesh Refinements (AMR) Settings.

In this particular mesh setting a modification, respect to the previous project model, has been done. Since in this thesis work the operating points have a higher load and higher velocity, the AMR settings have to be different otherwise the number of cells into the domain can be too much for the computational power available. In particular the Sub-Grid criterion velocity has been changed from 1 m/s to 3.5 m/s.

This particular mesh setting suffered of some modifications during the project in order to find the perfect balance between simulation run time and result resolution. It will be described in the following chapter.

5. Results

5.1 Introduction

In this chapter the model validation of all the results obtained will be described and an engine operation point subdivision will take place. As previously mentioned, all the simulation results will be compared with the experimental measurements in order to define if the model behavior can predict approximately the real engine in a specific condition demarcated by the engine operating point.

The model validation will be obtained looking and comparing the followings parameters:

- *Pressure curve in the cylinder*: comparison between the simulation closest cycle to the ensemble average with the experimental closest, maximum and minimum cycle which define the validity range where the simulation has to be considered valid. Additionally, a scatter plot and the trend line computed by the 100 experimental cycles will help to determine the peak location validity range.
- *HRR (Heat Release Rate)*: As mentioned above, the results of the HRR calculation by the Octave scripts will be compared with the experimental data using the same method explained for the pressure curve.
- *IHR (integrated Heat Release)*: As previously described, the IHR will be compared, through the Octave script, to the experimental data. The burn duration will be also used to obtain the model validation.

5.2 Operating point 4600x7.9x1 (NG)

For what concern the operating point 4600[rpm]x7.9[bar]x1[lambda], all the tests and the simulations run, in order to finally obtain the model validation, will be described in details comparing the parameters, cited above, with the experimental data. In particular all the cases, that will be shown, present the same model features and some modifications, when they will be necessary, will be motivated. Specifically, all the following cases will be run using the GRI III Mechanism because it is the best one to simulate the natural gas combustion. The fuel composition of this specific operating point is, as mentioned above, a mixture of methane gas and other species:

- $\text{CH}_4 = 98\%$
- $\text{C}_2\text{H}_6 = 1\%$
- $\text{CO}_2 = 1\%$

5.2.1 Base Simulation

According to the model shown above a first simulation has been run in order to figure which could be the first problems to fix to obtain the model validation out.

In the figures 5.1 is shown the pressure in the cylinder for this particular case.

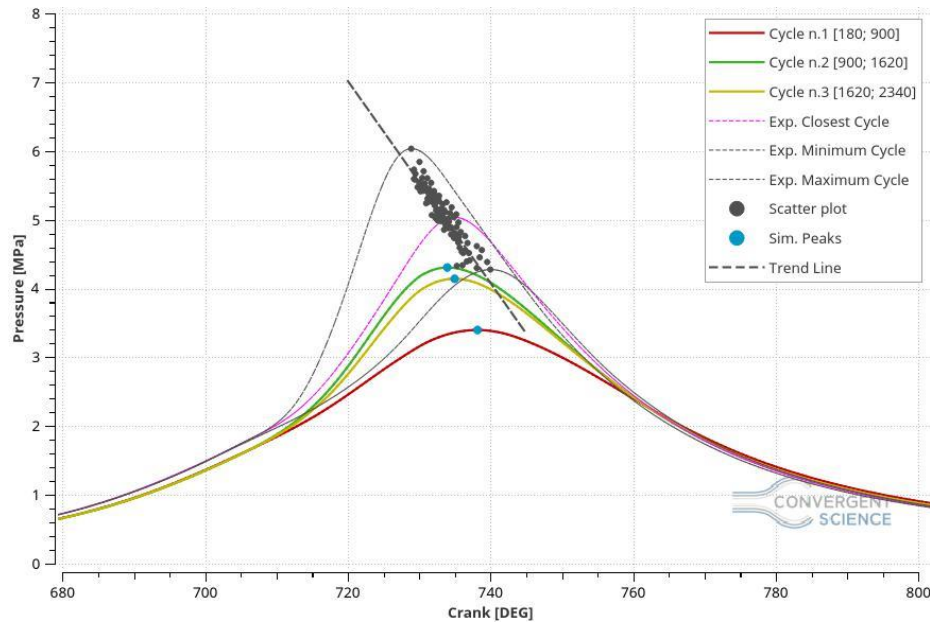


Figure 5.1: Pressure in Cylinder, Base Simulation.

From the picture 5.1 some problems in the model can be found. In particular the main visible issues on this plot are:

- The model compression phase does not match the experimental data;
- The peaks location is shifted and they are not following the trend line;
- The peak values are underestimated.

These are the main issues and, with the following simulations and modifications, we are going to analyze and solve them.

Firstly, making a zoom on the compression phase zone, appreciate the compression phase error between the model and the experimental measurement is easier.

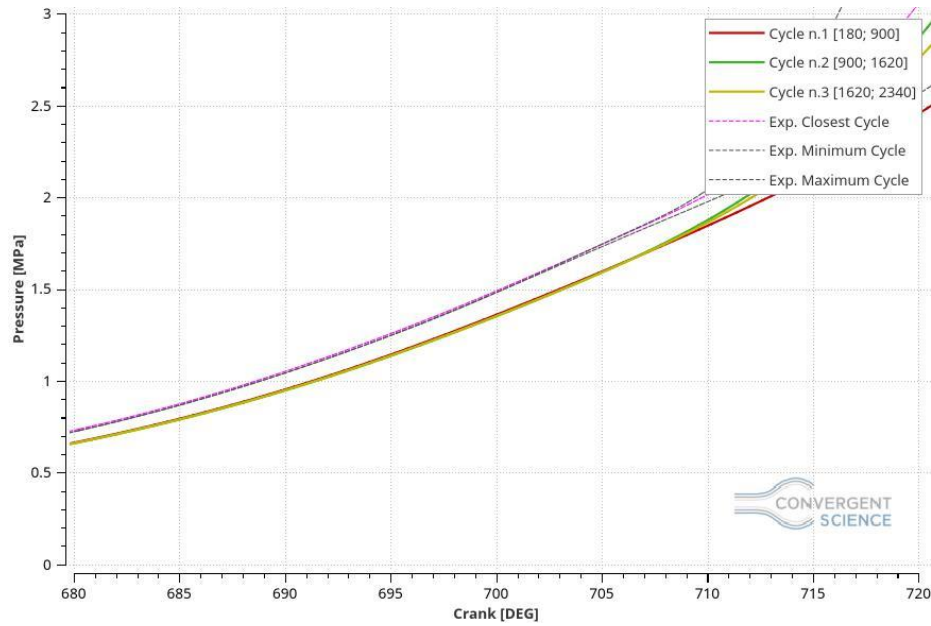


Figure 5.2: Pressure in cylinder, base simulation zoom.

In order to determine the error amount, the values have to be referred to a common point. In this case the spark advance crank angle (695 DEG) has been taken in account and the compression phase error is equal to 8.96%. Unfortunately, this issue is not acceptable and some case setup modification must be done.

The figure 5.3 and 5.4 show the AHRR and the AIHR respectively.

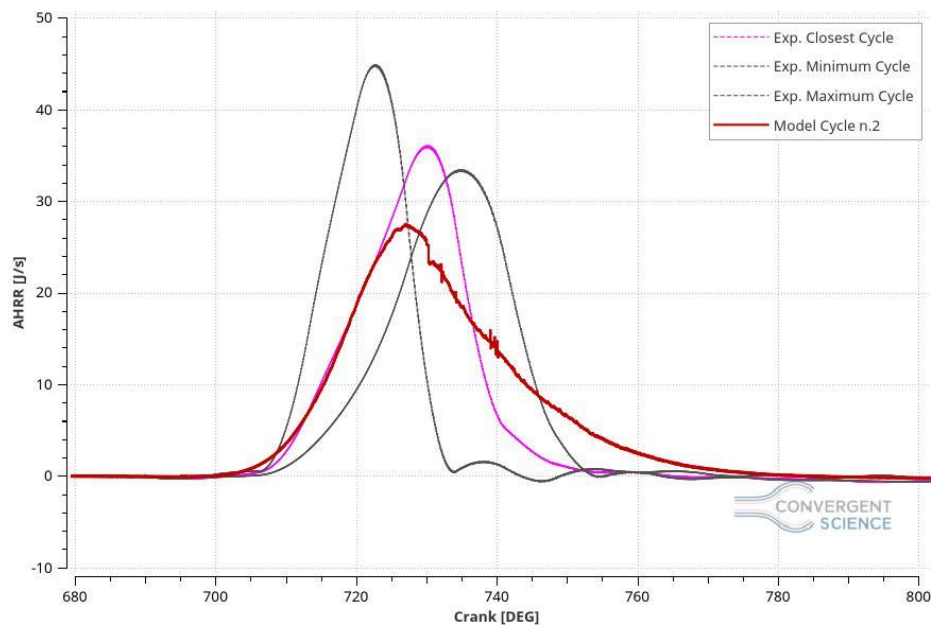


Figure 5.3: AHRR, base simulation.

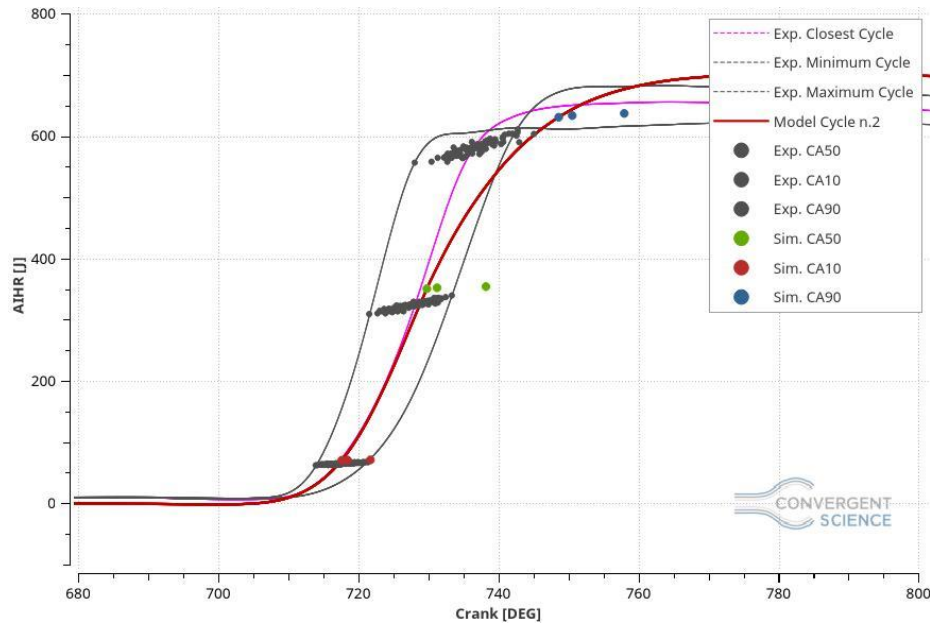


Figure 5.4: AIHR, base simulation.

From the figure 5.3, another issues has been found: the graph tail is too high, the combustion is too long and, consequently, the burn duration is longer than the measurements of a value equal to 31.7%.

On the other hand, the figure 5.4 shows the AIHR where the experimental and simulation values of 10, 50 and 90 percent of burned mass are exposed.

Finally, comparing the model trapped mass with the experimental data one, the error obtained is equal to -1.02% which means that the simulation trapped mass turns out to be 1.02% less than the measurements.

This simulation has been run with 4 nodes which means 4 cores per node (machine), for a core total amount of 16 and the run time is equal to 170.94 hours.

5.2.2 Boundary Conditions Manipulation

Since the compression phase is one of the most important phases in an engine cycle to obtain a perfect combustion, it has been decided to focus on it at first to go on with the combustion and all the other problems in a second time.

Several cases with many modifications to erase the compression phase error has been run. Unfortunately, none of them gave an improvement and, in the majority of cases, the results were even worse than the base simulation.

Taking into consideration this concept, it has been decided to increase the pressure boundary condition profile of a value equal to 8.96%, to be sure to match the experimental data during the compression phase. In order to conserve the mass in the cylinder, increase also the inflow temperature from the value of 313 K to 353 K has been necessary. In particular, the temperature of 353 K is a real temperature taken from another excel sheet of the same operating point with the same load conditions.

This approximation can be considered acceptable because the pressure boundary conditions do not derive from a measurement operation, but instead they have been computed by using a MatLab script.

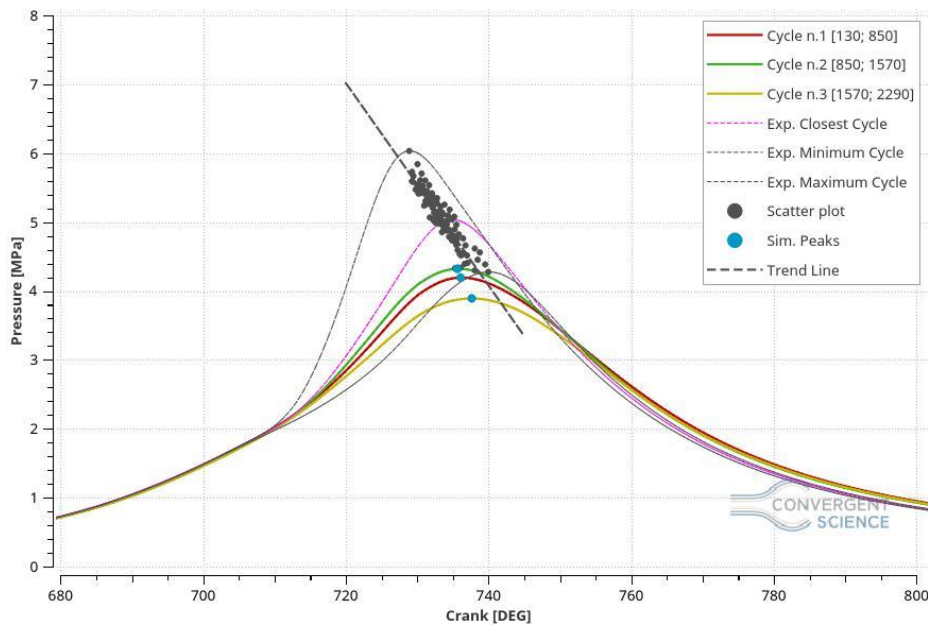


Figure 5.5: Pressure in Cylinder with boundary conditions increased.

The figure 5.5 shows the pressure in the cylinder of this particular case and, zooming on the compression phase, the error is disappeared.

The peaks locations and the pressure peak values are still shifted and lower than the experimental data, which means that other model modifications must be done.

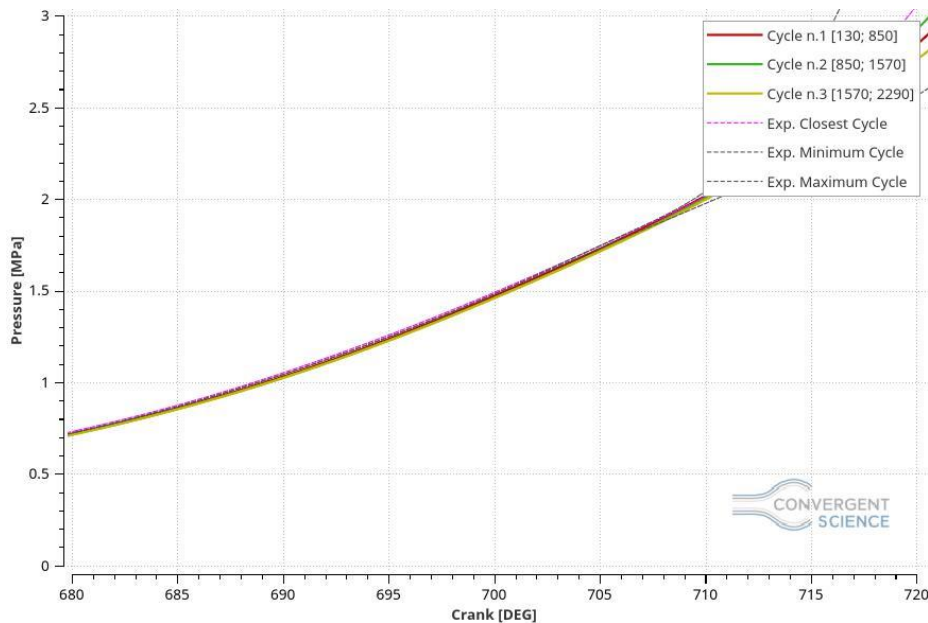


Figure 5.6: Pressure in the Cylinder with Boundary Conditions Increased zoom.

In particular, as the figure 5.6 shows, the compressor phase error, at the SA crank angle, moved from 8.95% to 1.71% that is acceptable.

In this case the trapped mass is lower and the error is equal to 0.01% which means that the model is perfectly matching the measurements.

In the figure 5.7 and 5.8 the AHRR and the AIHR are displayed.

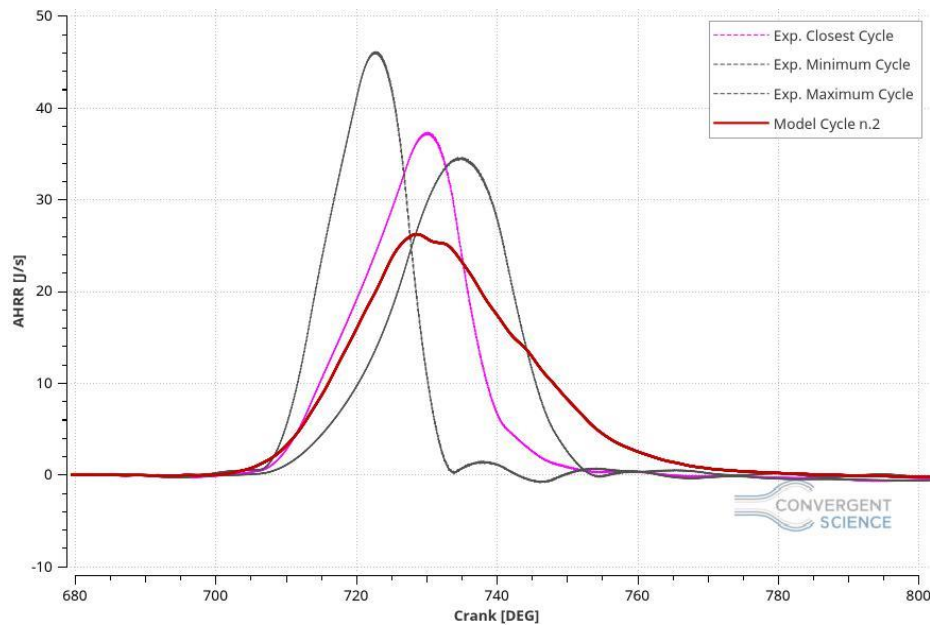


Figure 5.7: AHRR with boundary conditions increased.

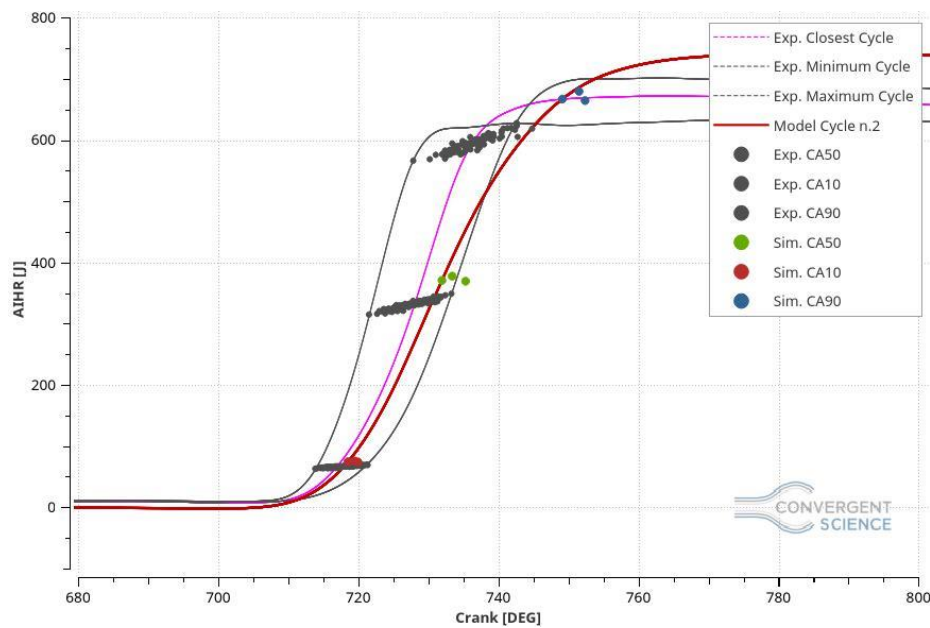


Figure 5.8: AIHR with boundary conditions increased.

As the figure 5.7 exposed, the model HRR tail is still longer and higher than the measurements, this affects the burn duration and, consequently, the crank angle where the 50% and 90 % of the fuel mass is burned. In particular, the burning duration error is higher than the previous simulation and the value is equal to 36.3%, which means that the combustion simulated, from CA10 to CA90, is 36.3% longer than the experimental data.

This simulation employed 155.7 hours and it has been run on 6 nodes which means on 24 cores.

5.2.3 Mesh Sensitivity

Once the problem in the compression phase has been solved, the attempt has been made to shift the peaks location, in order to get closer to the trend line, and to increase the pressure peak values, since they are outside than the validity range and because they are underestimating the experimental values.

In order to do that, firstly, a mesh sensitivity has been analyzed to understand if an increasing of the number of cells can make the difference in the results. In particular, the minimum mesh size remained the same (equal to 0.5 mm) but, by means a change the AMR sub grid criterion velocity (SGS), increase the number of cells has been possible.

By changing the AMR SGS, from 3.5 to 2 or 1 m/s, the number of cells increase considerably and, with more cells, all the turbulent phenomena can be catch better by obtaining a more valid model. Unfortunately, the run-time increased significantly as well and a trade off between a more accurate resolution of the model and a convenient computational run time has to be found.

In addition to the previous case, two more simulations have been run, in particular with SGS equal to 2 and 1 m/s.

AMR Sub Grid Criterion Velocity equal to 2

For what matters the case with the AMR manipulation, the results are shown in the figures 5.9, 5.10 and 5.11.

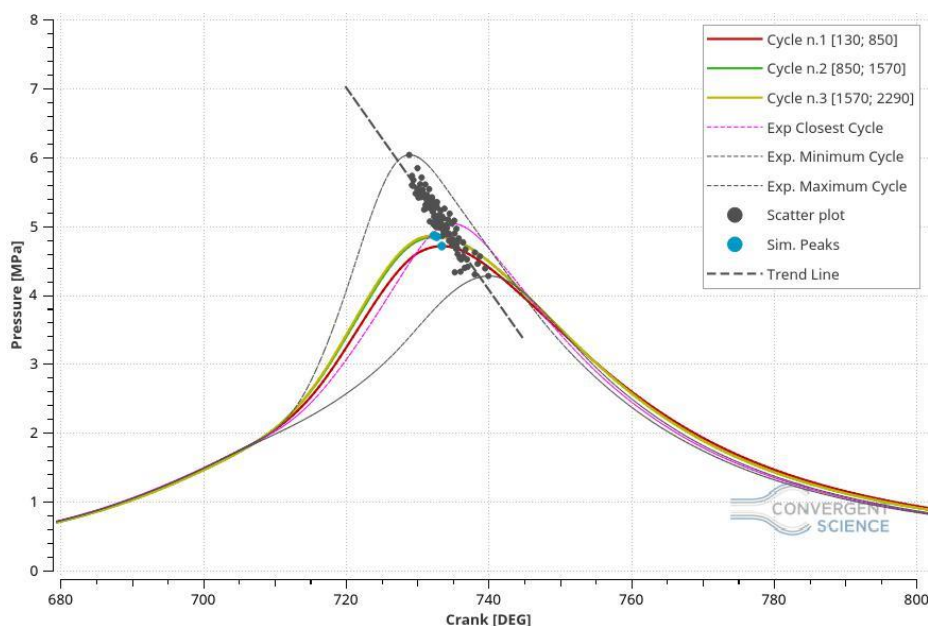


Figure 5.9: Pressure in Cylinder, SGS equal to 2 m/s.

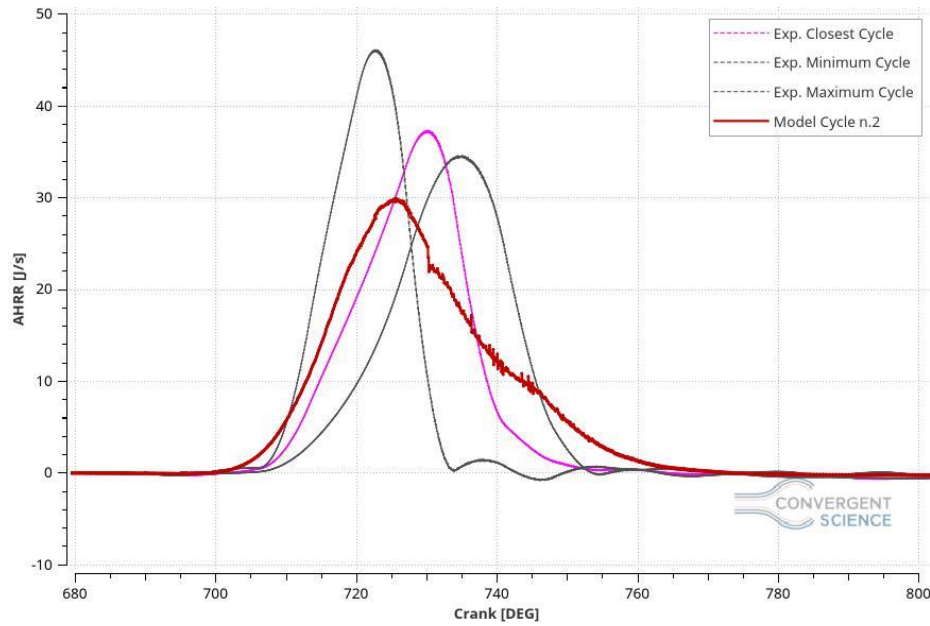


Figure 5.10: AHRR, SGS equal to 2 m/s.

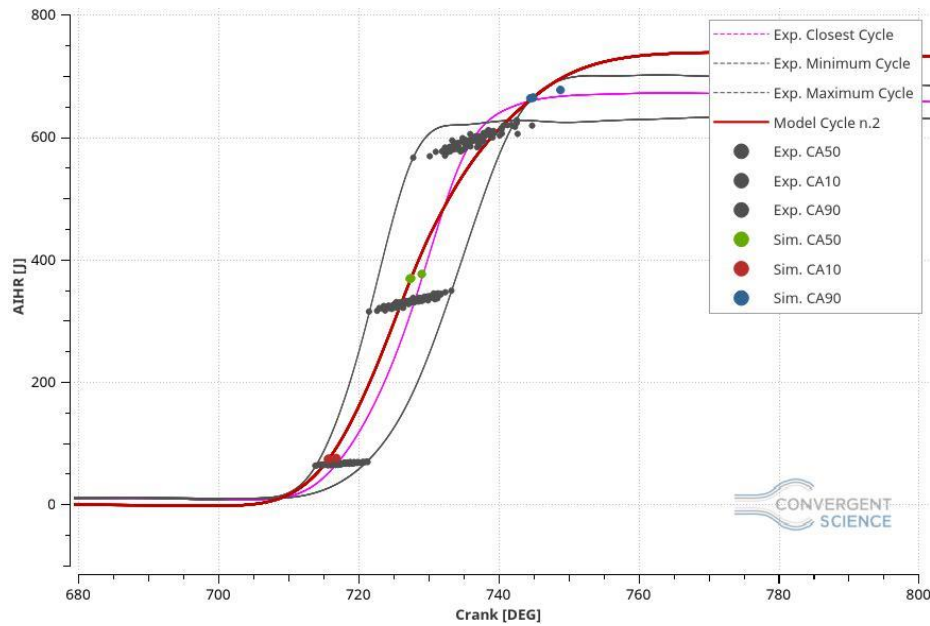


Figure 5.11: AIHR, SGS equal to 2 m/s.

In the figure 5.9 the peak location is closer to the trend line, which means that the combustion velocity is improving in the right direction. The pressure peak values increased, comparing them with the previous simulation, and this behaviour could be associated to an increment of the turbulence in the combustion chamber due to the higher number of cells.

Unfortunately, the AHRR and the AIHR show that the combustion is still longer than the measurements and the energy in the system is higher than the maximum cycle, so other corrections have to be done. In particular, the burn duration of this case is 33.45% longer than the experimental data.

In this simulation the run time was 69.68 hours and it has been computed by special cluster machines made by 20 cores for each node. Specifically, this case has been run on 3 nodes that correspond on 60 cores.

AMR Sub Grid Criterion Velocity equal to 1 m/s

For what concern this particular case the following figures show the results.

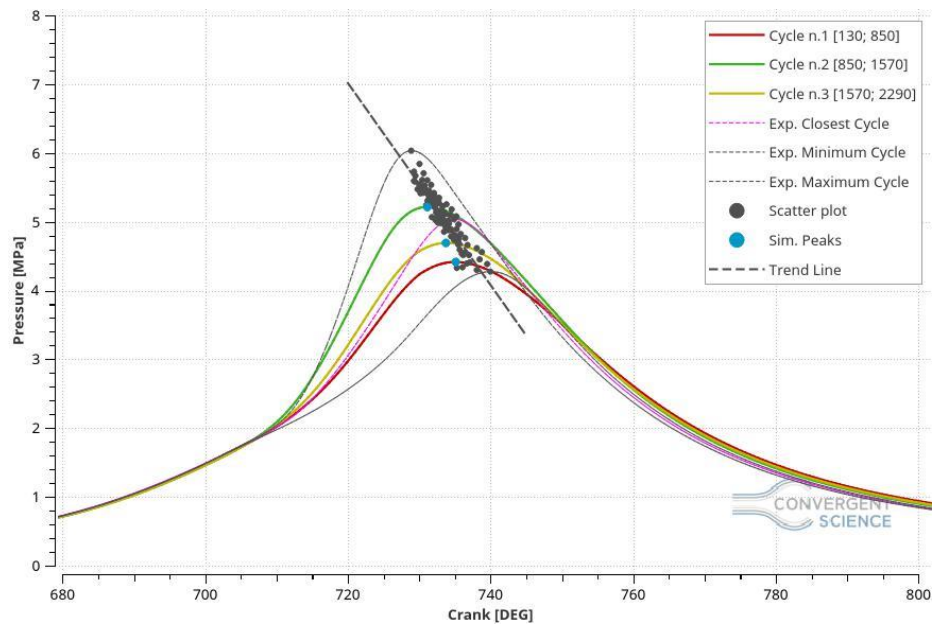


Figure 5.12: Pressure in Cylinder, SGS equal to 1 m/s.

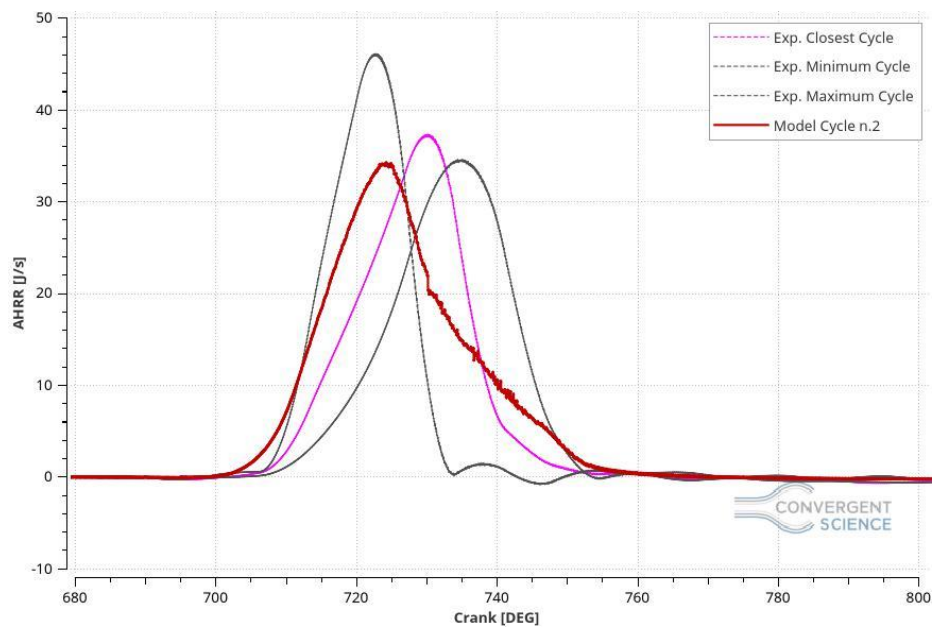


Figure 5.13: AHRR, SGS equal to 1 m/s.

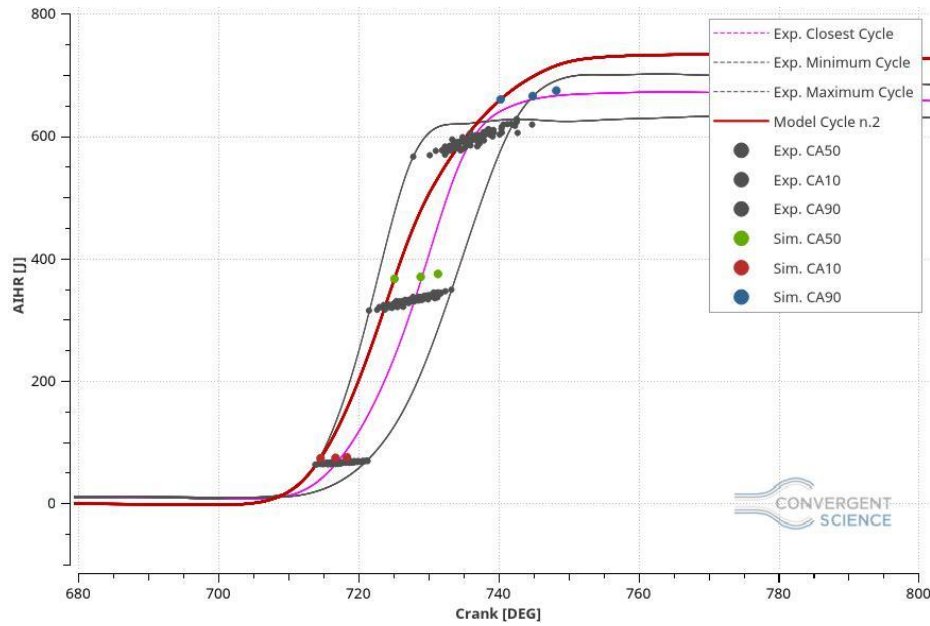


Figure 5.14: AIHR, SGS equal to 1 m/s.

The figure 5.12 shows the pressure in the cylinder and, thanks to that plot, the pressure peak locations improvement is easy to see. In particular the pressure peaks are close enough to the trend line to be defined acceptable. Likewise, the pressure peak values are inside of the CCV range, thus they can be considered adequate as well.

However, the AHRR does not possess improvements on the tail shape and the combustion starts too early and finish too late giving a burn duration longer of 30.5% than the measurements in terms of crank angles.

This simulation employed 94.25 on 3 nodes with 60 cores. Unfortunately, these kinds of special machines were not always available, thus, just few simulations have been run on them. In particular, this case was impossible to run on normal machines made by 4 cores for each node because the number of cells was too high and multiple crashes has been obtained.

Comparisons

The figures 5.15, 5.16 and 5.17 display the comparisons between the three cases analyzed until now, especially the three cases with a value of AMR SGS equal to 3.5, 2 and 1 m/s respectively. In order to obtain the following comparisons, the best cycles of each simulation, given by the closest cycles to the ensemble average cycle, have been taken in account.

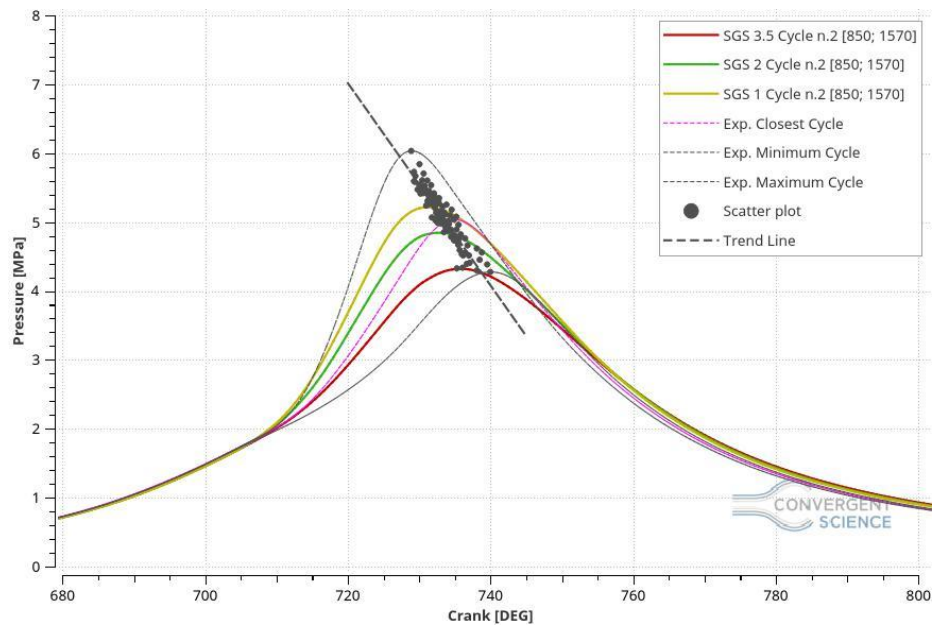


Figure 5.15: Mesh Sensitivity Pressure Comparison.

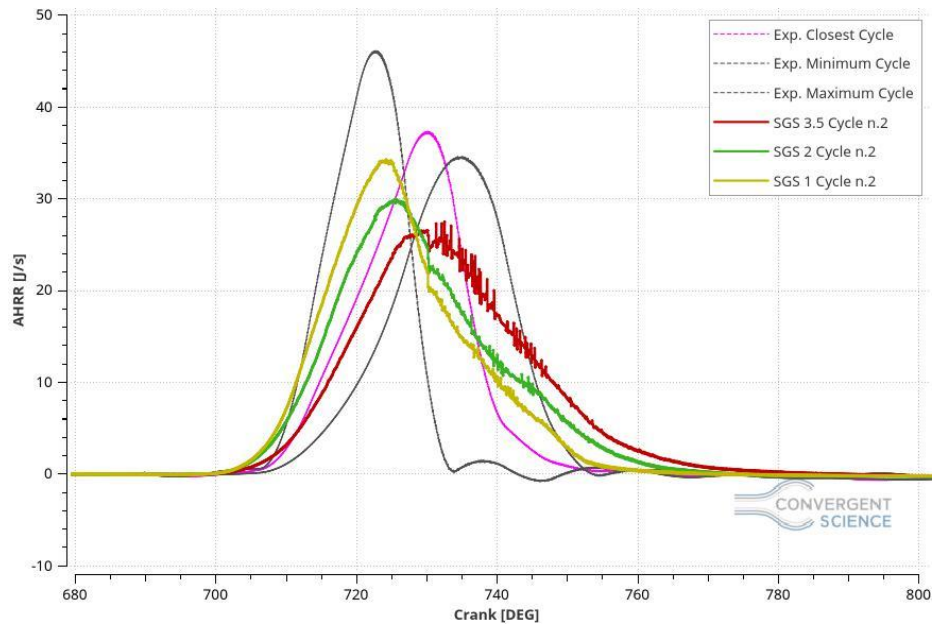


Figure 5.16: Mesh Sensitivity AHRR Comparison.

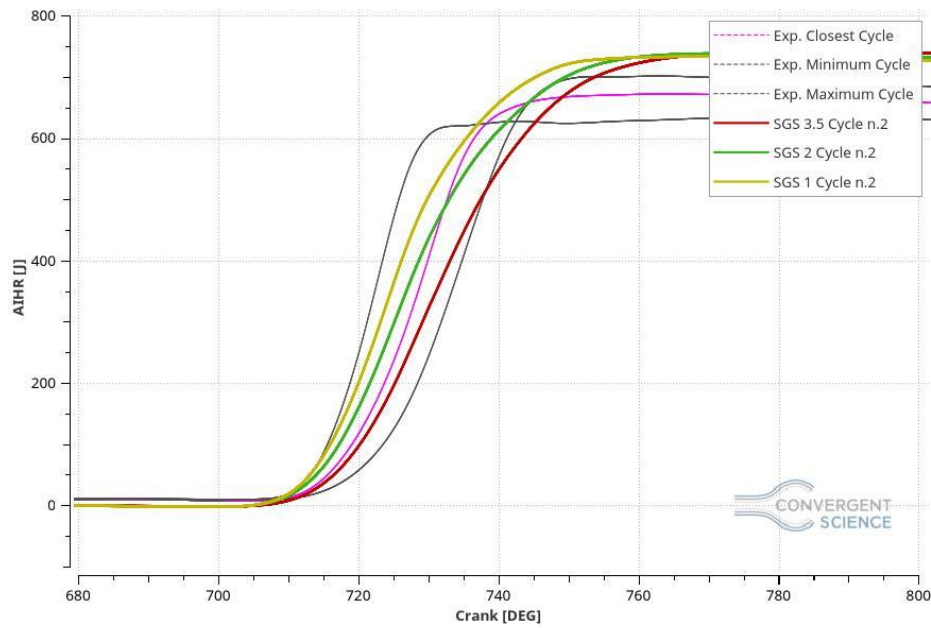
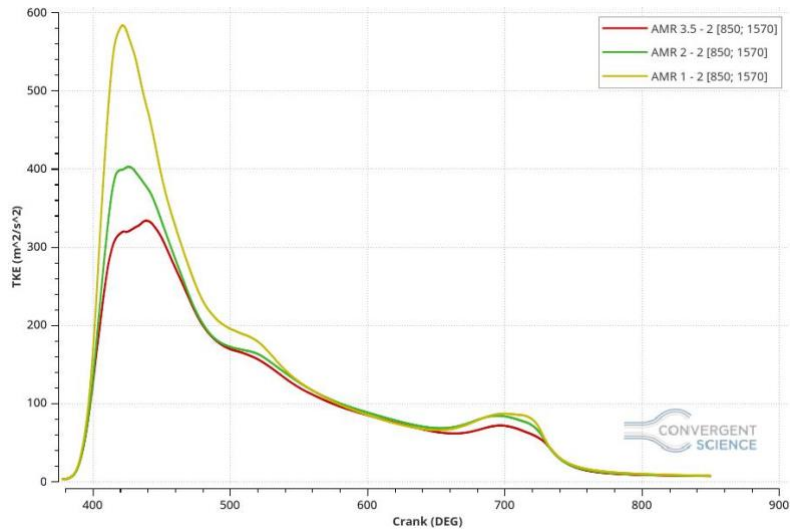


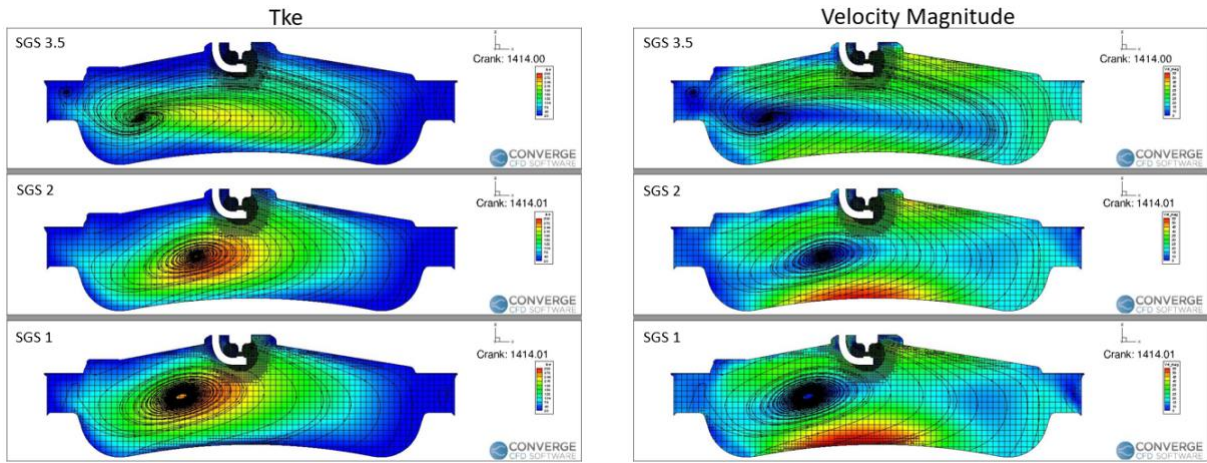
Figure 5.17: Mesh Sensitivity AIHR Comparison.

An improvement, with the increasing of the SGS value, can be notice in all the charts, especially on the pressure peak location and on the AHRR shape.

This development can be associated to the increase of the turbulence magnitude due to the cells number rise. In the Figure 5.18 and 5.19 will be analyzed the number of cells in the domain and the turbulence magnitude of these cases in order to define a trade off between a high model resolution and acceptable simulation run time.



(a): Turbulence Comparison.

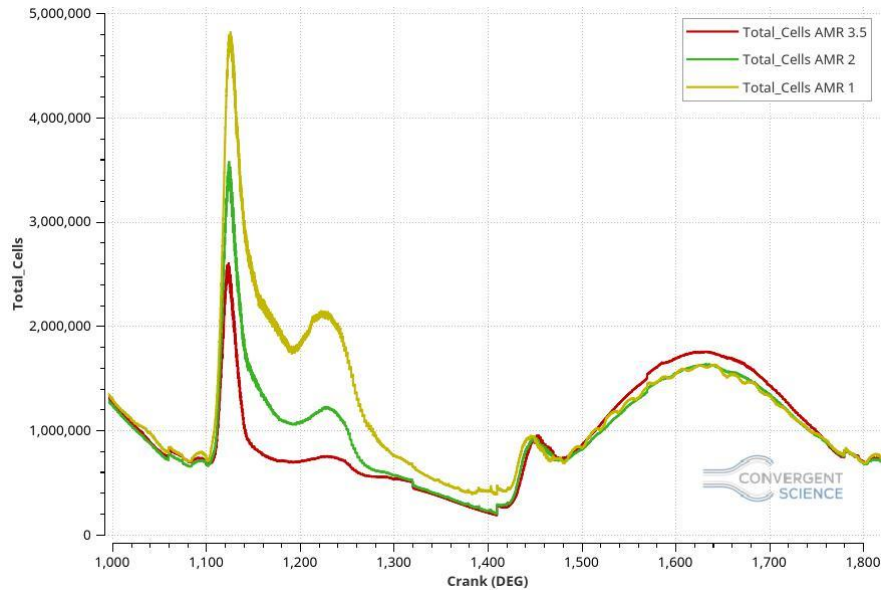


(b): Comparison of TKE in the chamber before the combustion phase.

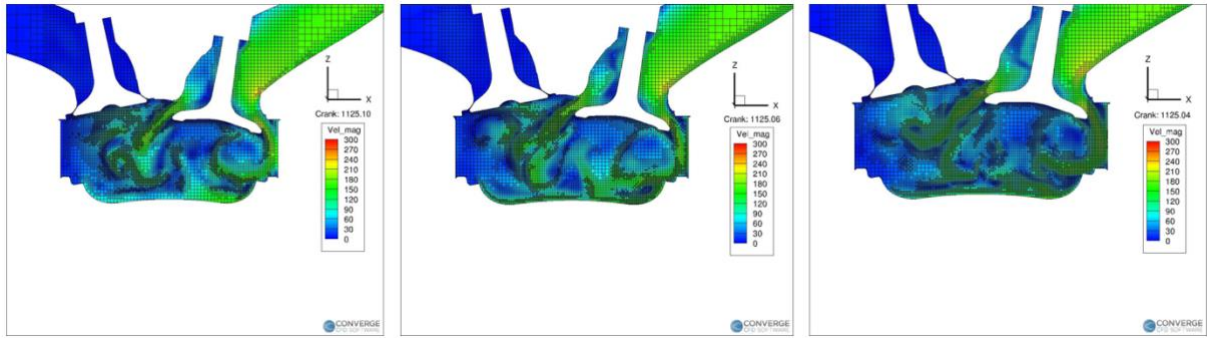
(c): Comparison of the Velocity Magnitude in the chamber before the Combustion phase

Figure 5.18: Turbulence Magnitude Comparison

In the figure 5.18 the changing of the turbulence magnitude is easy to see, especially there is a considerable relation between the number of cells and the turbulence value. Since a high turbulence in the chamber is fundamental to obtain a fast combustion, the correct balance between a high simulation results resolution and an acceptable simulation run time is needed. The right compromise should be the case with the AMR sub grid criterion velocity equal to 2 m/s but, unfortunately, these simulations have been run on a special cluster that was not always available and, consequently, these cases cannot be calculated by normal computer due to the hazardous number of cells shown on the figure 5.18. For this reason, the trade off has been forced on the case with AMR SGS equal to 3.5 m/s.



(a): Number of Cells Comparison.



(b): SGS 3.5 m/s, cells during the aspiration phase.

(c): SGS 2 m/s, cells during the aspiration phase.

(d): SGS 1 m/s, cells during the aspiration phase.

Figure 5.19: Cells in the domain.

As the figure 5.19 shows the number of cells in the domain can reach the hazardous value of 5 million for the SGS 1 m/s case and 3.5 million in the SGS 2 m/s case that are over the normal computer capability and the run time could be more than 10 days long for a three cycles simulation.

5.2.4 Schmidt Number Sensitivity

Furthermore, to adjust the pressure peak location and magnitude, avoiding the use of a too fine mesh, the Schmidt number tuning has been definite. In particular, as previously mentioned, the Schmidt Number is a dimensionless numerical value able to increase or decrease the mass diffusivity. It is defined by the following relation in which compare the kinematic viscosity [m^2/s]:

$$D = \frac{\nu}{Sc} \quad (5.1)$$

From the equation 5.1, the Schmidt Number role is easy to imagine. Generally speaking, an increase of the Schmidt Number value causes a decrease on the mass diffusivity value, consequently, it makes the combustion slower. Conversely, a diminution of the Schmidt Number causes a rise of the mass diffusivity achieving a faster combustion. The normal Schmidt Number value is fixed at 0.78 but, for this particular case, two additional simulation, with the value equal to 0.75 and 0.70, have been run.

Schmidt Number Equal to 0.75

The figures 5.20, 5.21 and 5.22 show the results of this current simulation.

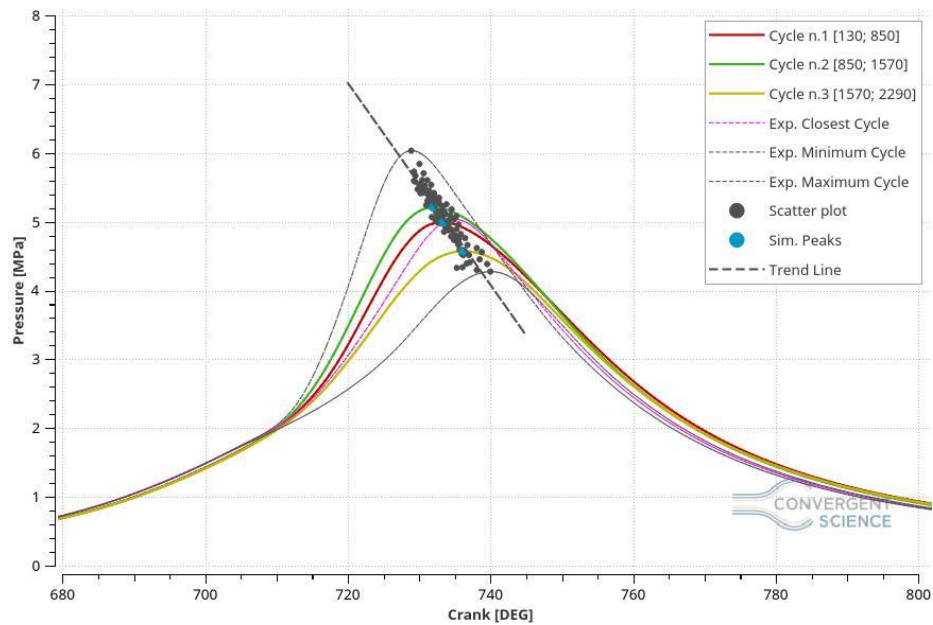


Figure 5.20: Pressure in Cylinder, Schmidt Number equal to 0.75.

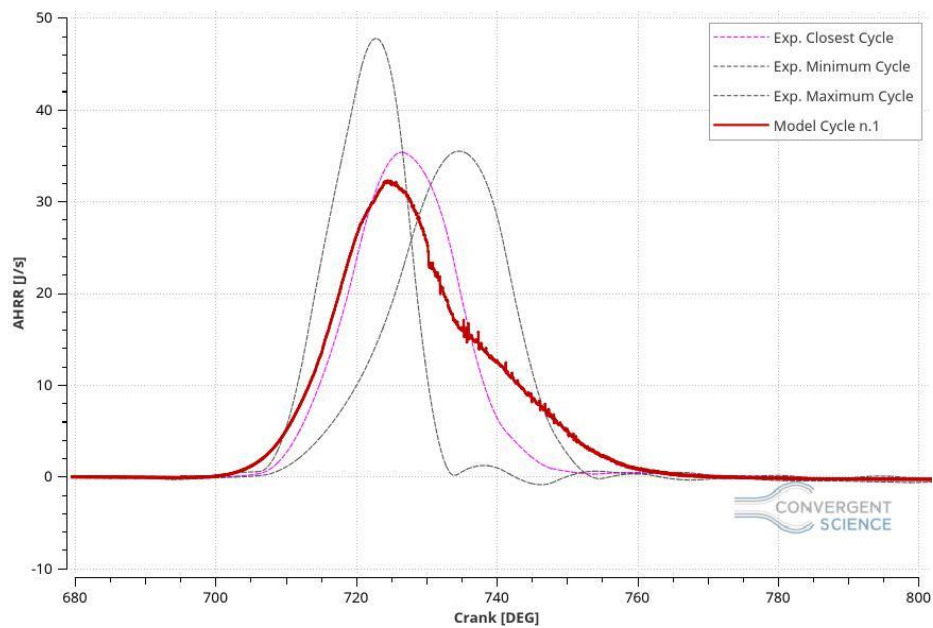


Figure 5.21: AHRR, Schmidt Number equal to 0.75.

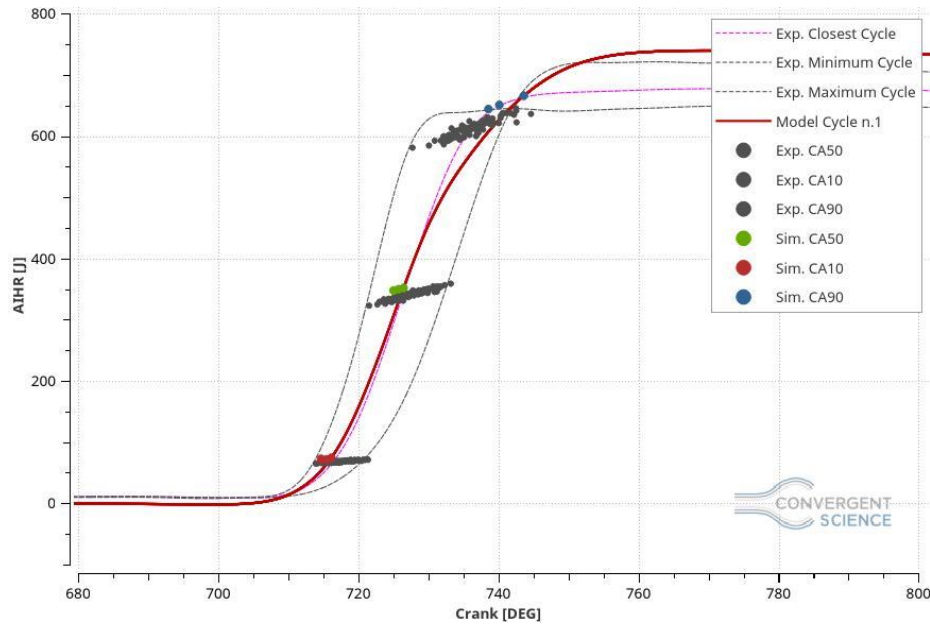


Figure 5.22: AIHR, Schmidt Number equal to 0.75.

As expected, in the figure 5.20, the pressure peaks are perfectly following the trend line, thus it is possible to assert that the peak location is acceptable. The same can be declare for the pressure peak magnitude since they are inside of the CCV range made by the 100 experimental cycles. Conversely, the same affirmation cannot be assert for the AHRR curve because the tail results still high at the end of the combustion, which means that the model is not predictive yet and some others modifications have to be done in order to fix it.

The trapped mass error in the chamber before the combustion phase is equal to 0.36% which means that the mass value is acceptable.

Even if the AHRR tail is high, giving a longer combustion than the measurements, the simulation statistic burn duration error is only 2.26% longer in terms of crank angles. This is an important improvement which assert that the alterations made in the model case setup are leading, step by step, to the validation of the model.

In the figure 5.22 it is possible to see that the CA50 and CA90 crank angles are closer to the experimental data ones, comparing to the previous simulations, but the energy in the system is still too high.

This simulation has been run on 6 cores machines, especially on 6 nodes which represent 36 cores; it employed 115.21 hours to run three cycles.

Schmidt Number Equal to 0.70

For what concern this case the following figures show the results obtained.

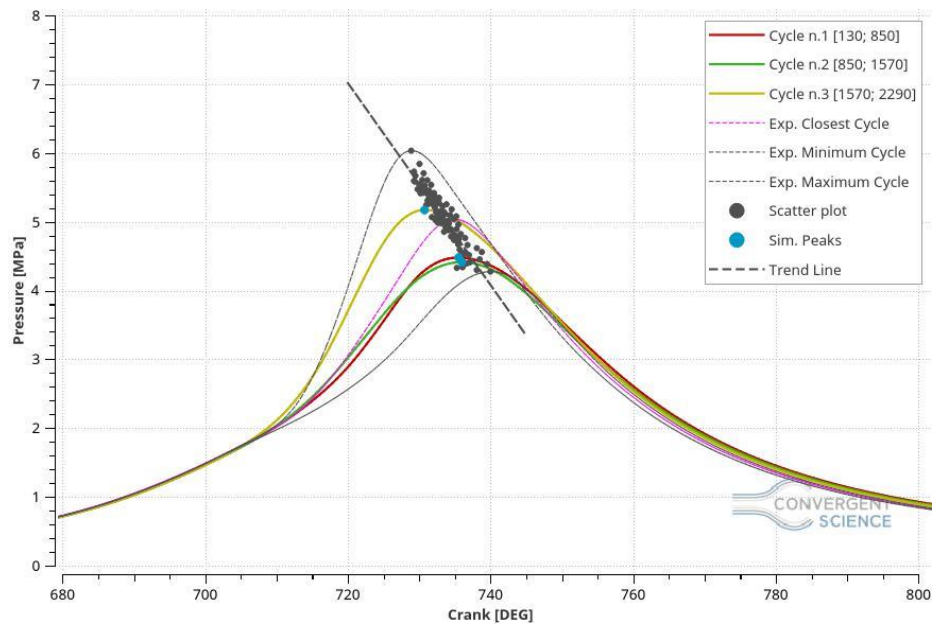


Figure 5.23: Pressure in Cylinder, Schmidt Number equal to 0.70.

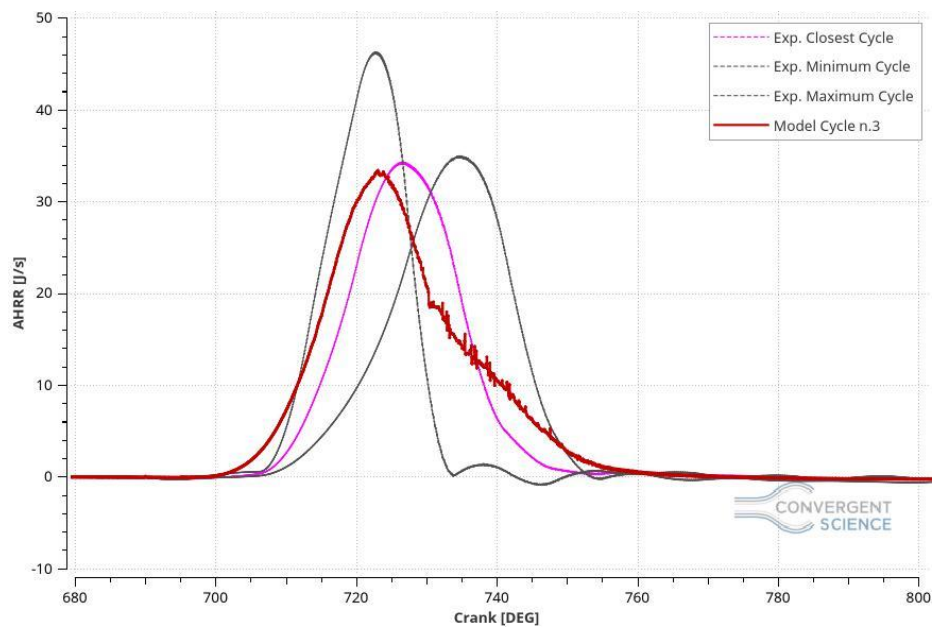


Figure 5.24: AHRR, Schmidt Number equal to 0.70.

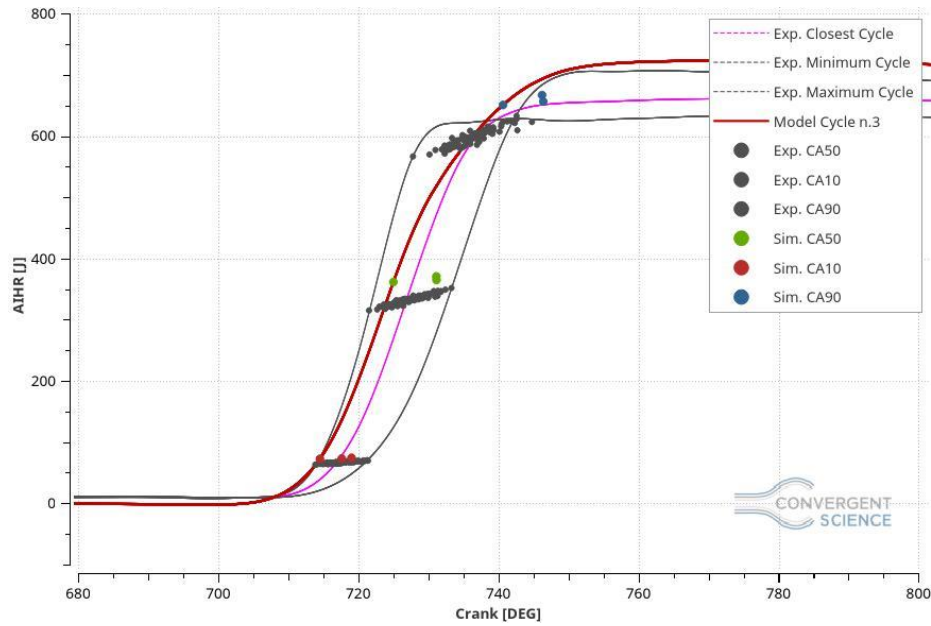


Figure 5.25: AIHR, Schmidt Number equal to 0.70.

The figure 5.23 shows the pressure in the cylinder of this particular case. The peak locations and the peak magnitude are acceptable also in this case because they are perfectly inside of the validity range even if the pressure peak value of the first two cycles is lower than the previous simulation. This behaviour can be associated to the cycle to cycle variability.

The trapped mass error, of this particular case, results to be 0.23%.

However, in the figure 5.24 and 5.25, the AHRR curve tail is still too high and that influences the burn duration achieving an error equal to 33.4%.

This simulation has been run on 6 nodes (36 cores) and it employed 117.67 hours to make three cycles.

Comparisons

In order comprehend which is the best improvement obtained, according to the Schmidt Number sensitivity, the figures 5.26, 5.27 and 5.28 will show the comparisons of the cases with Schmidt number equal to 0.78 (which is the reference simulation), 0.75 and 0.70 respectively.

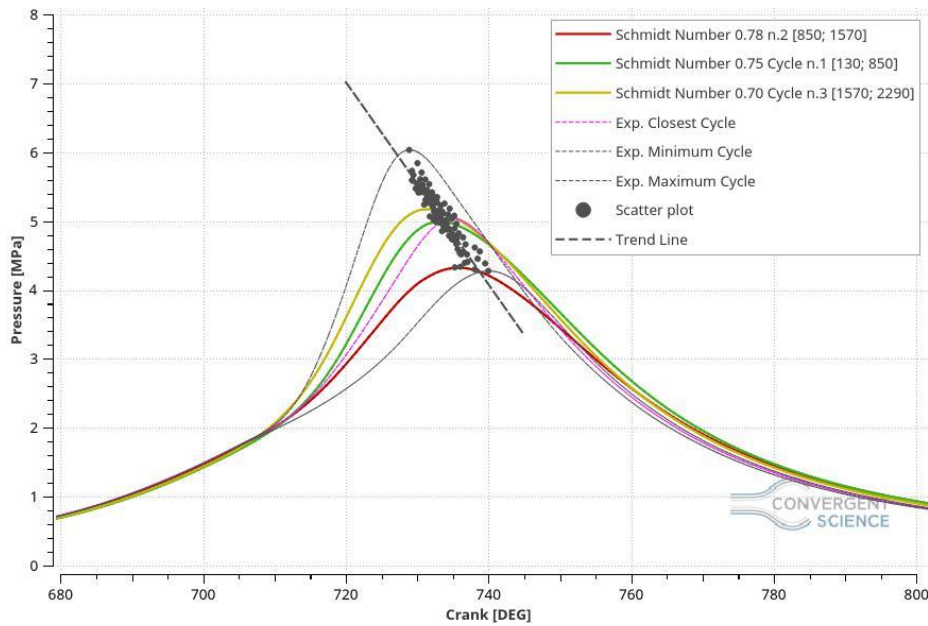


Figure 5.26: Schmidt Number Sensitivity, Pressure Comparison.

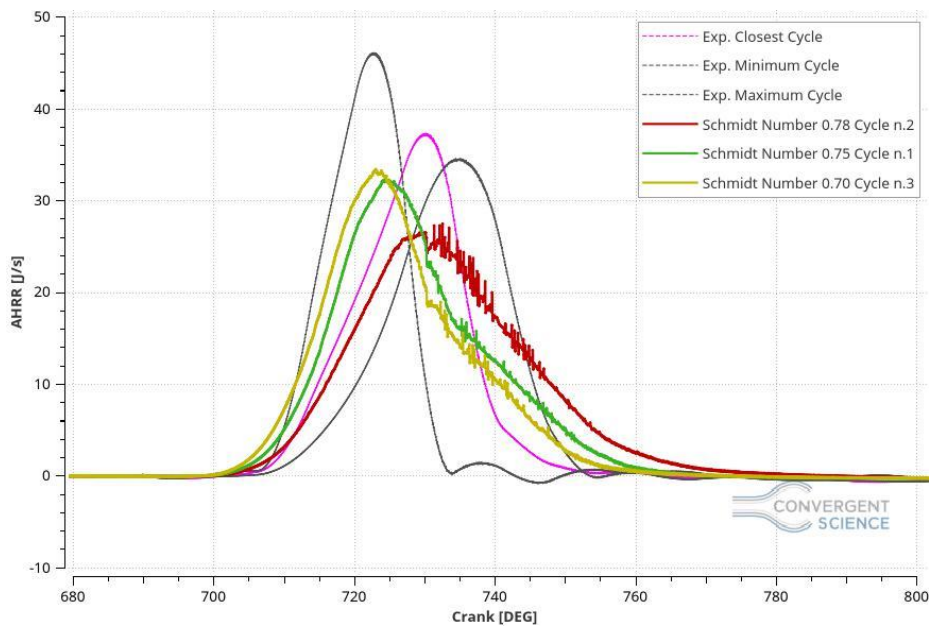


Figure 5.27: Schmidt Number Sensitivity, AHRR Comparison.

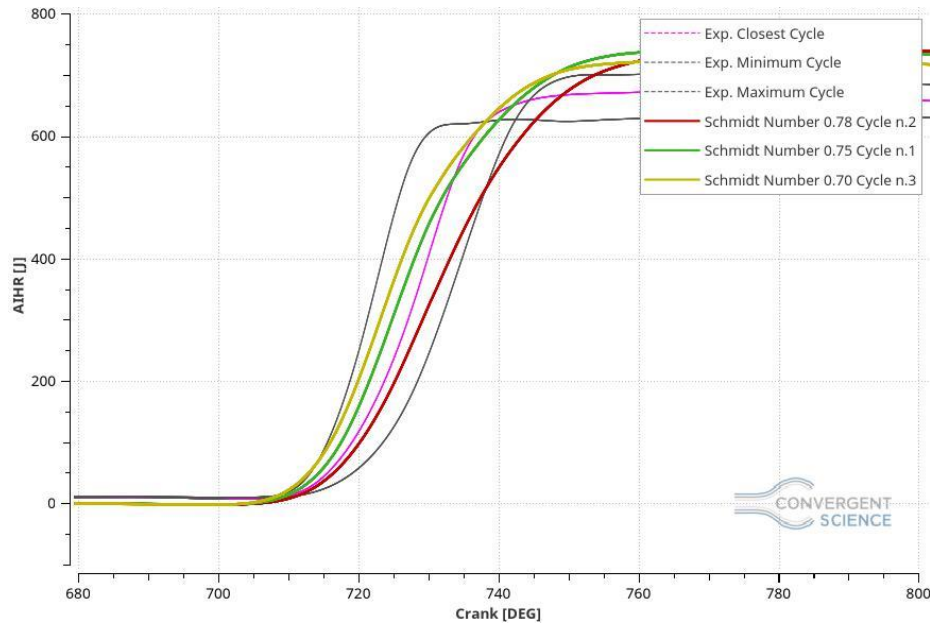


Figure 5.28: Schmidt Number Sensitivity. AIHR Comparison.

In the figure 5.26 the pressure improvement is shown, decreasing the Schmidt number, the mass diffusivity increases and, consequently, the combustion is faster and able to reach higher values of pressure in the chamber. At the same time, this modification helped to shift the peak location matching, quite perfectly, the experimental trend line.

An improvement can be seen also on the AHRR, figure 5.27, because the tail, decreasing the Schmidt Number, is going down. Unfortunately, the Schmidt Number alteration make the combustion too fast in the beginning (at 710 CAD), since that modification alters the mass diffusivity that is strongly linked with the combustion speed. According to this graph, the compromise is forced on the case with Schmidt Number equal to 0.75.

Conversely, on the AHIR comparison (figure 5.28), according with the burn duration showed above, the minimum error between those cases is the simulation with Schmidt number equal to 0.75 with a burn duration of 2.26% against 33.4% of the simulation with Schmidt Number equal to 0.70 and 36.3% of the simulation with Schmidt Number equal to 0.78, which represent the reference simulation where the pressure boundary conditions have been scaled.

According to this analysis, the best balance between a too fast combustion and the right peak location and value is the case with a Schmidt Number equal to 0.75, thus this simulation will be defined a reference simulation from where the others cases, that will be run, will be compared with.

5.2.5 Reaction Multiplier Sensitivity

In parallel with the Schmidt Number sensitivity, with the same aim to adjust the pressure peak locations and their magnitude, a SAGE reaction multiplier sensitivity has been run. The SAGE Reaction Multiplier is a useful parameter able to increase or decrease the combustion speed, specifically the chemical reaction rate. Normally, this value is equal to 1 but for this particular case, since the aim is to rise up the too low-pressure peaks, it has been increased of 5% and 10%, which means that the combustion chemical reactions will be faster of a coefficient equal to 1.05 and 1.1 respectively.

SAGE Reaction Multiplier Equal to 1.05

For what concerns the simulation with a reaction multiplier equal to 1.05, the results are showed in the figures 5.29, 5.30 and 5.31.

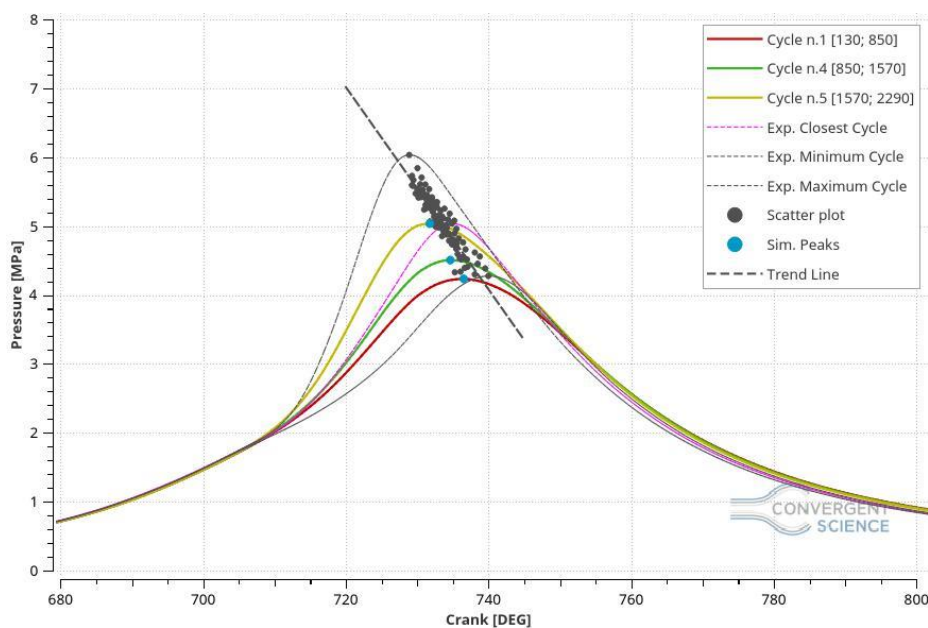


Figure 5.29: Pressure in Cylinder, Reaction Multiplier equal to 1.05.

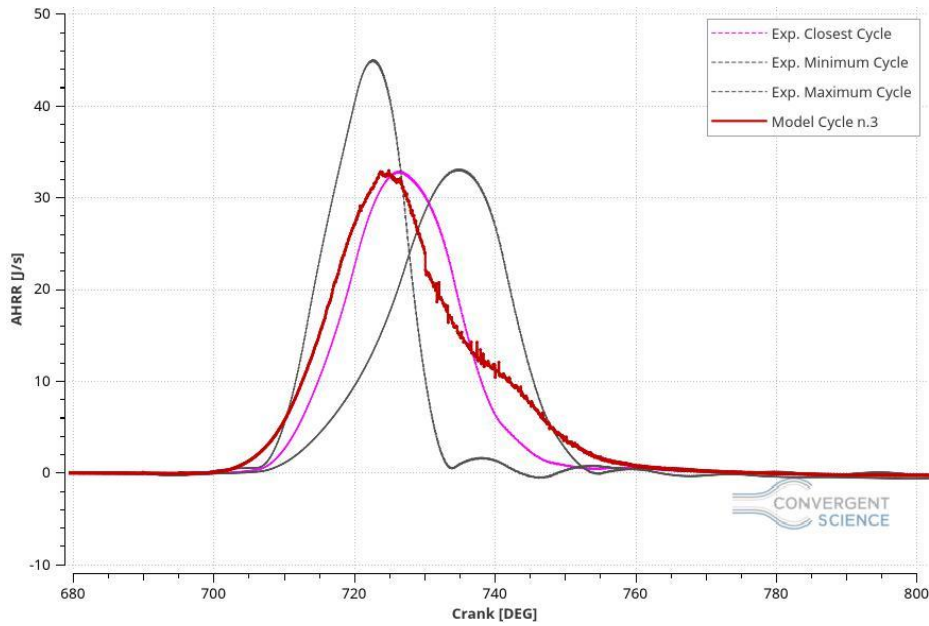


Figure 5.30: AHRR, Reaction Multiplier equal to 1.05.

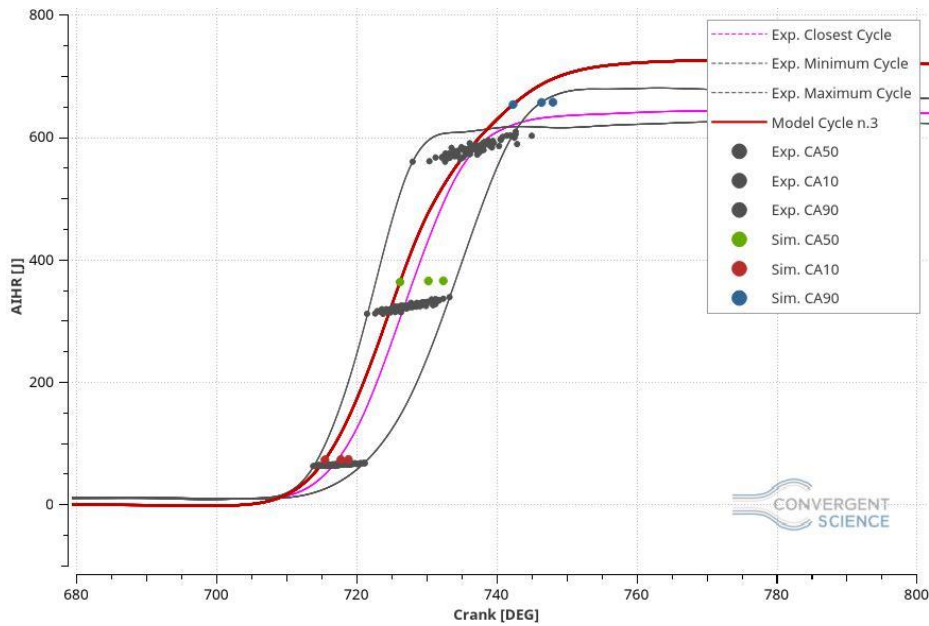


Figure 5.31: AIHR, Reaction Multiplier equal to 1.05.

Also in this case, an improvement on the peak locations and values can be noticed. In the figure 5.29 the pressure magnitude is visibly increased but the peak locations are not following completely the trend line, thus some other modification should be done. For what matters the AHRR and AIHR, present in the figures 5.30 and 5.31, the improvements, in comparison with the Schmidt number sensitivity cases, are less remarkable especially on the AIHR plot. In the AHRR chart the combustion is too fast in the beginning and the plot tail is too high at the end of the combustion phase, even if the heat release rate peak seems to be acceptable. Another problem on the AIHR is the total energy produced by the combustion phase, in fact it is considerably higher than the measurements.

The trapped mass error referred to this particular case is 0.23% and the burn duration error, influenced by the long combustion due to the high AHRR tail, is 47.55% longer than the measurements.

This simulation has been run on a special cluster with the features to have 20 cores per node, in particular this case has been computed by 3 nodes (60 cores) in 42.94 hours.

SAGE Reaction Multiplier Equal to 1.1

For what matters this case the following figures will show the results obtained.

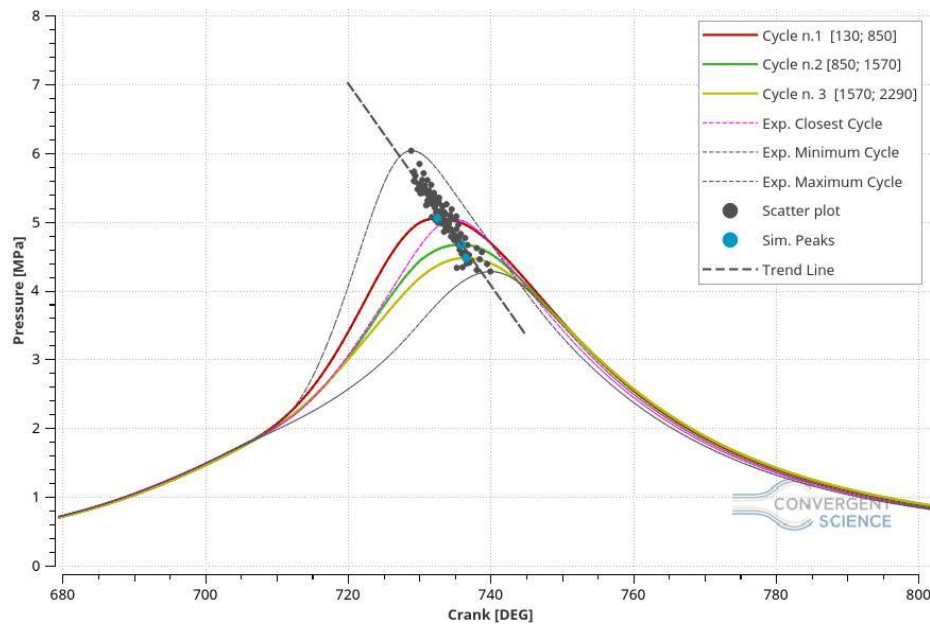


Figure 5.32: Pressure in Cylinder, Reaction Multiplier equal to 1.1.

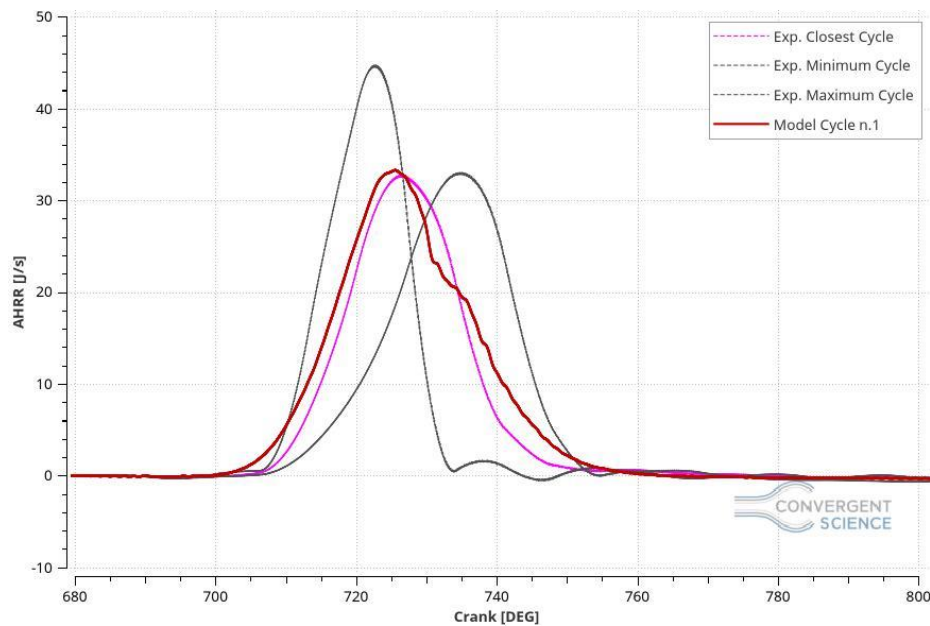


Figure 5.33: AHRR, Reaction Multiplier equal to 1.1.

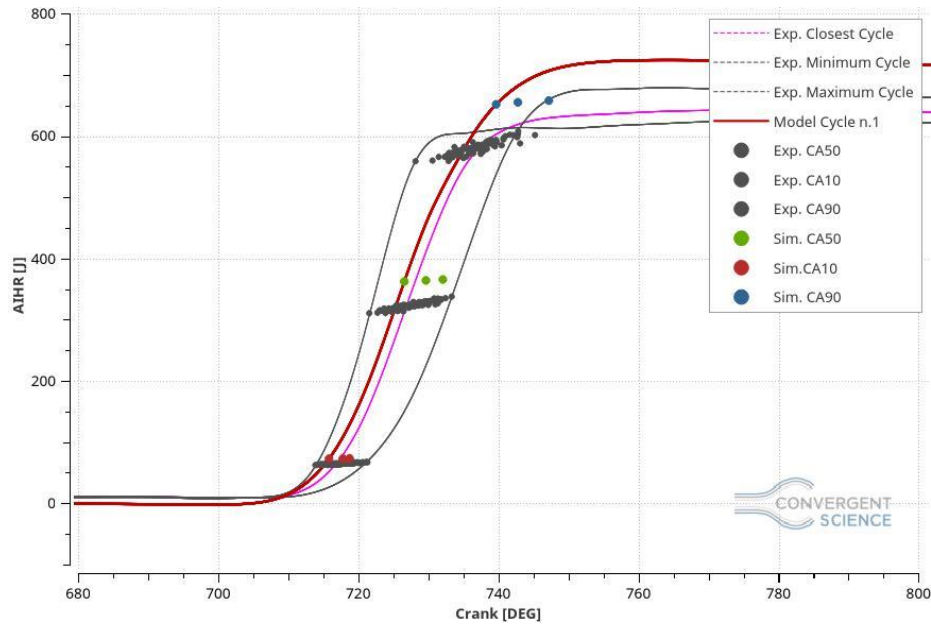


Figure 5.34: AIHR, Reaction Multiplier equal to 1.1.

The figure 5.32 shows the pressure in the cylinder where the perfect peak locations is easy to notice, in fact the pressure peaks stand perfectly on the trend line and they also are inside of the validity range made by the cycle to cycle variability.

The AHRR, figure 5.33, shows that the reaction multiplier modification affects the combustion behaviour decreasing the plot tail, even if the combustion remains too fast in the beginning. Unfortunately, this improvement is not enough to be considered acceptable because the burn duration error is still too high (28.69%), although a significant improvement has been noticed. The most relevant problem that can be noticed from the AIHR plot is the quantity of energy present in the system. This energy is significantly higher than the experimental data maximum cycle, which means that the model is not predictive yet and many improvements have to be done.

The trapped mass error is 1.99% thus it is acceptable.

This simulation has been run on the 6 cores machines, precisely on 6 nodes (36 cores) and it employed 119.43 hours to compute three cycles.

Comparisons

This comparison has been attempted to see the differences produced by the SAGE Reaction Multiplier sensitivity. The figures will show the results of the cases with the reaction multiplier coefficient equal to 1.0, 1.05 and 1.1 respectively.

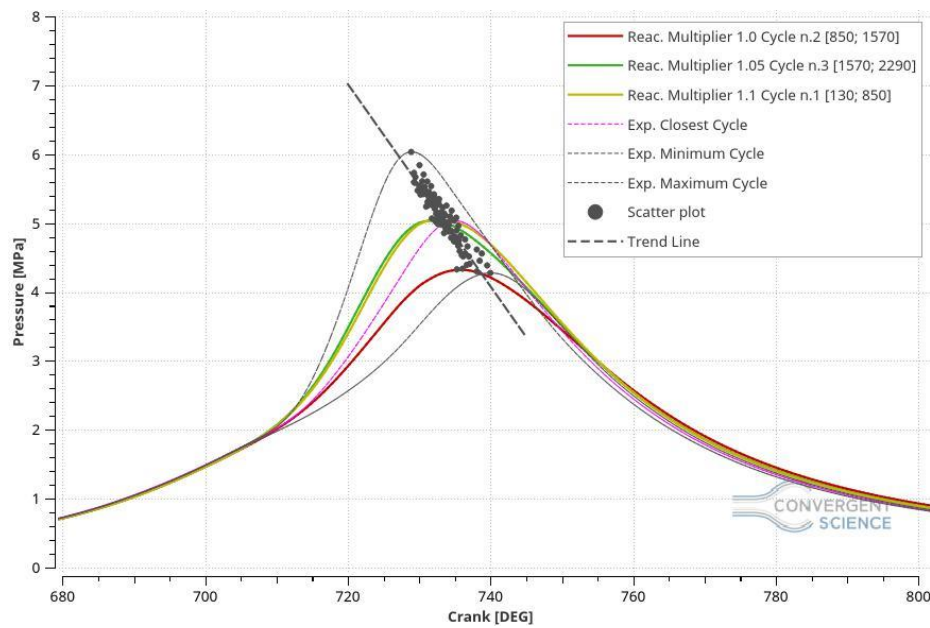


Figure 5.35: SAGE Reaction Multiplier Sensitivity, Pressure Comparison.

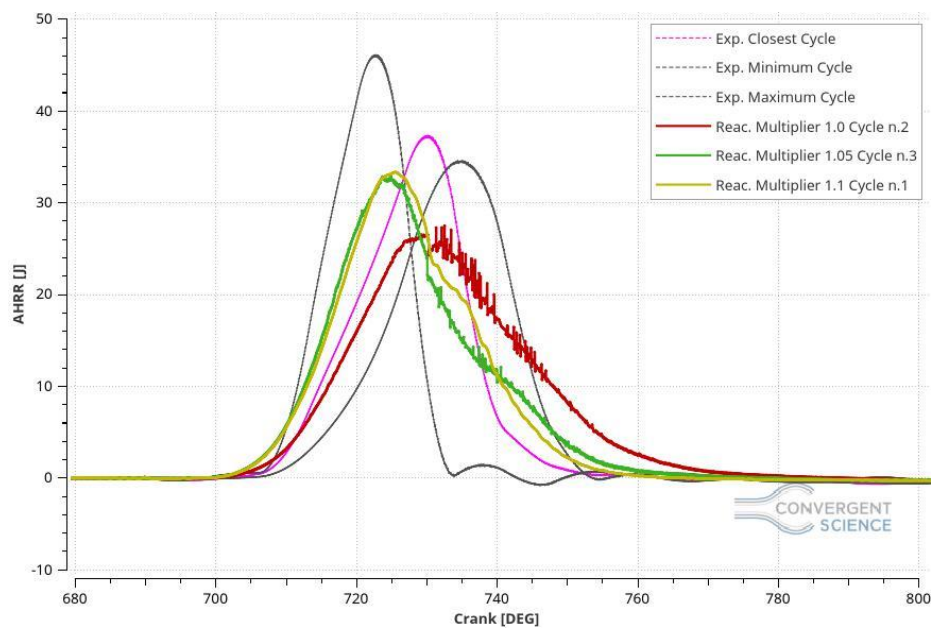


Figure 5.36: SAGE Reaction Multiplier Sensitivity, AHRR Comparison.

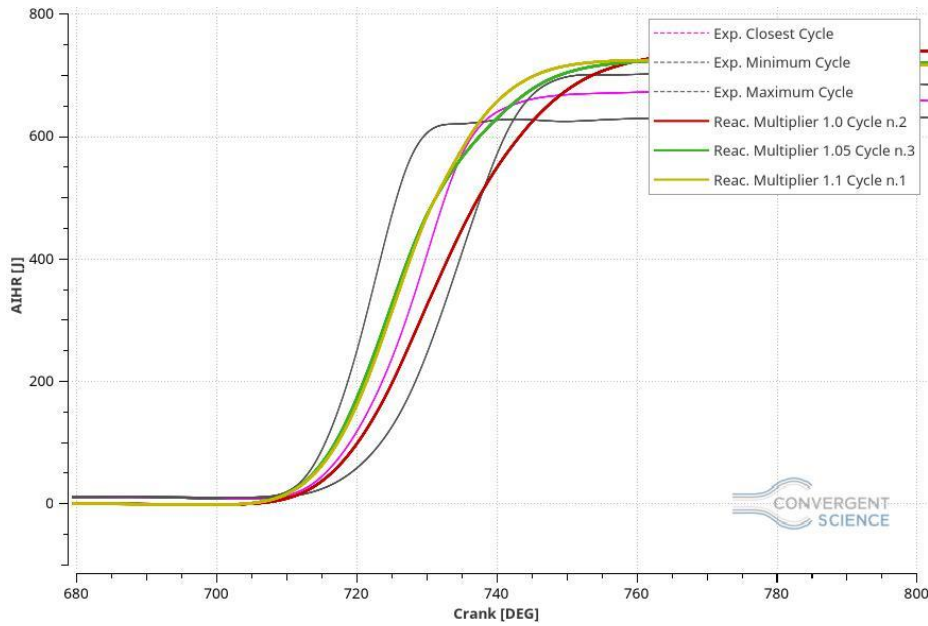


Figure 5.37: SAGE Reaction Multiplier Sensitivity, AIHR Comparison.

On the pressure plot (figure 5.35) the pressure magnitude improvement is noteworthy, in particular, increasing the combustion rate, due to the rise of the reaction multiplier factor, the pressure tends to go up rapidly. Focusing on the pressure peak locations, a correlation between the peak location and the reaction multiplier value is present with the same impact of the Schmidt number value, by means a shift of the peak location closer to the trend line made by the 100 peak cycles.

For what concerns the AHRR plot, figure 5.36, the reaction multiplier increase, shifts the curve giving the sensation to improvement but, unfortunately, the tail is still too high and the combustion begin too fast making all these results unacceptable.

Moreover, in the AIHR plot, figure 5.37, in all of the cases, the total energy presents in the chamber is higher than the experimental data and consequently, as it has been shown above, the model burn duration is substantially longer than the measurements. In particular, considering the cases with reaction multiplier 1.0 (which is the reference one), 1.05 and 1.1, the burn duration errors are 36.3%, 47.55% and 28.69% respectively.

5.2.6 LHV Correction

After several tests and simulations, in order to reduce the AHRR tail and the total energy in the combustion chamber, the final solution has been found and it is characterised by the using of a different low heat value (LHV) of the fuel composition. Since the fuel composition is not real but just an approximation, previously, the LHV computed by CONVERGE was equal to 50,12 MJ/kg. This value makes the combustion too powerful, compared to the measurements, and, consequently, the energy in the chamber and the burn duration was too high and long respectively.

Searching in literature, a new LHV value, equal to 47.141 MJ/kg, referred to a real natural gas fuel composition has been found. Since this value is referred to a real natural gas fuel composition, it should be more correct and it should give some advantages regarding the total energy calculation and on the burn duration.

In particular this simulation has been run with a Schmidt Number equal to 0.75, in order to fix the previous issues referred to the pressure peak location and magnitude, and with the new LHV to solve the quantity of energy and the burn duration problems.

The LHV correction is a way to force the LHV value to a simulation, avoiding its calculation by the software and setting the new value externally as an input parameter. In this way COVERGE will not compute the LHV regarded to the current fuel composition but it will use the input value as the real one. Usually this type of correction is useful when the correct fuel composition is unknown or when it is an approximation of the real one, as this particular case.

The figures 5.38, 5.39 and 5.40 will show the results referred to this specific case.

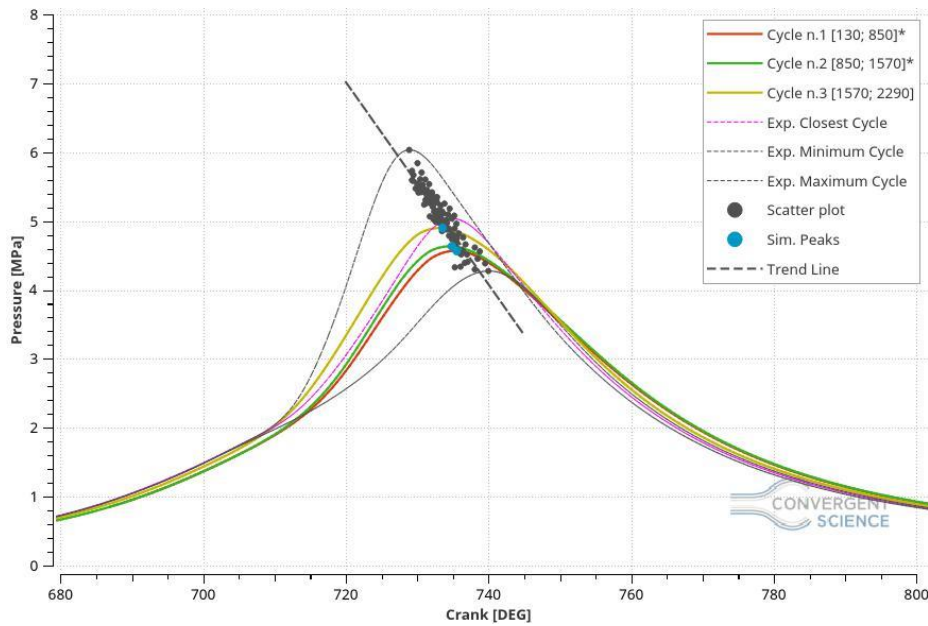


Figure 5.38: Pressure in Cylinder, LHV Correction.

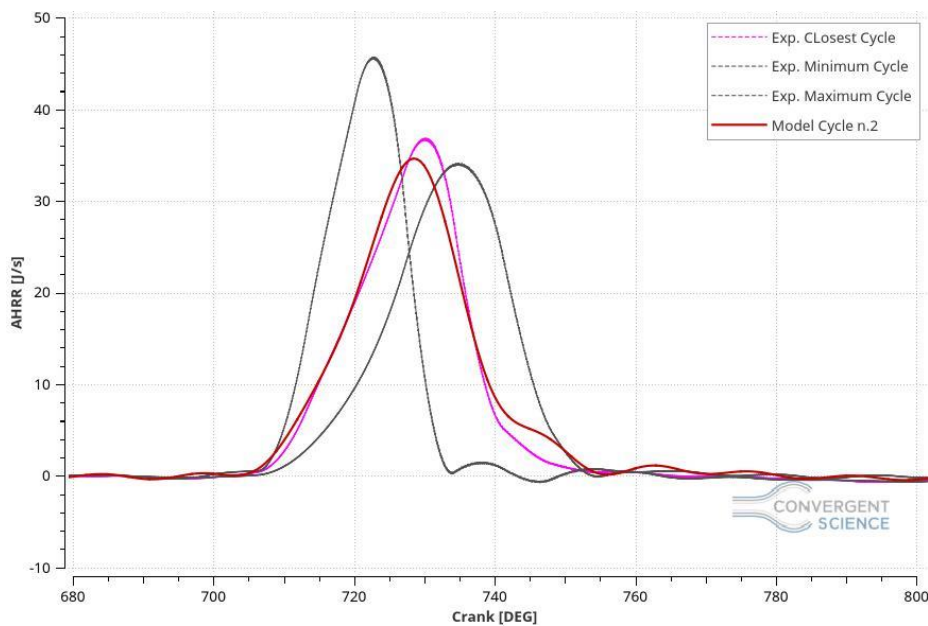


Figure 5.39: AHRR, LHV Correction.

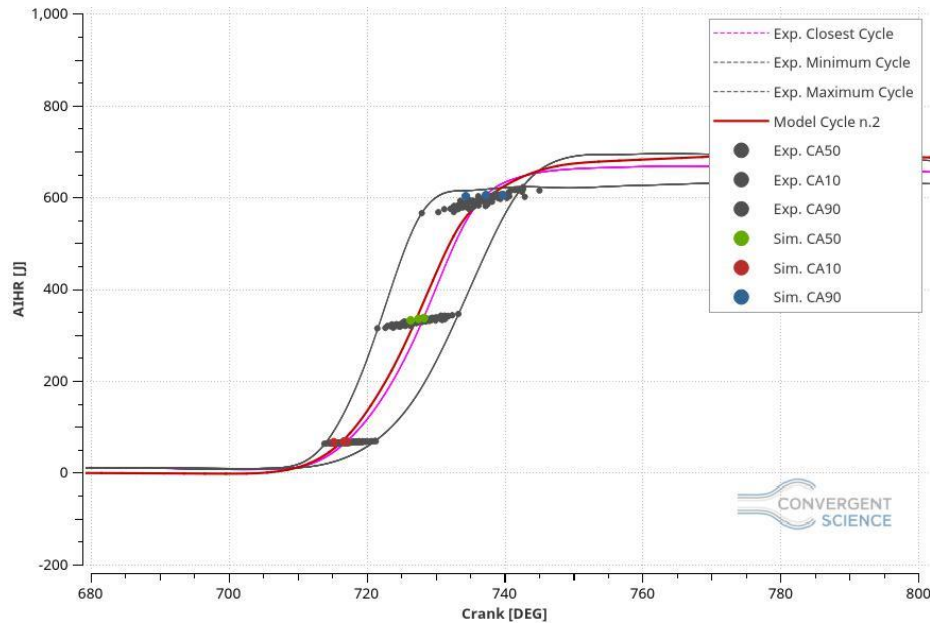


Figure 5.40: AIHR, LHV Correction.

In the figure 5.38, as expected, the pressure peak locations and magnitude are perfectly inside the validity range made by the CCV and the trend line regression, thanks to the Schmidt Number variation as showed in the previous case. The trapped mass error carried out from this case is 1.34% which can be considered acceptable.

For what concerns the AHRR, figure 5.39, the curve is almost matching the experimental reference cycle (closest cycle to the ensemble average) in the beginning of the combustion because, since the total energy is lower, the combustion is slower than the previous cases and, at the same time, obtaining a lower AHRR tail, getting closer to the reference cycle.

Moreover, focusing on the AIHR curve, figure 5.40, the total energy and the crank angles corresponded to the 10%, 50% and 90% of burned mass are matching with the experimental data giving a burn duration error equal to 1.635%. The trapped mass error of this simulation results to be equal to 0.265%.

This simulation has been run on 6 cores machines, especially on 6 nodes with correspond on 36 cores and it employed 118.92 hours to complete a three cycles simulation.

From the analysis made, according to the variables used to compare the simulations with the measurements and the results obtained, the model can predict, with reasonable errors, the engine behaviour for this operating point, which means that the model can be considered a good agreement.

5.3 Operating Point 4600x7.9x1 (NG+15% H_2)

For what matters the operating point 4600[rpm]x7.9[bar]x1[lambda] with the addition of 15% in volume of hydrogen, the results will be shown in the following pages in details focusing on the modifications made on the standard case set-up. In this particular case, different reaction mechanism has been used to find the most predictive one and finally obtain the model validation. The fuel composition of this specific case is:

- $CH_4 = 83.3\%$
- $C_2H_6 = 0.85\%$
- $CO_2 = 0.85\%$
- $H_2 = 15\%$

5.3.1 Base Simulation

In this specific simulation, according to the reference case set-up, the GRI III mechanism has been used and the figures 5.41, 5.42, 5.43 and 5.44 show the results obtained.

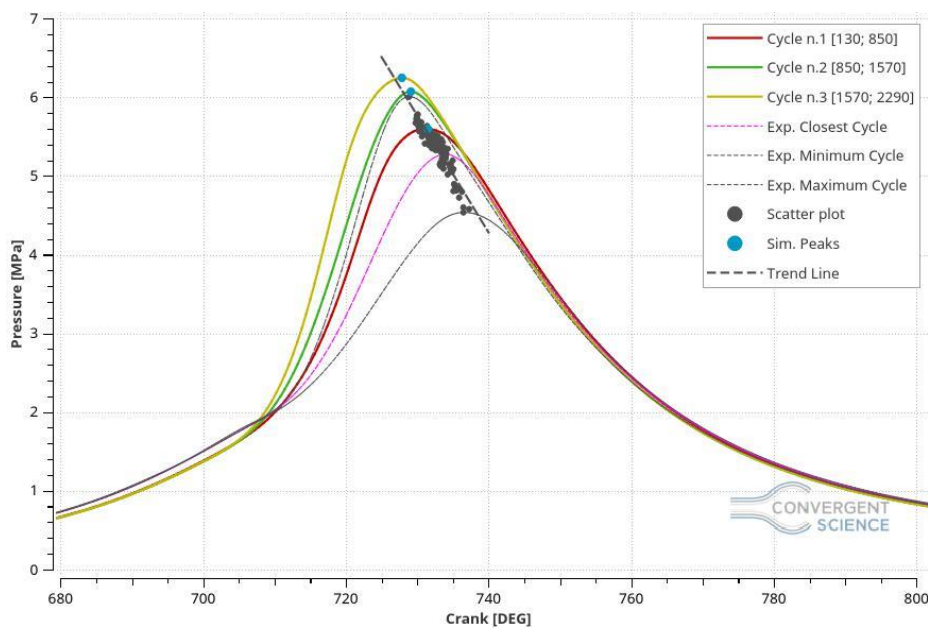


Figure 5.41: Pressure in Cylinder, Base Simulation.

From the figure 5.41 different problems has been found:

- Pressure peak magnitude overestimated;
- The compression phase does not match the experimental data.

These issues can be solved easily by changing the reaction mechanism and increasing the pressure boundary condition in the inlet. The peak locations are already following the trend line made by the 100 experimental cycles, thus modifications are not necessary.

Making a zoom on the compression phase (figure 5.42) the compression error between the model and the measurements is easier to catch, in particular the error is equal to 9.58%, at spark advance (697 CAD) which is not acceptable and some modifications need to be performed.

Furthermore, the trapped mass error computed, referred to this particular case, is equal to 5.6% which cannot be considered reasonable.

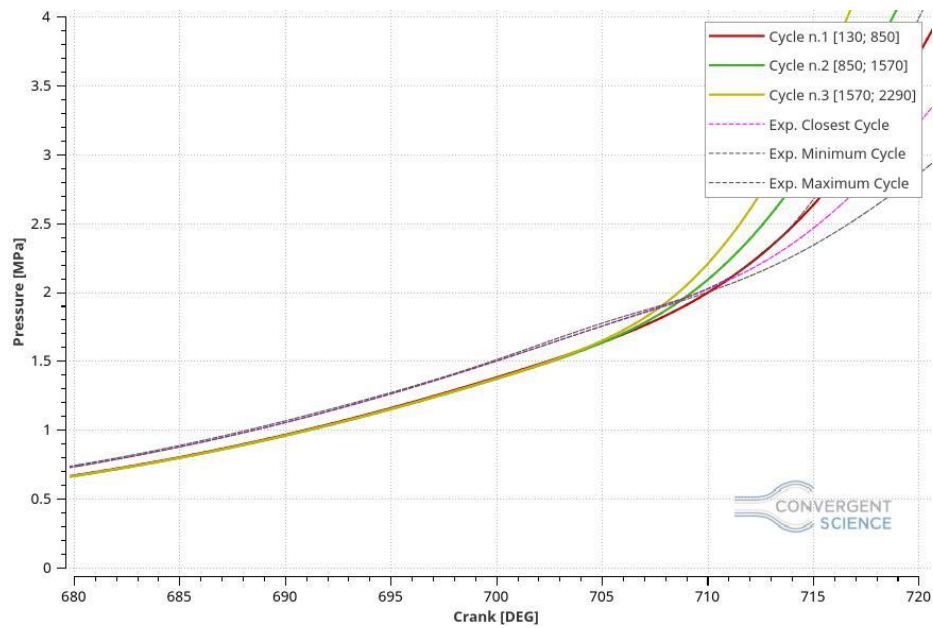


Figure 5.42: Compression Phase zoom, Base Simulation.

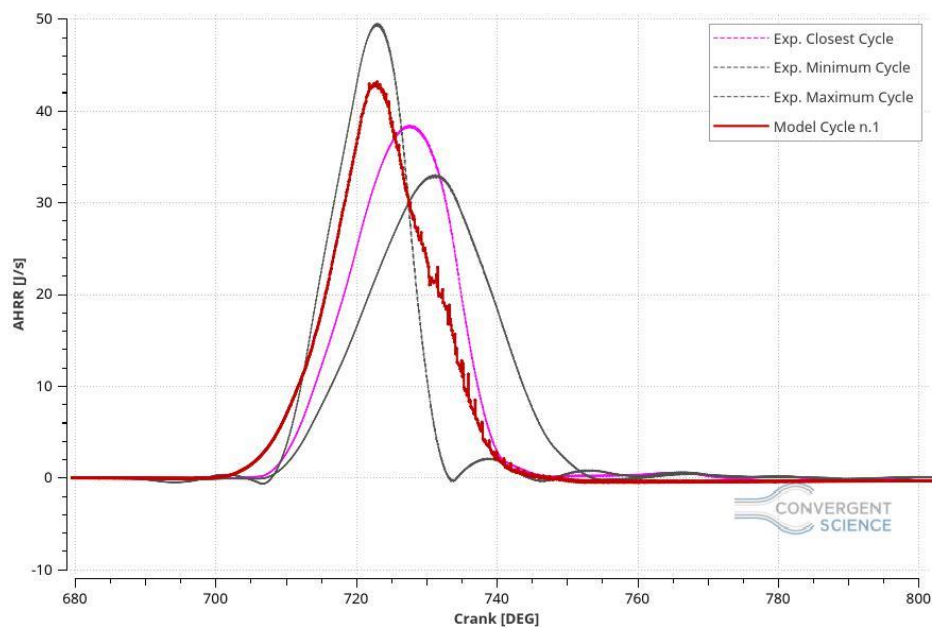


Figure 5.43: AHRR, Base Simulation.

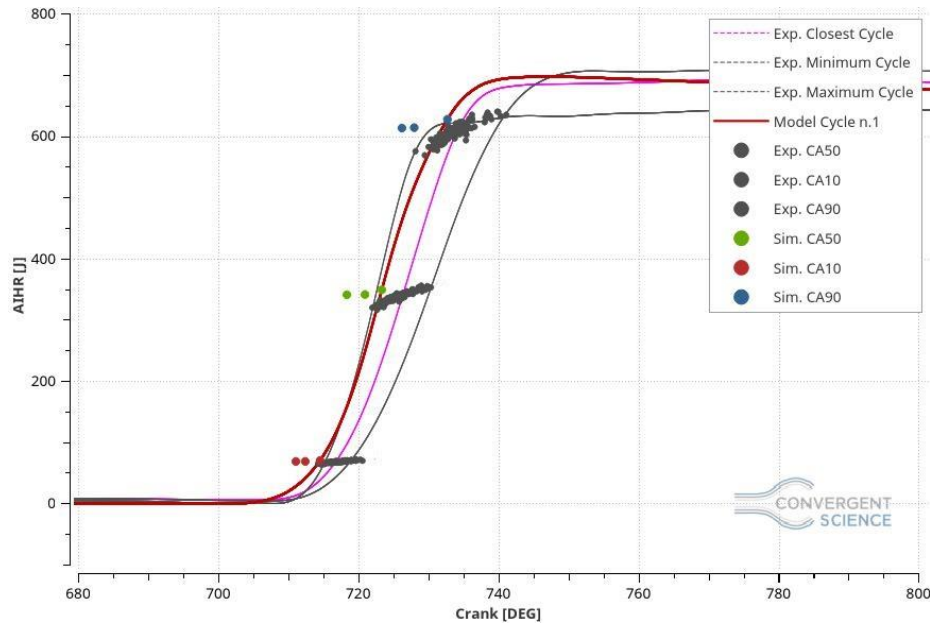


Figure 5.44: AIHR, Base Simulation.

Focusing on the AHRR, figure 5.43, the combustion shown is faster than the reference cycle (closest cycle to the ensemble average) and in the very beginning, almost at SA crank angle, the combustion results too fast even than the measured maximum cycle. Since the combustion is quicker than the experimental data, the AIHR, shown in the figure 5.44, displays that the burning duration error is equal to 4.13% shorter than the measurement. Which means that the combustion is faster and it employ less crank angles to reach completion than the previous cases. Moreover, the total energy in the chamber can be considered acceptable because it is equal to the closest cycle energy and more modifications of it are not necessary. The fundamental issue is that the first cycle considered, might be assumed acceptable in terms of quantity con energy, peak location and magnitude, but the other cycles are overestimating the data making this case not adequate.

This simulation has been run on the special cluster on 3 nodes, which correspond to 60 cores, and it employed 54.64 hours to reach completion.

5.3.2 New Reaction Mechanism: USC Mech

In order to fix the pressure peak magnitude issue, the USC reaction mechanism has been introduced. The aim is to considerably reduce the pressure peak in order to get inside to the validity range made by the CCV of this specific engine. Since in a previous thesis work this reaction mechanism gave back underestimate results in term of laminar flame speed and ignition delay, it has been decided to use it to reduce the combustion burn rate and, consequently, reduce the pressure peaks significantly. In the figures 5.45, 5.46 and 5.47 the results obtained will be shown and a brief description will take place.

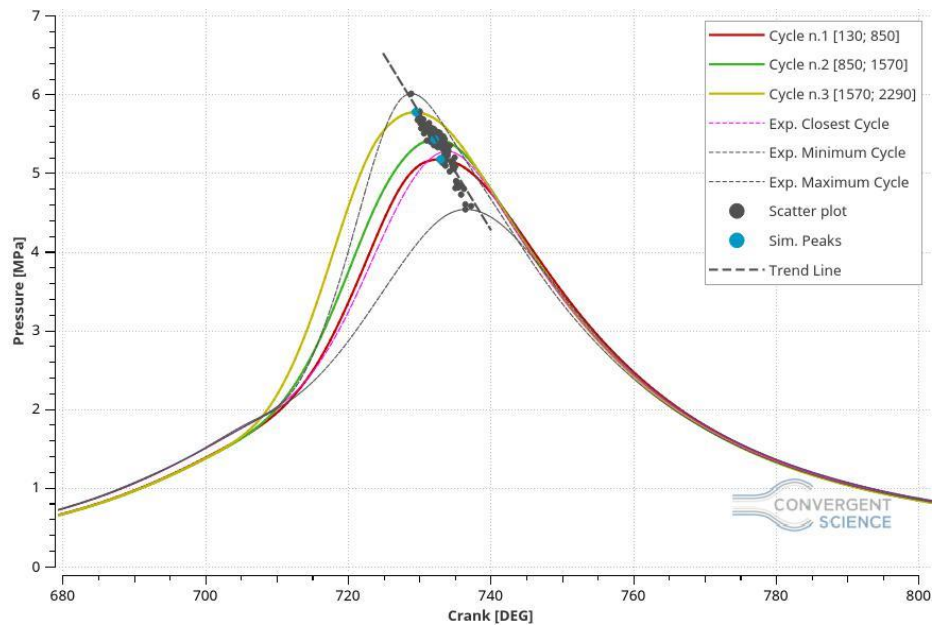


Figure 5.45: Pressure in Cylinder, USC Mechanism.

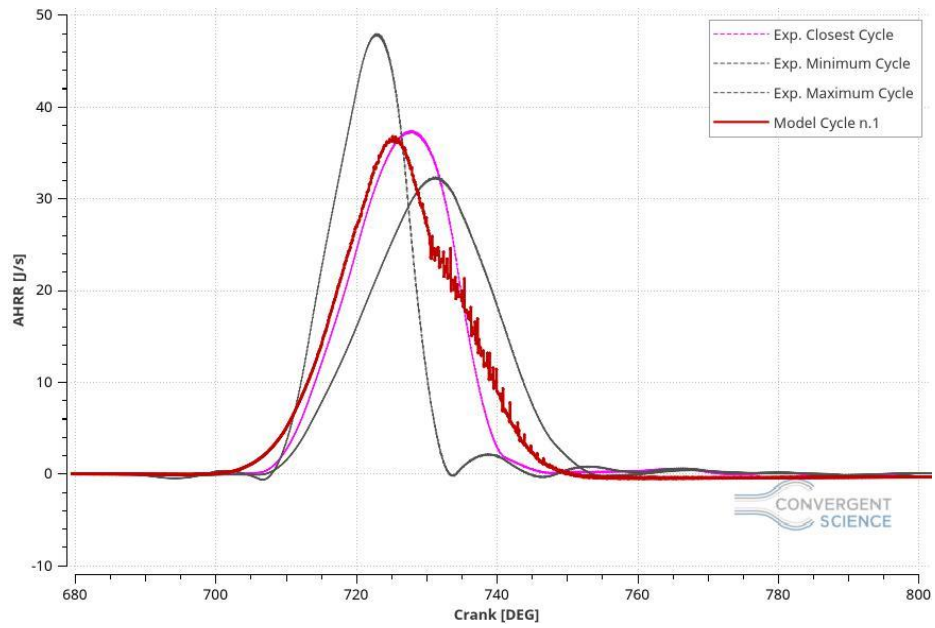


Figure 5.46: AHRR, USC Mechanism.

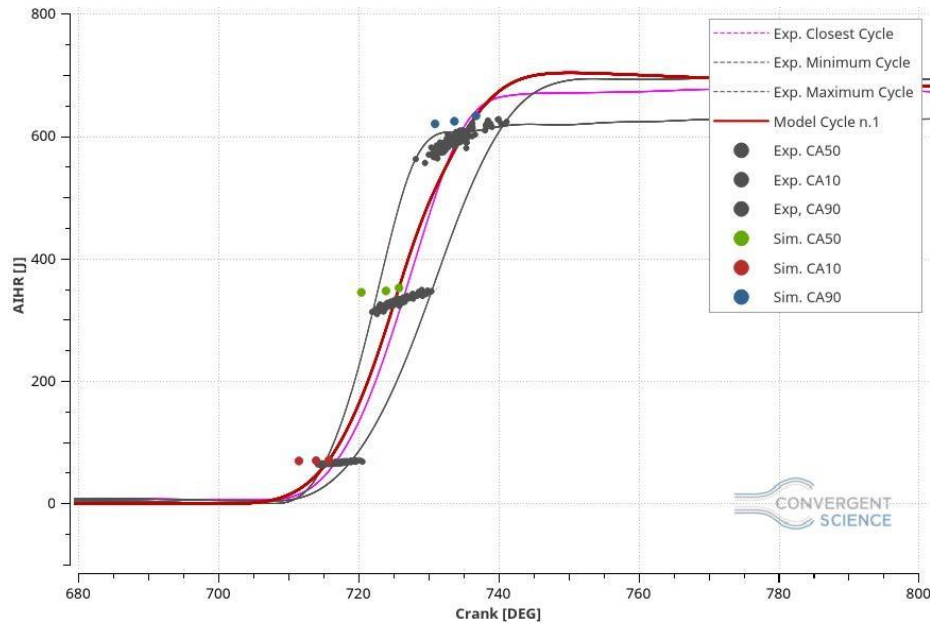


Figure 5.47: AIHR, USC Mechanism.

As the figure 5.45 shows, the USC mechanism give a lower pressure peaks even if they are still overestimating the experimental closest cycle, but an improvement is noteworthy. The pressure peak locations are perfectly following the trend line which means that, regarding that variable, no additional modifications are needed and they can be considered reasonable. The trapped mass error, referred to this particular simulation, is still high and it is equal to 5.49% which cannot be considered acceptable.

Focusing on the AHRR and the AIHR, figure 5.46 and 5.47, the model cycle considered as reference is the number one and the relative combustion generated is too fast in the beginning and quite long at the end influencing negatively the AIHR and giving a burn duration error equal to 17.47% longer than the measurements. Additionally, it is easy to notice that the energy in the chamber is higher than the previous case but still acceptable.

This simulation has been run on the 6 cores machines, especially on 6 nodes, which represent 36 cores, and it employed 117.83 hour to run a three cycles simulation.

5.3.3 Boundary Conditions Manipulation

In order to match the experimental data during the compression phase, it has been decided to increase the pressure boundary conditions in the inlet of a value equal to the error found at SA in the base simulation, which means that the boundary conditions have been increased of 9.58%. To be sure that the trapped mass would be conserved, also the Inflow temperature boundary condition has been increased of the same value, obtaining 345.125K. As previously mentioned, this approximation can be considered acceptable because the pressure boundary conditions were not directly measured by means sensors located in the intake system, but they were computed by a MatLab script.

The USC mechanism has been used to decrease the pressure peak magnitude as the previous case.

The figures 5.48, 5.49 and 5.50 show the results of this specific case.

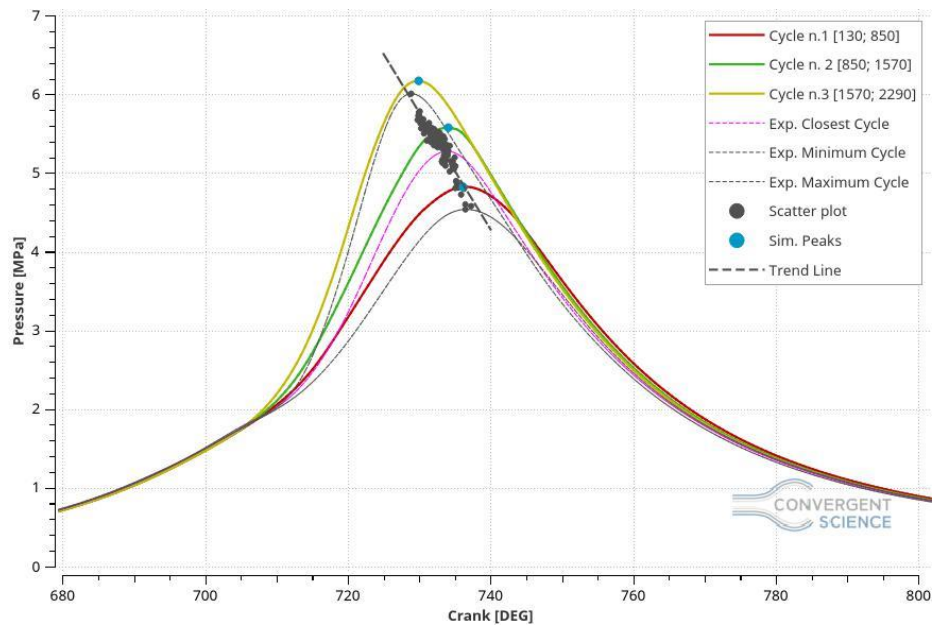


Figure 5.48: Pressure in Cylinder, Boundary Conditions Manipulation.

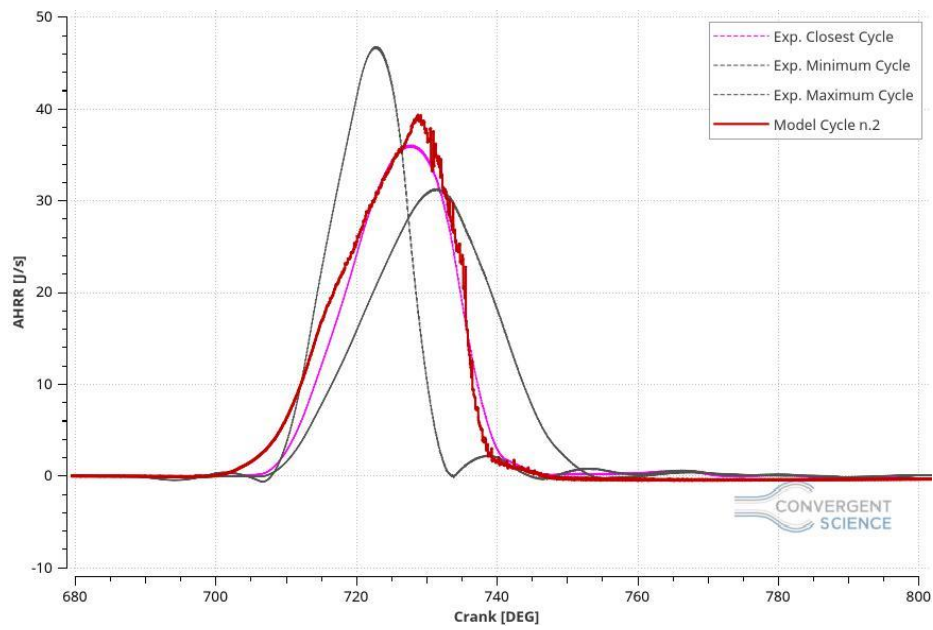


Figure 5.49: AHRR, Boundary Conditions Manipulation.

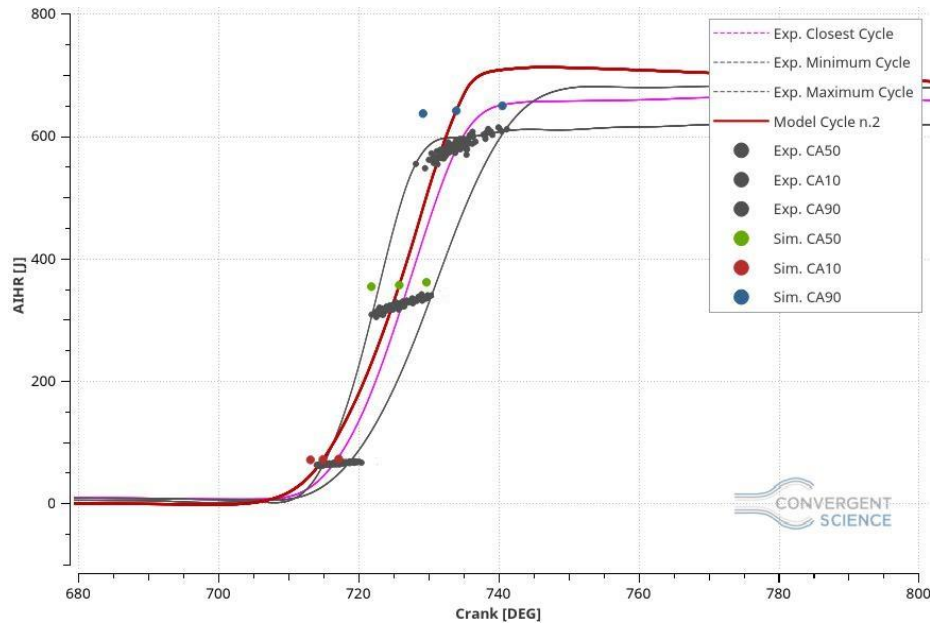


Figure 5.50: AIHR, Boundary Condition Manipulation.

The figure 5.48 shows the pressure in the cylinder and noteworthy is the fact that, during the compression phase, the model and the experimental data are matching perfectly. Unfortunately, the increasing of the pressure boundary conditions influenced the peak pressure generating higher peaks with a too high tail which effects undesirably all the others plots obtaining too much energy in the chamber even if the trapped mass error is -3.27%, which means that the mass in the chamber, after the intake valve closing (IVO), is 3.27% lower than the measurements.

Focusing on the AHRR and AIHR, figures 5.49 and 5.50 respectively, and considering the simulated second cycle as the reference one, since it is the closest one to the ensemble average, it easy to see that the combustion starts too early, but it follows the closest cycle to the ensemble average on the final part of the phase. The underlying area of the model is bigger than the ensemble, which means that the integration of the AHRR curve itself will give a too high energy in the chamber that cannot be considered acceptable. Computing the burn rate as the difference between CA90 and CA10, in terms of crank angles, the error between the model and the experimental data results to be 6.3% obtaining an improvement.

This simulation has been run con the 6 cores machines on 6 nodes, which means 36 cores and it run for 117.78 hours to reach completion.

5.3.4 LHV Sensitivity

Considering that some uncertainties on the correct fuel composition can be easily found and since the total energy in the chamber and the burn rate obtained in the previous cases are too high and too fast respectively, a lower heat value (LHV) correction sensitivity has been carried out. Several LHV ranges have been found in literature, with the referred physical conditions, of NG fuel and hydrogen in order to make the LHV validity range calculation possible. Since the fuel composition used can be also written:

- NG = 85%
- H₂ = 15%

Instead of:

- $\text{CH}_4 = 83.3\%$
- $\text{C}_2\text{H}_6 = 0.85\%$
- $\text{CO}_2 = 0.85\%$
- $\text{H}_2 = 15\%$

The potential LHV range to use it easily computable by means of a weighted average based on the species mass fraction of NG and hydrogen.

The ranges funded in literature are the followings:

- *LHV NG range: 42/55 MJ/kg*
- *LHV H2 range: 120/142 MJ/kg*

And computing the below formula (equation 5.2) replacing the minimum and the maximum values, the potential LHV range obtained is 53.7/68.05 MJ/kg.

$$LHV_{NG+H_2} = \frac{LHV_{NG} \cdot 85 + LHV_{H_2} \cdot 15}{85 + 15} \quad (5.2)$$

Since the current fuel LHV computed by CONVERGE is equal to 59.12 MJ/kg, three different simulations have been run with three different LHV: 54, 55, 56 MJ/kg.

With this correction a reduction of the pressure and AHRR tail is expected obtaining acceptable results.

LHV Equal to 54 MJ/kg

The figures 5.51, 5.52 and 5.53 show the results obtained for this particular case.

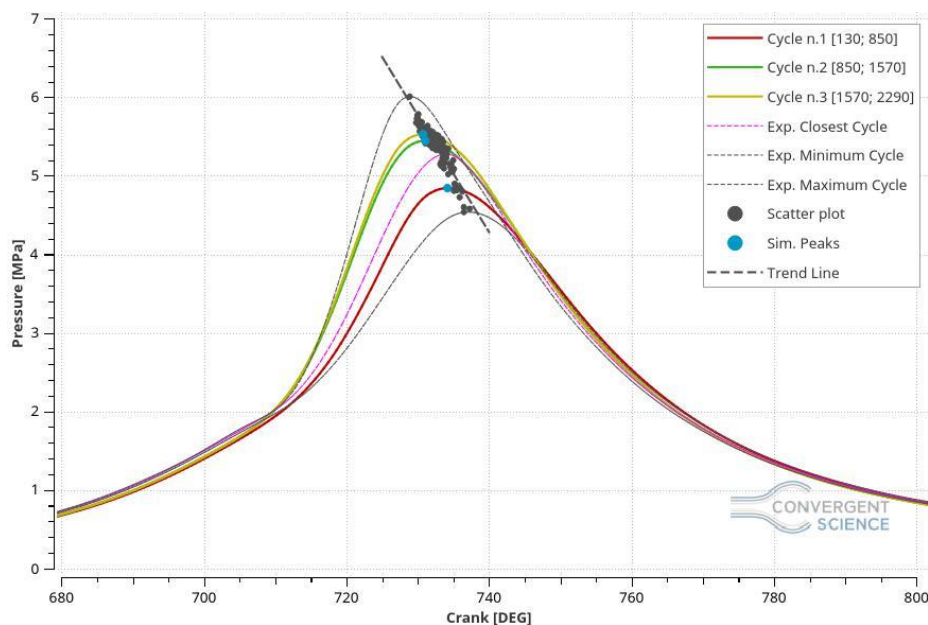


Figure 5.51: Pressure in Cylinder, LHV equal to 54 MJ/kg.

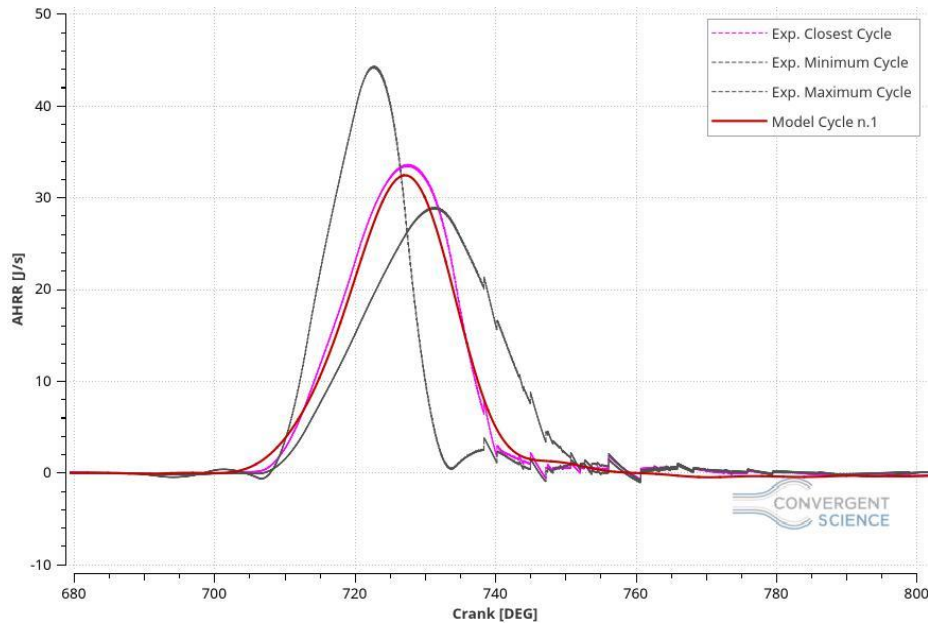


Figure 5.52: AHRR, LHV equal to 54 MJ/kg.

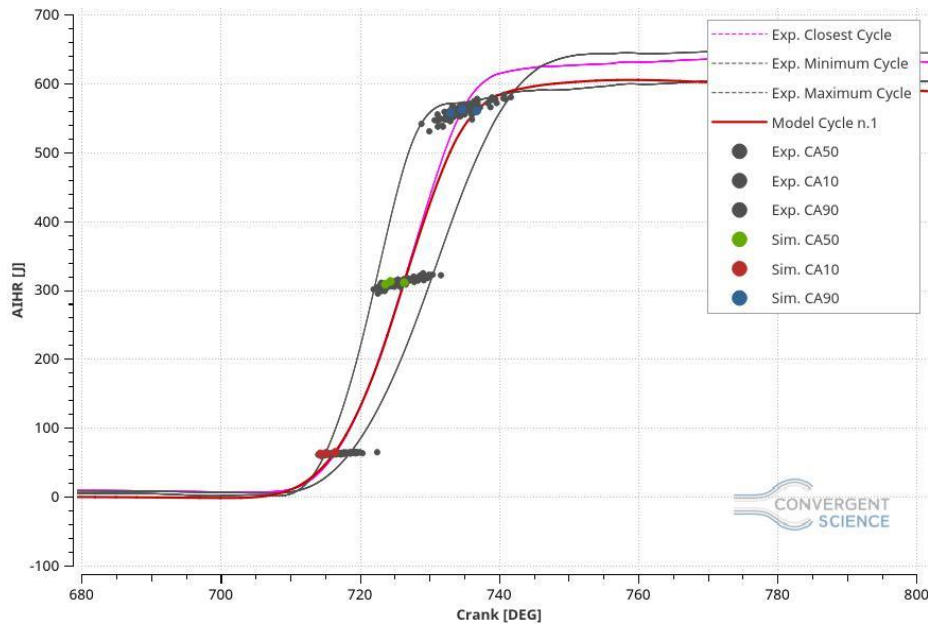


Figure 5.53: AIHR, LHV equal to 54 MJ/kg.

Looking at the pressure curve, figure 5.51, considerably improvements can be easily seen on the tail and on the pressure magnitudes, indeed, the pressure peaks stand inside the CCV validity range and the pressure peak locations are following the trend line obtaining significant progresses. For what concerns the pressure curve tail, a remarkable improvement has been obtained reducing the tail itself until the match with the experimental data. This progress is fundamental because it influences positively the AHRR and AIHR plots turning this case into a good agreement. The trapped mass error obtained in this particular case is equal to 0.16% which can be considered acceptable.

Focusing on the AHRR and AIHR curves, figures 5.52 and 5.53 respectively, it possible to see, for what concerns the former, that the simulated AHRR follows almost perfectly the reference experimental cycle, in the very beginning the combustion has the same timing of the measure and, at the end of the phase, it is slightly higher but with a significant improvement. For what matters the latter, all the progresses obtained influenced positively the graph giving a good burn rate with a final total energy in

the chamber inside of the maximum and minimum range made by the experimental data. Indeed, the burn duration error is equal to 1.97% which makes this case acceptable.

This simulation has been run on the 6 cores machines, especially on 6 nodes (36 cores) and it employed 118.12 hours to accomplish three complete cycles.

LHV equal to 55 MJ/kg

The following figures, 5.54, 5.55 and 5.56, shows the results of this specific case.

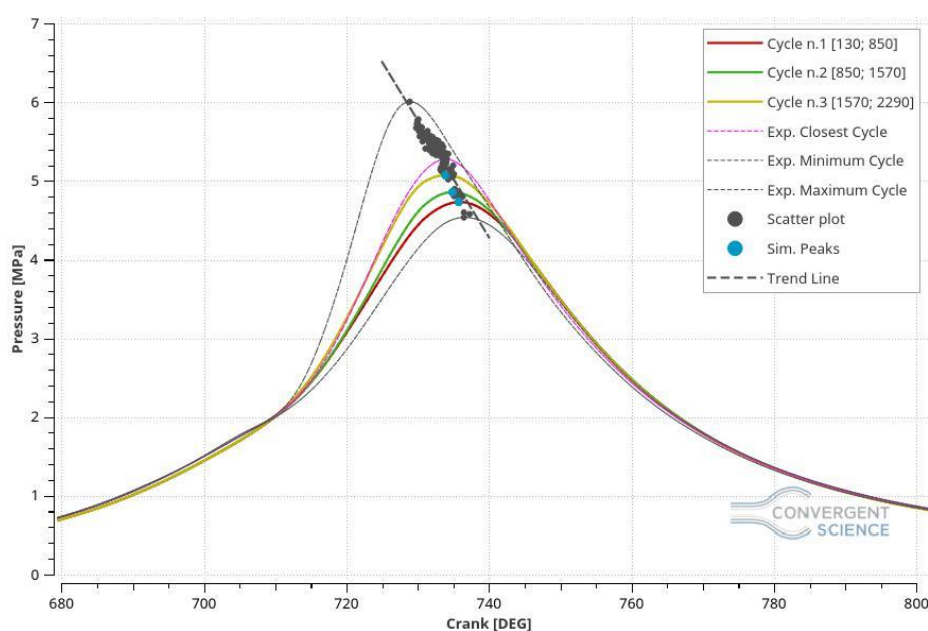


Figure 5.54: Pressure in Cylinder, LHV equal to 55 MJ/kg.

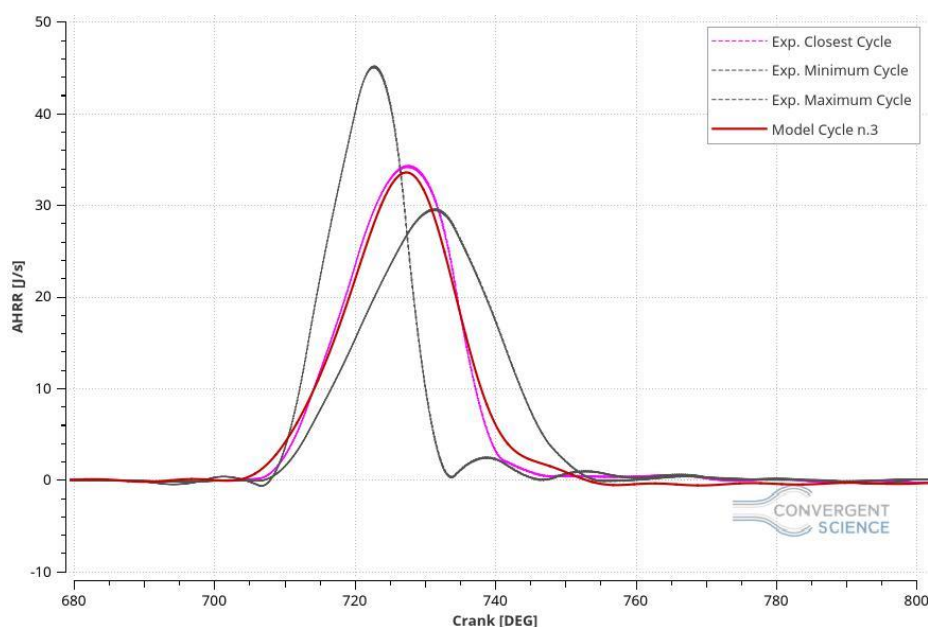


Figure 5.55: AHRR, LHV equal to 55 MJ/kg.

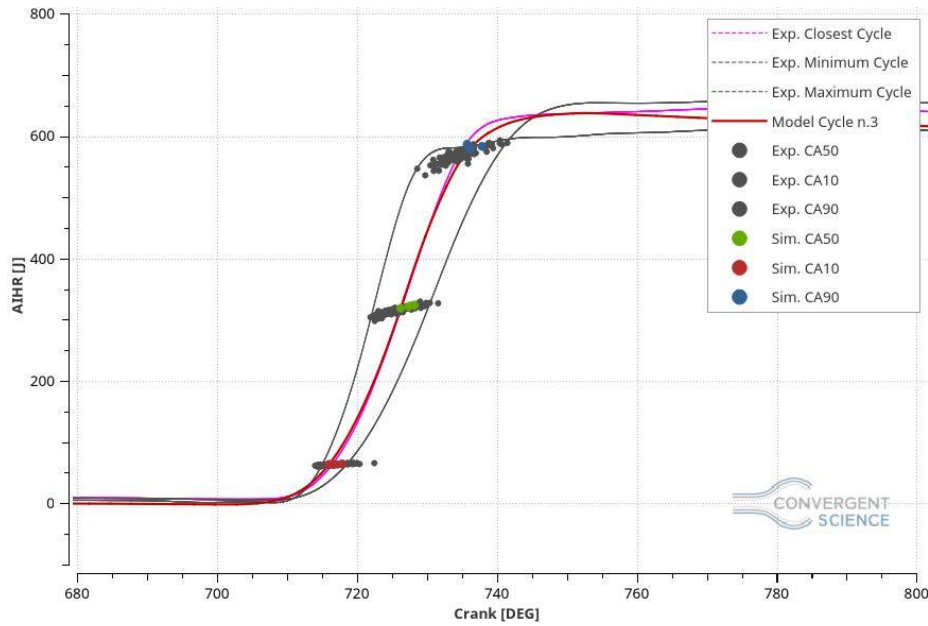


Figure 5.56: AIHR, LHV equal to 55 MJ/kg.

Also for this particular case, is noteworthy the fact that considerably improvements on the pressure curve have been acquired. Specifically, the pressure peak magnitudes are inside of the validity range made by the CCV of the engine and the peak locations stand on the trend line, turning this case into a good agreement. For what matters the tail, it easy to see that it is following the experimental data generating, considering the third cycle as the reference one, an AHRR (figure 5.55) close to match perfectly the experimental reference cycle (closest cycle to the ensemble average). All of those improvements influence remarkably the AIHR curve (figure 5.56), producing a burn rate almost perfect and the total energy found in the chamber entirely inside the range made by the experimental data. Additionally, the trapped mass error inside the cylinder is equal to 0.21% and the burn duration error is 2.01% making this simulation acceptable.

This case has been run on the 6 cores machines, especially on 6 nodes, which means that it has been computed by 36 cores and it employed 116.94 hours to reach completion.

LHV equal to 56 MJ/kg

For what concern this particular case the figures 5.57, 5.58 and 5.59 shows the results achieved.

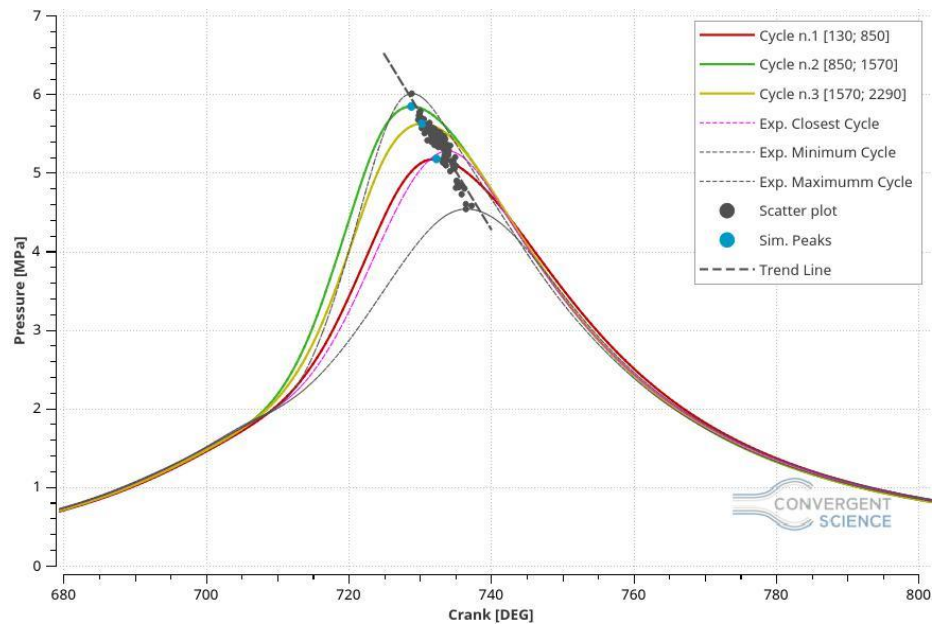


Figure 5.57: Pressure in Cylinder, LHV equal to 56 MJ/kg.

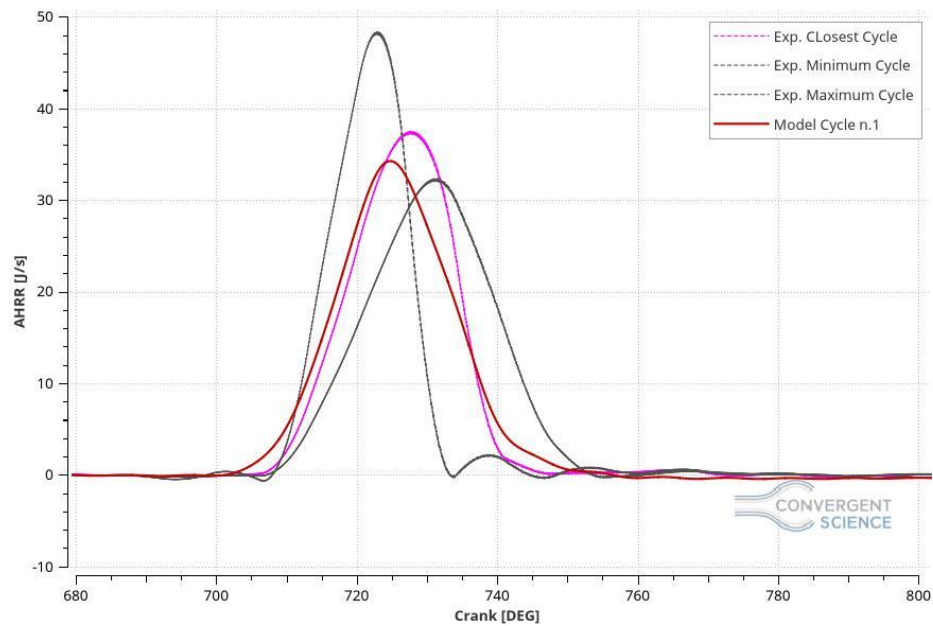


Figure 5.58: AHRR, LHV equal to 56 MJ/kg.

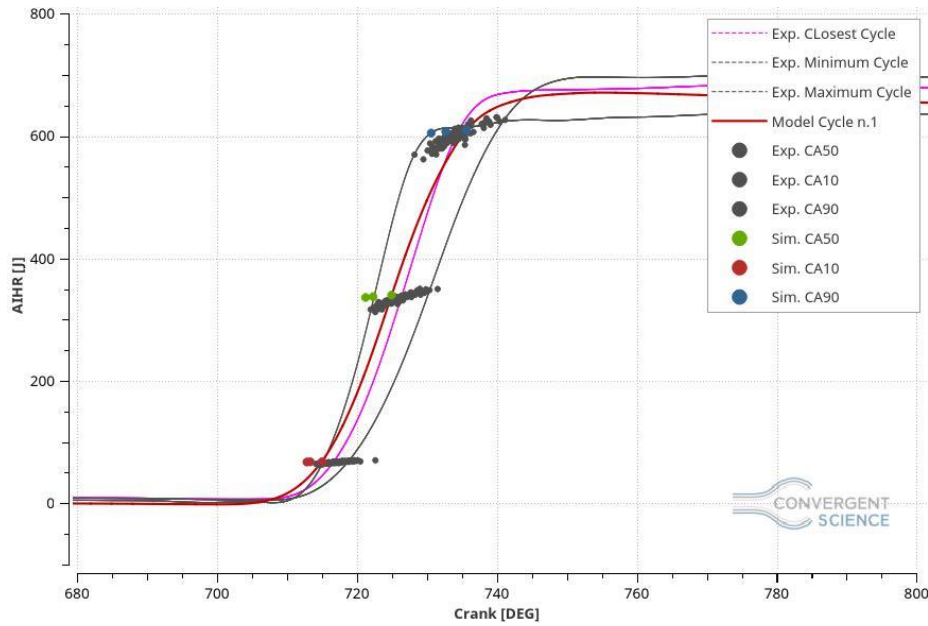


Figure 5.59: AHRR, LHV equal to 56 MJ/kg.

For what concerns this particular case, the pressure trend shows that the energy set as input by means the LHV correction is too high giving overestimated peaks. On the other hand, the pressure peak locations stand on the trend line and they stay inside of the CCV validity range made by the experimental data.

Looking at the AHRR plot, figure 5.58, and considering the first cycle as the reference one, it can be seen that the combustion starts too early, in comparison with the reference experimental cycle, and it lasts too late giving a slightly higher tail. Furthermore, seeing the AHIR plot, figure 5.59, despite the AHRR area is higher than the experimental reference one, the total energy computed is close to be right.

In this case the trapped mass and the burn duration errors obtained are 0.24% and 2.75% respectively. In particular, the burn duration computed is shorter than the experimental data, which means that the combustion is faster in terms of crank angles.

This simulation has been run on the 6 cores machines, especially on 6 nodes and it employed 117.13 hours to reach completion.

Comparisons

In the following pages a comparison between all the LHV correction cases run has been carried out with a brief description of the differences achieved.

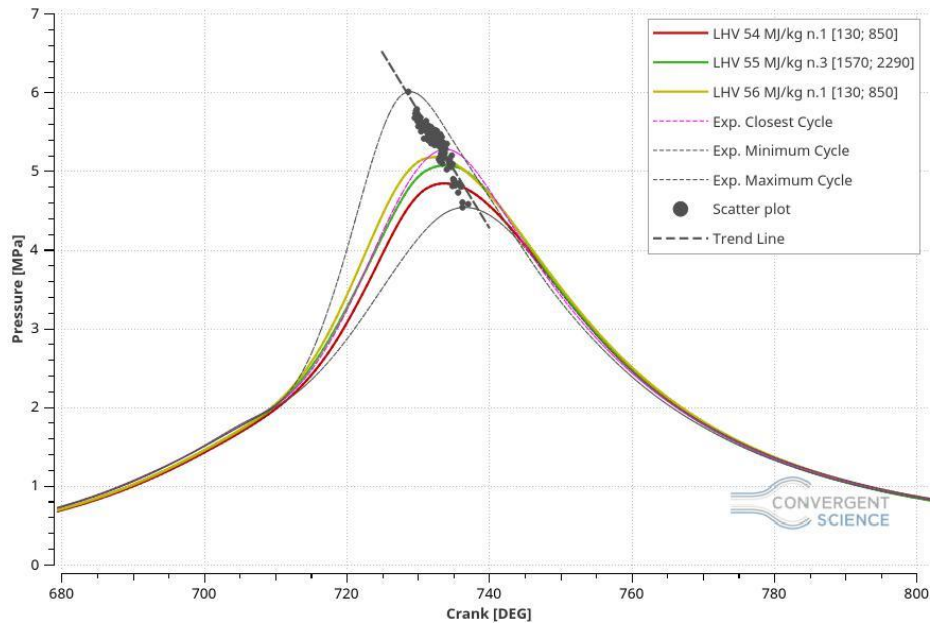


Figure 5.60: Pressure in Cylinder, LHV Comparison.

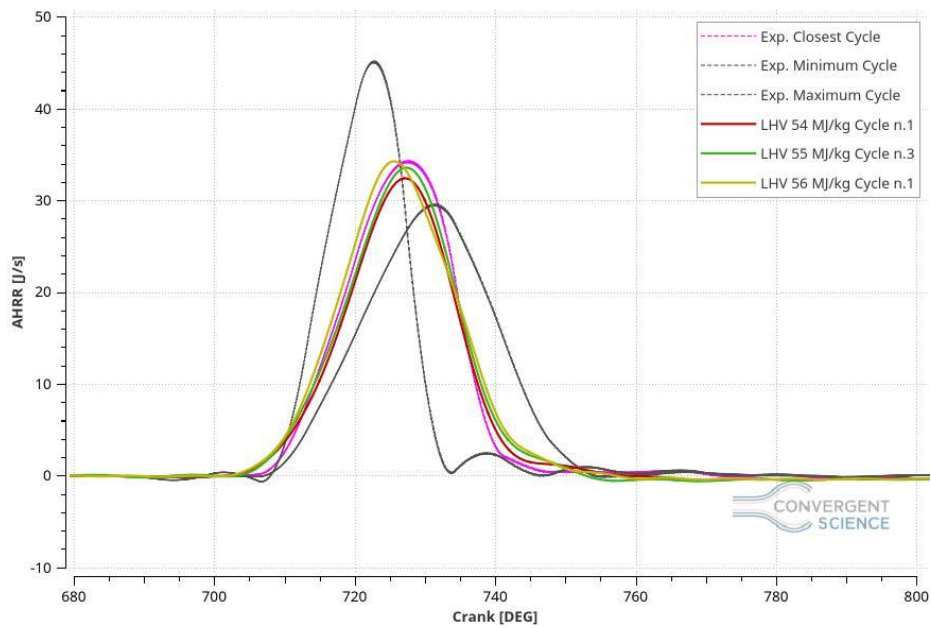


Figure 5.61: AHRR, LHV Comparison.

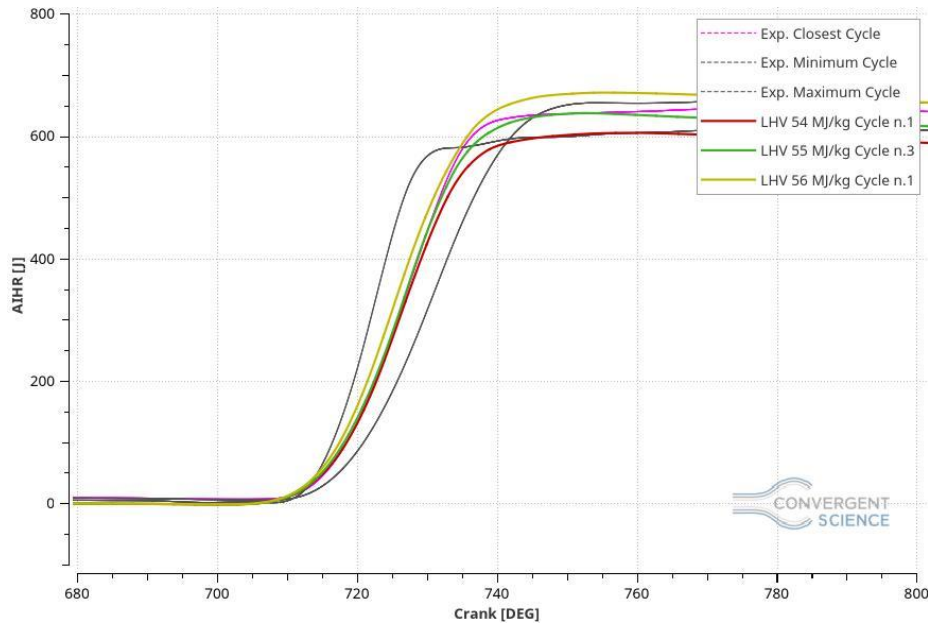


Figure 5.62: AIHR, LHV Comparison.

Focusing on the pressure plot, figure 5.60, noteworthy is the fact that increasing the LHV also the pressure peak tends to increase achieving the maximum value in the case with the LHV equal to 56 MJ/kg. For what concerns the AHRR, figure 5.61, the simulations provide the same phenomenon, also shifting the combustion starting time backwards according with the increase of the LHV. Finally, considering the AIHR, figure 5.62, the total energy in the chamber tends to increase with the LHV, giving, for the 56 MJ/kg case an energy value too high and not acceptable for the aim of this study.

Concluding, this LHV sensitivity made, showed that the LHV computed by the software does not satisfy the measurements, which means that there are some uncertainties on the fuel composition and some future developments need to be done. Basing on those tests, the most correct case might be the one with the LHV equal to 55 MJ/kg which means that the future fuel composition should achieve this energy value to be able to give acceptable results.

5.4 Operating Point 2000x14x1 (NG)

For what matters the operating point 2000[rpm]x14[bar]x1[lambda], all the results obtained will be described in detail, focusing on the modifications made to the standard case setup shown above on the chapter 4. Also In this operating point, the mechanism used is the GRI III. The fuel composition is the natural gas one made by the following species:

- $\text{CH}_4 = 98\%$
- $\text{C}_2\text{H}_6 = 1\%$
- $\text{CO}_2 = 1\%$

5.4.1 Base Simulation

According to the model shown in the chapter 4, a base simulation has been run to understand where and which could be the first modifications to make, in order to obtain the model validation.

The following plots shows the results of this current simulation.

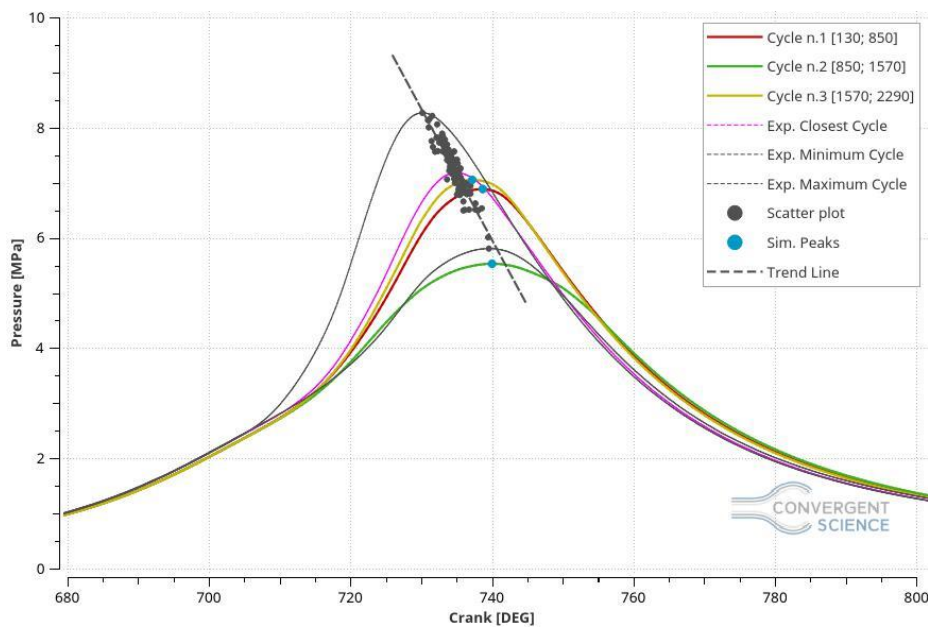


Figure 5.63: Pressure in Cylinder, Base Simulation.

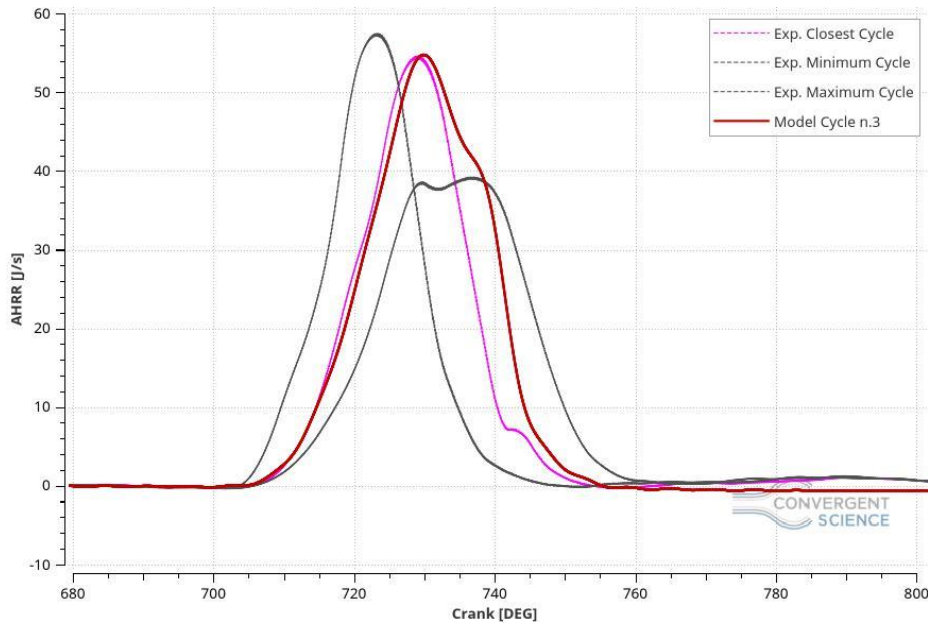


Figure 5.64: AHRR, Base Simulation.

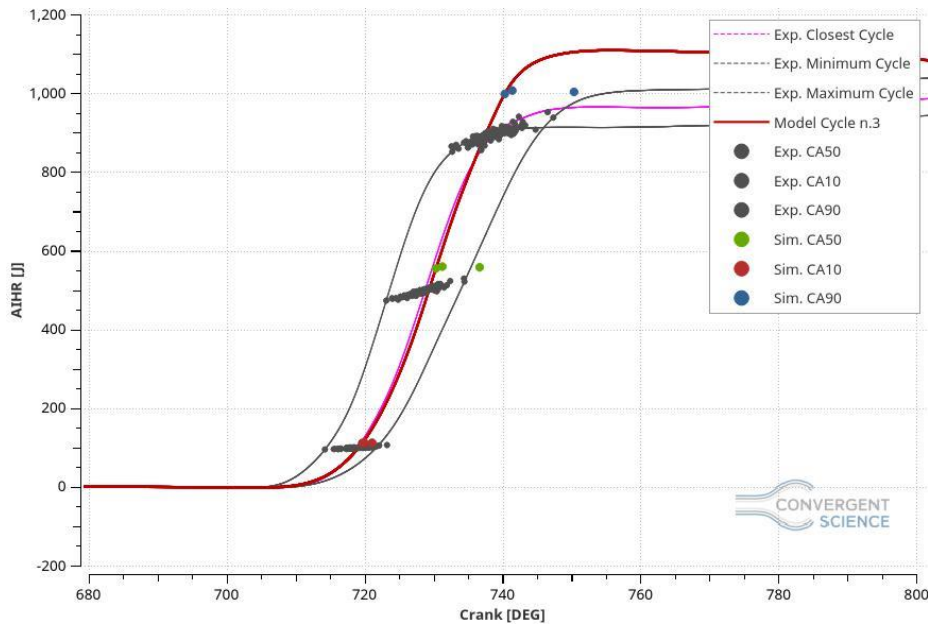


Figure 5.65: AIHR, Base Simulation.

In this operating point, the issues founded are quite similar to the previous one, which means that the peak locations are shifted forward instead backward as before and, in the figure 5.64 and 5.65, it is noteworthy the fact that the energy in the chamber is too high compared to the measurements, even though the trapped mass error is 0.66% higher than the experimental data.

In the figure 5.64, an inflection of the AHRR curve is important to note because it could be affected by the too large pressure curve and a 3D post processing investigation is needed.

Investigating with a 3D post processor (Tecplot software), the figure 5.66 shows the combustion in the chamber of all the three simulation cycles. In the first and the second cycle a combustion anomaly has been exposed in where the flame front is not symmetrical, as in the previous case, but it seems faster on one side instead of the other one. That should be the reason why the combustion seems, suddenly,

decreasing and increasing creating a flection on the AHRR plot. That is only and hypothesis thus other testes must be carried out.

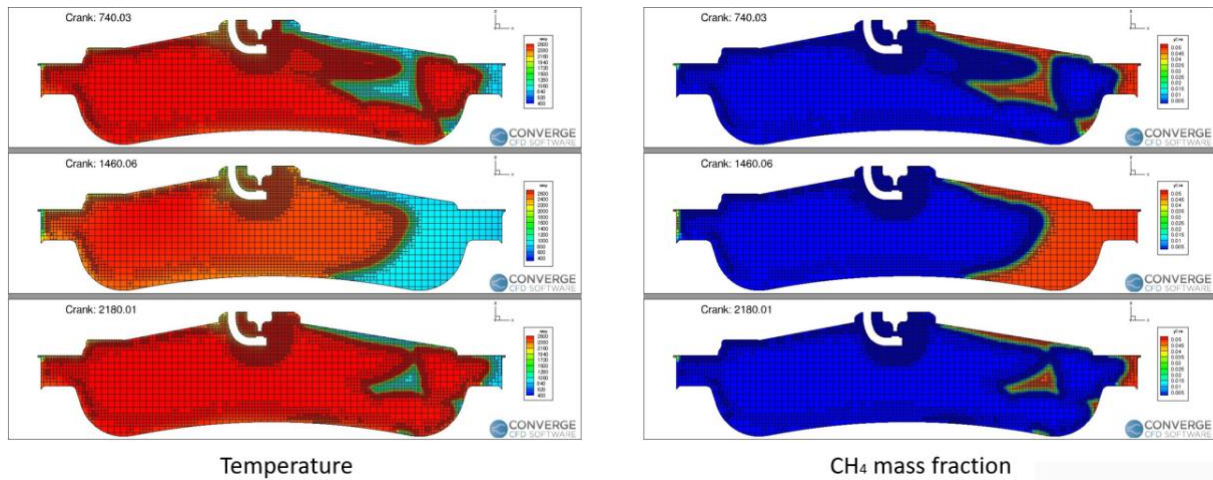


Figure 5.66: Combustion Anomaly in the Camber.

The figure 5.66 also shows the CH_4 mass fraction which is important to understand if the combustion is burning in the correct way and, indeed, the methane mass fraction is following perfectly the same shape of the temperature profile, which means that all the methane is burned and few residues will remain in the chamber. The problem on this figure is the unsymmetrical combustion and, at the same time, the too low burn rate close to the end of the combustion phase which generate the inflection of the AHRR plot.

These notes make some modification fundamental in order to make the model validation possible.

This simulation has been run on 6 nodes with 6 cores each one, which means 36 cores and it employed 117.54 hours to reach completion.

5.4.2 New Boundary Conditions

Following numerous tests and since the current pressure tail is much higher than the previous case, new temperature boundary conditions have been changed basing on the Convergent Science office stuff experience, obtaining the succeeding configuration.

Boundary Name	Old Temperature Value [K]	New Temperature Value [K]
Head	448.81	455
Liner	448.81	410
Piston	448.81	435
Spark Plug	550	750
Spark Plug Electrode	600	800
Inflow	313.78	313.78
Outflow	828	828
Exhaust Port	498.81	800
Exhaust Valve Bottom	498.81	400
Exhaust Valve Angle	498.81	800
Exhaust Valve Top	498.81	800
Intake Port Top	340	340
Intake Port Bottom	340	340
Intake Valve Bottom	340	340
Intake Valve Angle	340	340
Intake Valve Top	340	340

Table 5.1: New Boundary Condition Set.

The following figures show the results of this current simulation.

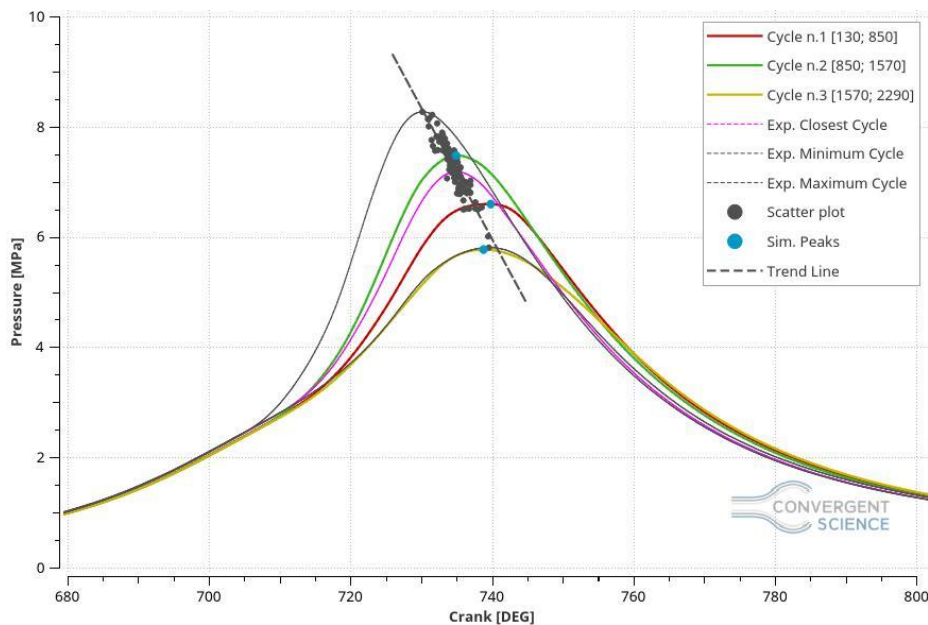


Table 5.67: Pressure in Cylinder, New Boundary Conditions.

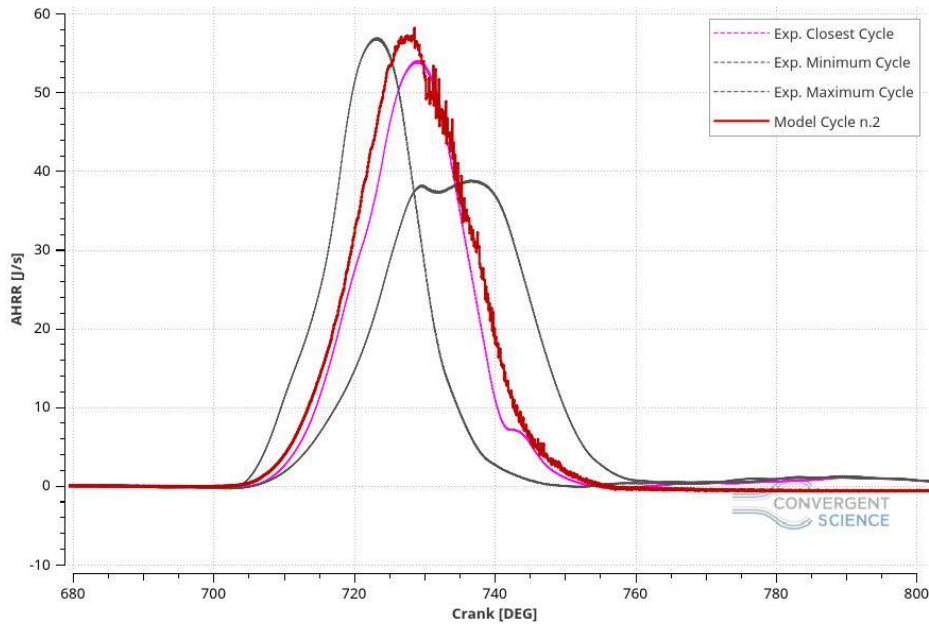


Table 5.68: AHRR, New Boundary Conditions.

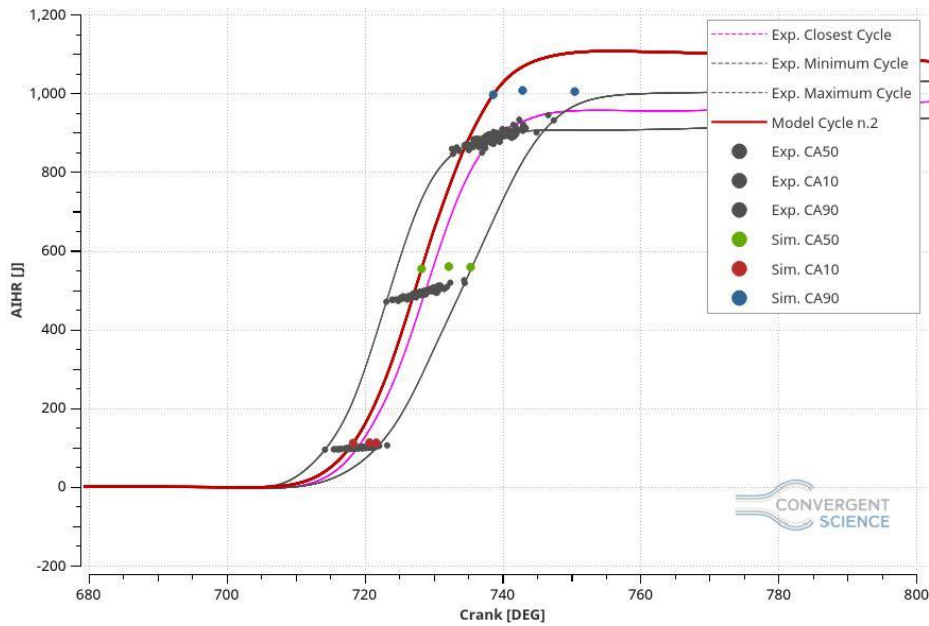


Figure 5.69: AIHR, New Boundary Conditions.

The pressure curve, figure 5.67, shows the pressure in the cylinder and, unfortunately, the boundary condition modification did not display improvement for what concerns the tail of the graph. The peak locations are still shifted even though the peak pressure magnitude is inside of the CCV validity range.

The trapped mass error is 0.08% lower than the measurements, which means that, inside the chamber, there is less mass than the experimental data but the error is almost zero so it has been considered acceptable.

Focusing on the AHRR and AIHR, figure 5.68 and 5.69 respectively, the former shows an improvement because the inflection is almost disappeared and the curve is nearly following the reference cycle (closest cycle to the ensemble average) even if the combustion results faster in the beginning, compared to the measurements, and too long at the end, and it influences badly the integrated heat

release. For what matters the latter, it is easy to see that the energy in the chamber is much higher than the measurements and the CA90 values are higher than the maximum energy value computed by means of the experimental data. The high energy presents in the chamber generates a high burn duration and its error calculation displays that the combustion in the model is 31.12% longer than the measurements in terms of crank angles.

Also on this case, making a 3D post processing, the unsymmetrical combustion anomaly is present and for all of these reasons it has been decided to abandon this case, with a boundary conditions modification, because it did not show relevant improvements.

This simulation has been run on the special cluster on 3 nodes, 60 cores, and the run-time corresponded to 79.17 hours to reach the completion.

5.4.3 Schmidt Number Sensitivity

In order to push back the peak pressure location, a Schmidt Number sensitivity has been run. The aim is to increase the combustion velocity, influenced by the mass diffusivity governed by the Schmidt number itself, to make the shift back of the peak location possible and to decrease the tail in the pressure curve. Generally speaking, if the peak magnitude is increasing, automatically, the tail should decrease giving improvements in the plot. According to the previous case, two additional simulations have been run with the Schmidt Number value equal to 0.75 and 0.70 respectively.

Schmidt Number equal to 0.75

The following plots show the results of this particular case.

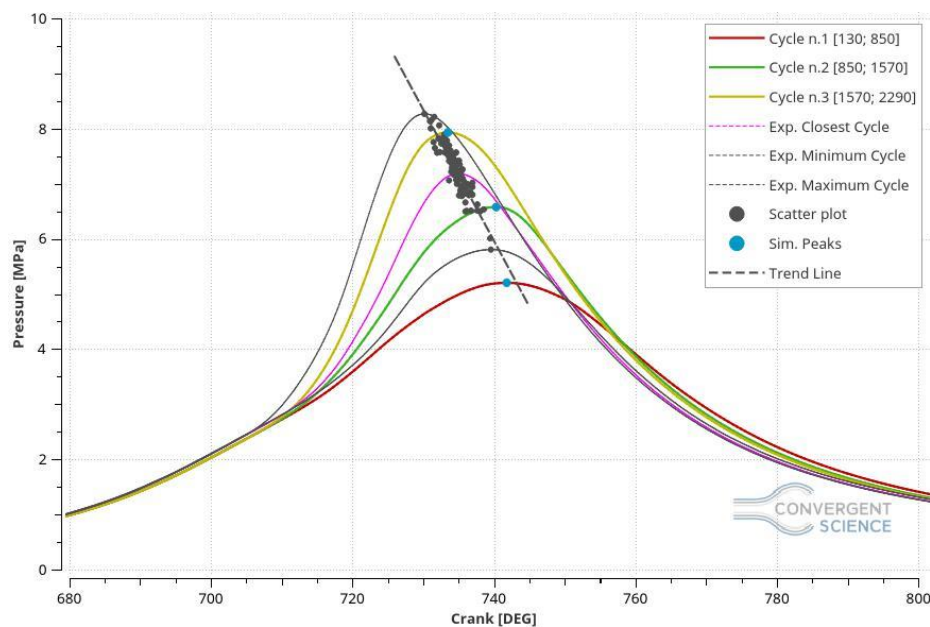


Figure 6.70: Pressure in Cylinder, Schmidt Number equal to 0.75.

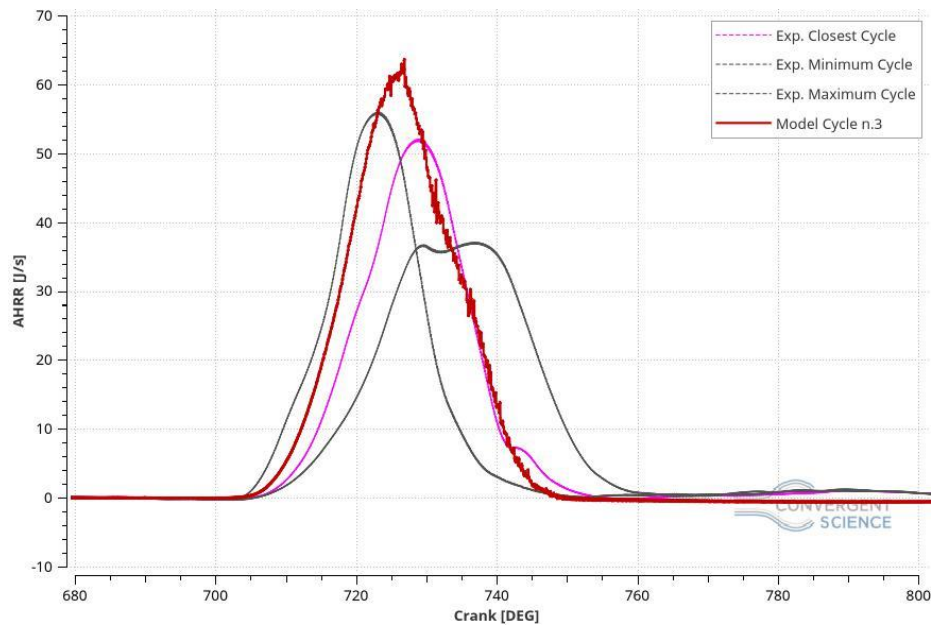


Figure 5.71: AHRR, Schmidt Number equal to 0.75.

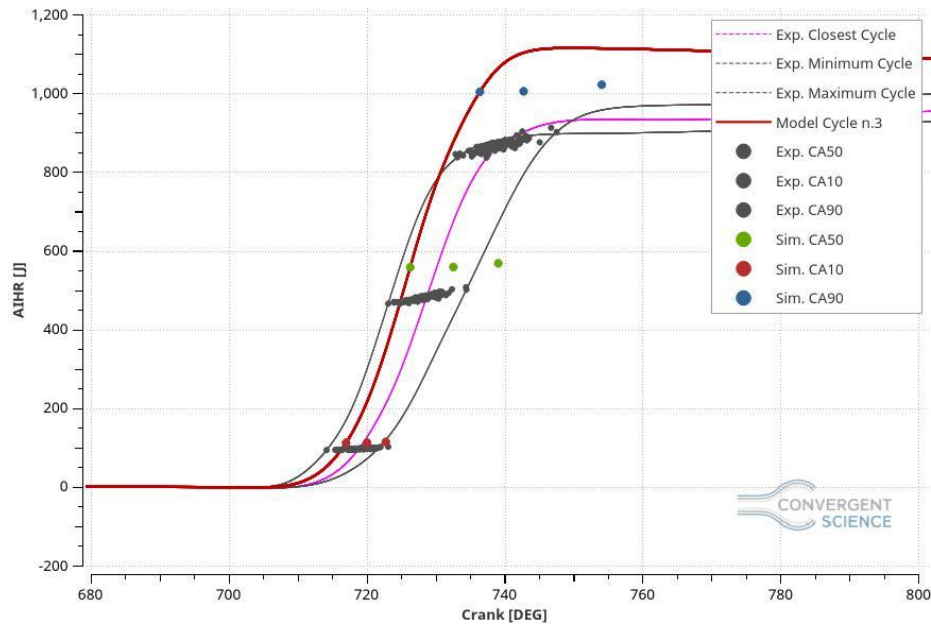


Figure 5.72: AIHR, Schmidt Number equal to 0.75.

Unfortunately, as the figure 5.70 shows, despite the peaks magnitude are increased, there are not improvements on the pressure curve tail. For what concerns the peak locations, they are still shifted and they are not following the trend line despite the trapped mass error is equal to 0.71% lower than measurements.

Considering the third simulation cycle as the best one of this specific case, in the figure 5.71 and 5.72, it easy to see that the energy in the chamber is much higher than the measurements to have the 90% crank angle of the burned mass higher than the maximum cycle of the experimental data. At the same time, the AHRR graph shows that the combustion is too fast in the beginning and it follows the same trend during the end of the phase, making a too long combustion, which influences negatively the burn duration, giving an error equal to 23.29%.

Focusing on the 3D post processing also this case displays an unsymmetrical combustion anomaly but the flection of the AHRR has been reduced considerably.

This simulation has been run on the 6 cores machines, on 6 nodes (36 cores) and it employed 116.68 hours to compute three cycles.

Schmidt Number equal to 0.70

The followings figures show the results of this specific case.

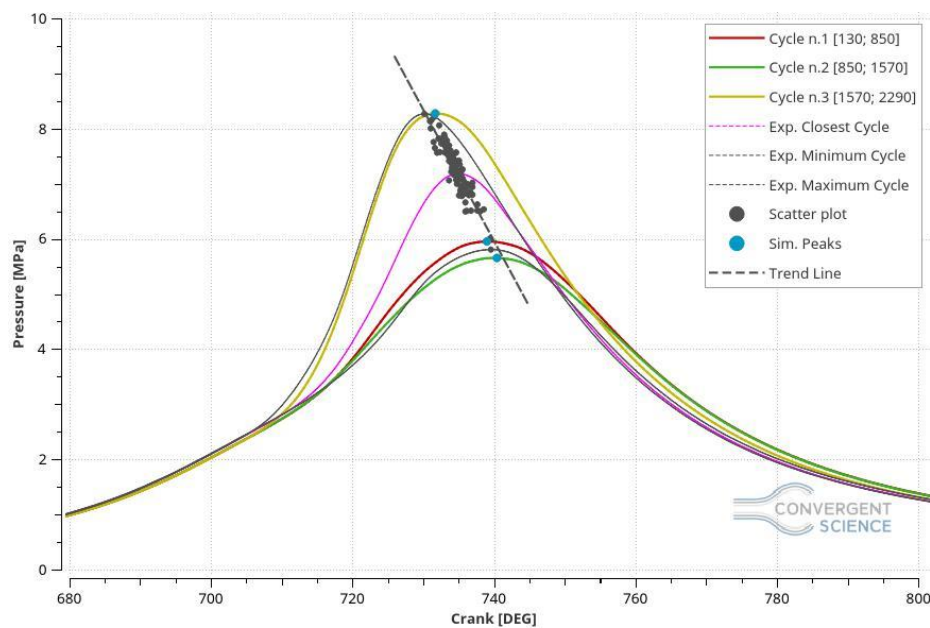


Figure 5.73: Pressure in Cylinder, Schmidt Number equal to 0.70.

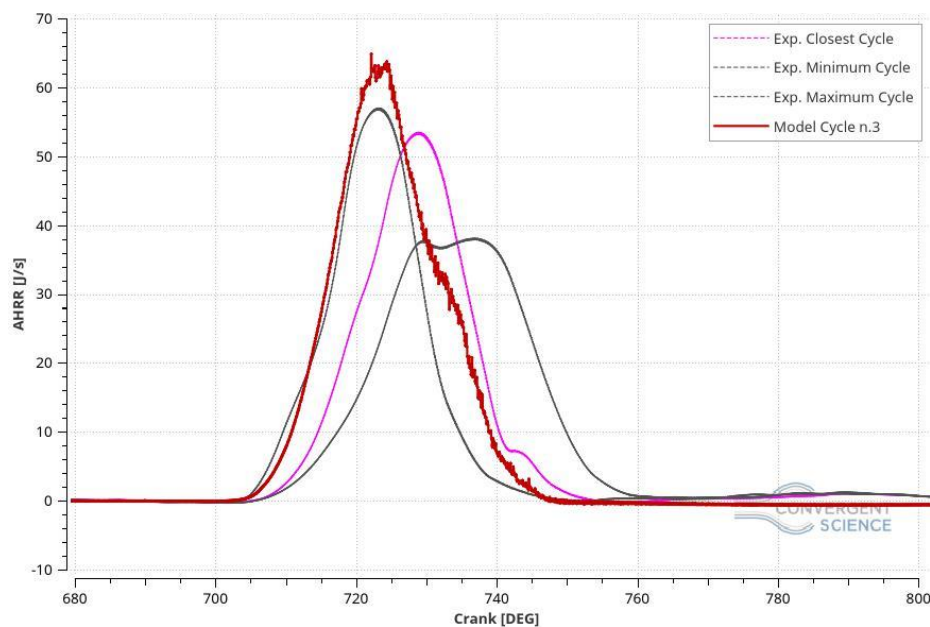


Figure 5.74: AHRR, Schmidt Number equal to 0.70.

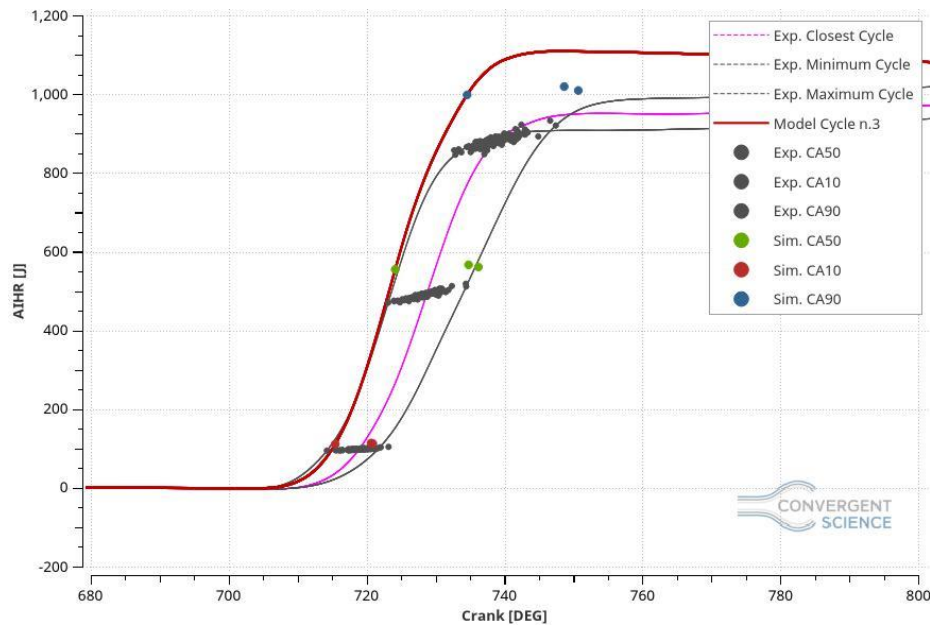


Figure 5.75: AIHR, Schmidt Number equal to 0.70.

This simulation shows some improvements in the pressure peak location but a deterioration of the pressure magnitude. In particular, the pressure magnitude presents an interesting behaviour because the first two cycles introduce a very low-pressure peak value, even if they have the Schmidt number parameter equal to 0.70, and a very high-pressure peak on the third cycle. That phenomenon is surely associated to an uncomplete combustion on the first two cycles that generates a quite important quantity of unburned gases which partially remain in the chamber and, during the third cycle, they burn together giving a faster and more powerful combustion than before.

Also in this case, the trapped mass error is 0.8% lower than the measurements, thus it is acceptable.

Focusing on the AHRR, figure 5.74, is noteworthy the fact that, comparing the model with the closest cycle to the ensemble average, the combustion results faster even than the maximum cycle and it ends with the same flection of the first reference case. That influences badly the integrated heat release, originating a very fast and high AIHR curve which displays a considerably high energy content that cannot be considered acceptable. In addition to this issue, also the burn duration cannot be taken as suitable because the error generated between the simulation and the measurements is equal to 30.73%.

This simulation has been run with the 6 cores machines, especially on 6 nodes, which correspond to 36 cores, and it employed 118.1 hours to complete a three cycles simulation.

Comparison

This comparison has been attempted to understand deeply the differences obtained with the Schmidt Number sensitivity regarding this particular case. The following plots will show the compared results of the closest cycles to the ensemble average of each simulation.

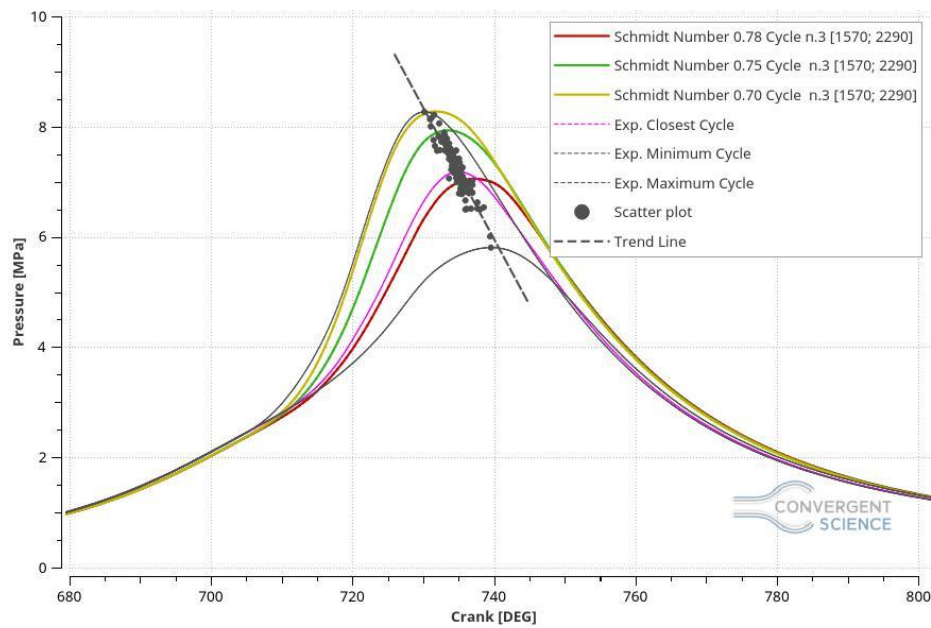


Figure 5.76: Pressure in Cylinder, Schmidt Number Sensitivity Comparison.

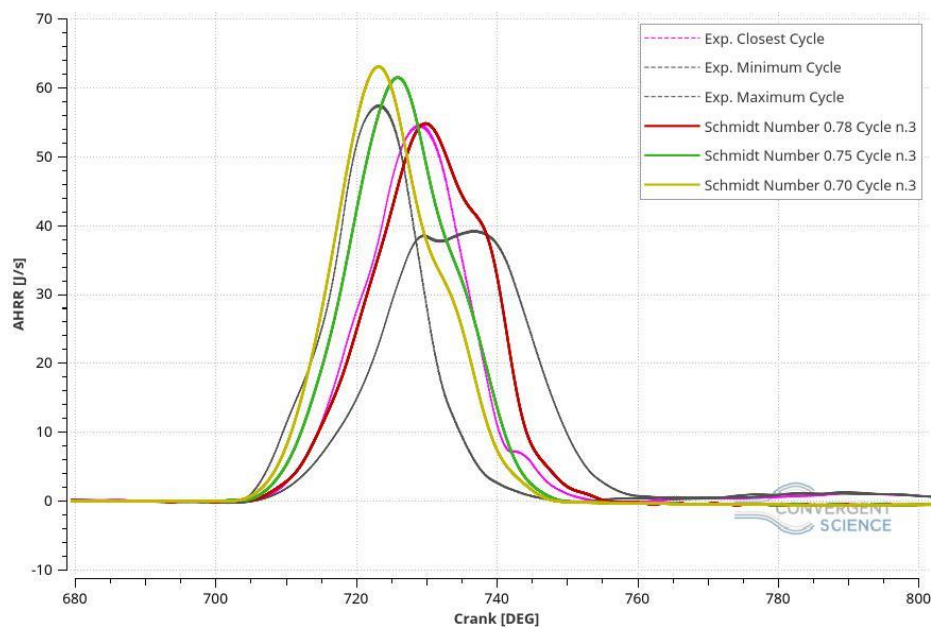


Figure 5.77: AHRR, Schmidt Number Sensitivity Comparison.

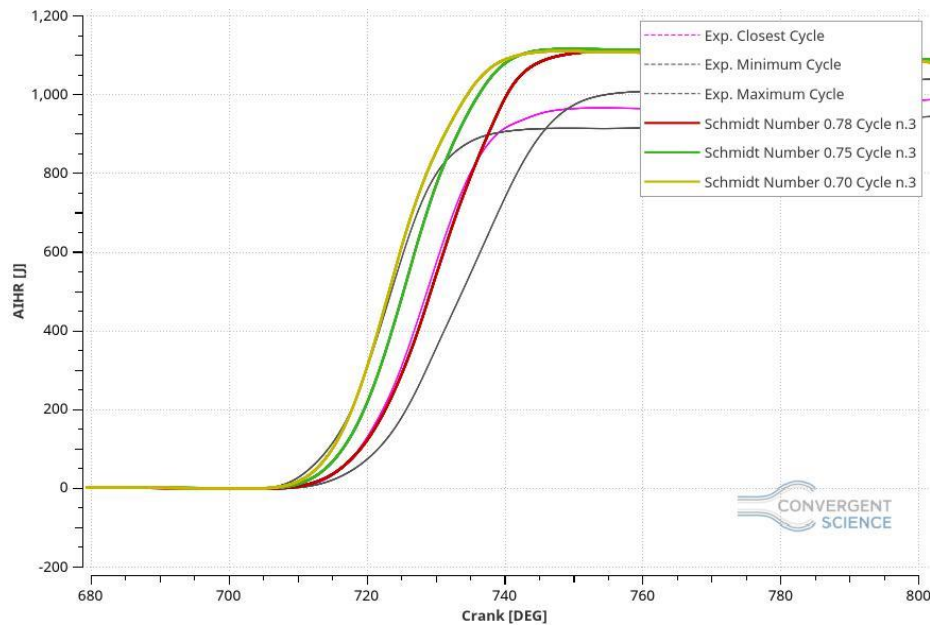


Figure 5.78: AIHR, Schmidt Number Sensitivity Comparison.

For what concern the pressure plot, figure 5.76, the decrease of the Schmidt Number value, as expected, increasing the mass diffusivity, rises the combustion velocity originating higher pressure peaks. The aim was to increase the pressure peak consequently obtaining a reduction of the pressure plots tail but, as the figure shows, it does not give advances and the motivation should be connected only on the combustion anomaly, presented before, that generates a too long combustion.

Moreover, the AHRR and the AIHR plots, figure 5.77 and 5.78, show an improvement regarded to the flection present at the end of the combustion but a deterioration in terms of combustion velocity originating a combustion faster and faster increasing the Schmidt Number. Obviously, this behaviour affects the AIHR negatively giving a too fast combustion with too much energy that makes these cases not acceptable.

For all these reasons, these cases have been abandoned to replace them with new ones where the modifications introduced give more relevant improvements.

5.4.4 LHV Correction

After several tests, the LHV correction, also for this operating point, has been carried out. The aim, since there are some uncertainties on the current fuel composition, is to reduce the total energy in the chamber to provide a lower pressure tail and come closer to the experimental data. This correction should also improve the AHRR and the AIHR turning this case into a good agreement. As in the previous case the LHV computed by CONVERGE was equal to 50,12 MJ/kg which is too high because it generates a too powerful combustion giving results that overestimate the measurements.

Many NG LHVs have been found in literature and the one who fits almost perfectly to this particular case is equal to 47.141 MJ/kg, consequently a simulation with this value has been run.

The following figures shows the results achieves regarding this specific case.

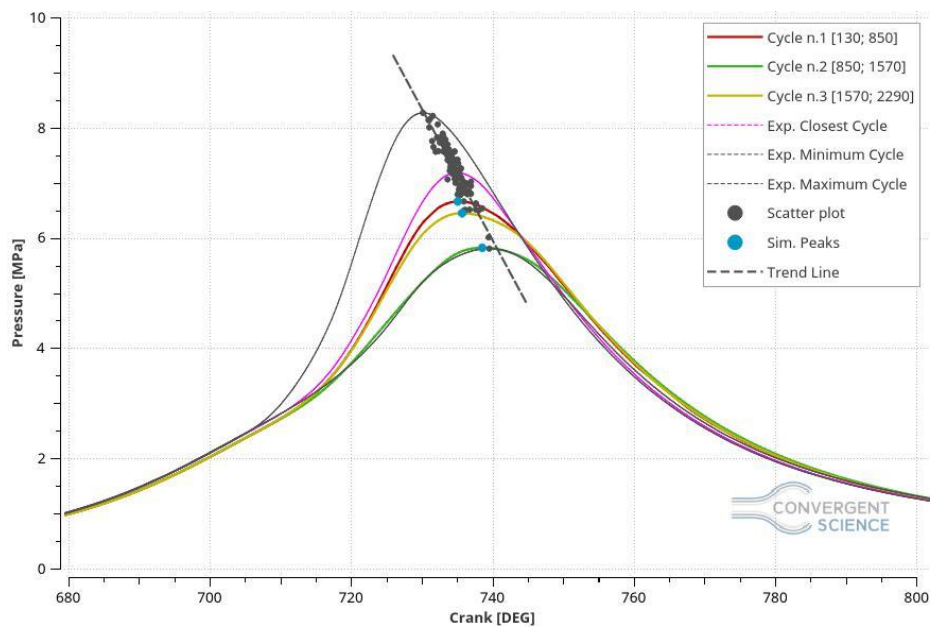


Figure 5.79: Pressure in Cylinder, LHV Correction.

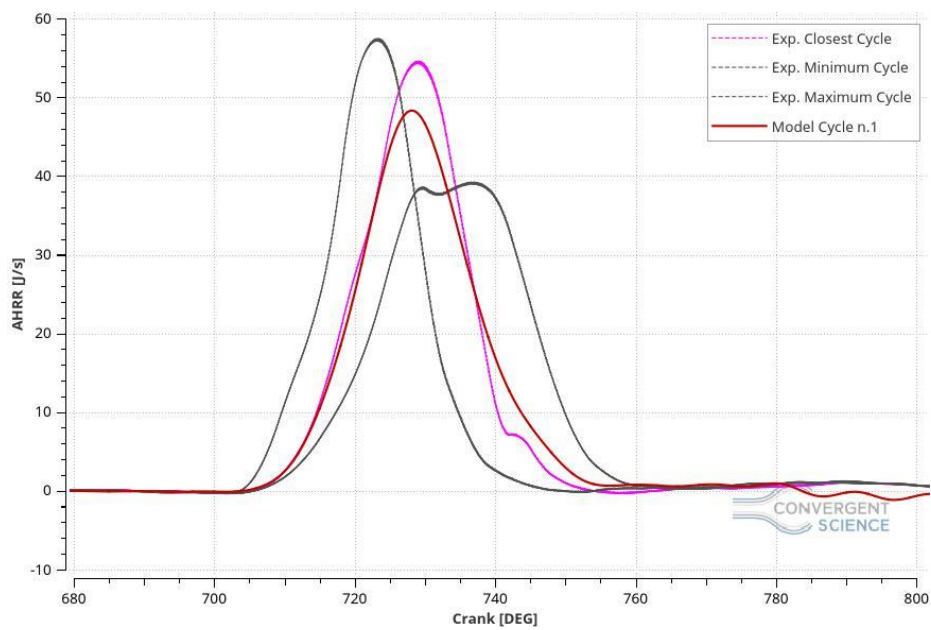


Figure 5.80: AHRR, LHV Correction.

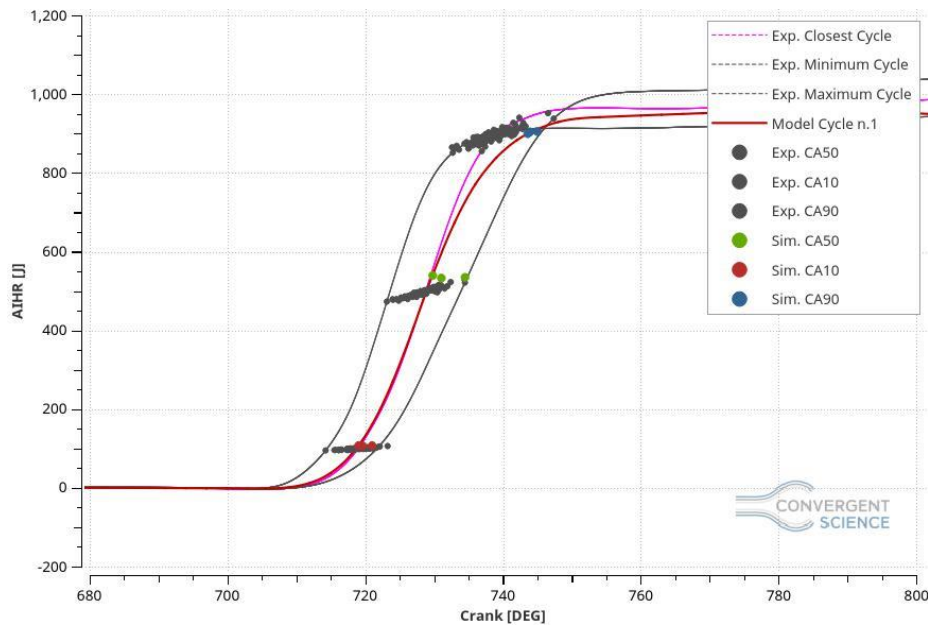


Figure 5.81: AIHR, LHV Correction.

Considering the pressure plot, figure 5.79, a remarkable improvement can be noticed on the pressure tail which is reduced considerably giving results closer to the measurements. For what concern the pressure peak locations, they are closer to the trend line, in comparison with the previous simulation, which can be considered a significant improvement.

Focusing on the AHRR, figure 5.80, it is easy to see that the combustion starts with the same time of the reference cycle and it last with a slightly high tail giving a remarkable development as well. Making the integration of this plot, obtaining the AIHR, figure 5.81, the burn rate achieved is almost matching the experimental data giving a total energy in the combustion chamber inside of the range made by the measurements.

Finally, the trapped mass and burn duration errors for this particular case are 0.15% and 4.66% respectively turning this result in a good agreement even if some improvements can still be carried out.

This simulation has been run on the 6 cores machines, especially on 6 nodes (36 cores) and it employs 118.11 hours to reach completion.

6. Conclusions and Future Developments

In this thesis work many CFD simulations has been carried out, more than 130, whom gave the opportunity to increase the knowledge in SAGE-Detailed Chemistry Model and in all what concerns the CONVERGE CFD software, which is able to simulate all the conditions regarded the combustion of natural gas engines.

The model validation has been carried out on three different operating points, especially two of them with natural gas fuel supply and one of them with the adding of 15% of hydrogen in volume in the fuel composition. The Gas-on aim is to study a way to reduce the emissions of engines, thus the technique of adding hydrogen in the fuel mixture is one of the fundamental concepts of this project and the model validation, of the operating points treated, is a natural step which separates the theoretical concept to the real application in the everyday life.

Several issues have been found during the model validations which have been solved with many different approaches like, a mesh sensitivity, with different reaction mechanism, such as GRI III and USC, Schmidt Number sensitivities and LHV corrections. All these approaches showed more or less the same problem which can be associated to some uncertainties in the fuel composition in all of the operating points analysed.

For what concerns the operating point 4600x7.9x1 with a NG fuel supply, the model validation has been carried out with a final simulation characterised by a Schmidt Number equal to 0.75, which helped the pressure peak magnitudes and locations increasing the combustion rate and with the addition of an LHV correction based on a value found in literature, which corrects the fuel total energy turning that case into a good agreement able to predict the engine behaviour regarded this particular operating point.

For what matters the operating point 4600x7.9x1 with a NG + 15% of hydrogen in the fuel supply, the same issue of fuel composition has been found with a strongly dependents on the hydrogen mass in the chamber which gives a too powerful combustion that is not able to match the experimental data. Since in literature is quite impossible to find an LHV with the current fuel composition made by NG and Hydrogen, it has been decided to proceed with and LHV sensitivity, as a final test, in order to better understand which could be the influence of a lower LHV in the engine behaviour. The results accomplished showed that a lower LHV give better results in terms of pressure peak magnitude, pressure peak location and burning duration error turning this case into a good agreement. The best case run is the one with an LHV equal to 55 MJ/kg which cannot be considered real because it has been found by means a weighted average between LHV of NG and hydrogen, which means that it is not a valid value but just a theoretical one. Moreover, this case can be considered a base of future developments on the fuel composition which should give an LHV equal to 55 MJ/kg to be sure that the results will match the experimental data without further improvements. Another useful development could be a research of a new reaction mechanism which fits perfectly with a dual fuel, as this particular case, instead a mechanism which is based on just one fuel.

Finally, considering the last operating point 2000x14x1 with a NG fuel supply, the same uncertainty in the fuel composition has been found and it has been solved with an LHV correction, as the first case, which gave remarkable improvements in terms of pressure peak magnitudes, pressure peak locations

and burn duration error turning this case into a good agreement. Unfortunately, for what concerns this particular case, considerably improvements have been carried out but the pressure tail and the CA10, CA50 and CA90 locations (which are the 10%, 50% and 90% of the burned mass in the combustion chamber in terms of crank angles) are still not perfect and future developments might be accomplished to be able to consider this model validated and predictable.

In order to follow the main project idea, a fundamental future development might be to increase the percentage of hydrogen in the fuel composition to be able to reduce further the engine carbon emissions to a lower level or completely erase them using 100% of hydrogen as a fuel supply.

Furthermore, an interesting idea might be also checking the emissions of this engine in terms of CO, NO_x, HC and other type of pollutants, to analyse the differences and the improvements by using a mixture of natural gas and hydrogen until the complete erase of fossil fuels by means the usage of pure hydrogen. This future development might give interesting results that could revolutionize all the engine and transportation world turning these fundamentals technologies into a green and environmentally friendly machines that would decrease, or maybe completely eliminate, the air pollution in every part of the world.

Acknowledgements

I would like to gratitude all the people who helped and supported me during my studies and my thesis work bringing it to reality. Firstly, I would like to extend my gratitude to my supervisor at Convergent Science GmbH, Dr. Rainer Rothbauer for giving me the great opportunity to join this company as trainee, for giving me the access to all the equipment, technologies and tools which allowed me to realize this thesis project, to grow up from the personal point of view and to improve my knowledge. I would also like to thank my supervisor at the Politecnico di Torino, Prof. Daniela Misul for giving me the occasion to work on this project and the opportunity to make such an amazing experience. A truthful thank you to my co-supervisor Prof. Mirko Baratta for all his patience, the helpful suggestions, assistance and, sometimes, to cheer me up.

I would also like to acknowledge all the Convergent Science team: Lorenzo, Jyothish, Pietro, Matteo, Suresh, Ivona, Vera, Veera, Riccardo, Edith and Bugra who they really helped me by supporting and enduring me.

To my mother Paola, my father Flavio and my brother Nicolò who, with their tireless support, both moral and economic, they allowed me to end my studies, contributing to my personal training.

Thanks to all of my friends for sharing the most important experiences with me and to have and important weight in my life.

Acronyms

A/F: Air to Fuel ratio;

AHRR: Apparent Heat Release Rate;

AMR: Adaptive Mesh Refinement;

BC: Boundary Conditions;

BDC: Bottom Dead Center;

CAD: Crank Angle Degree;

CA10: Crank Angle which 10% of mass is burned;

CA50: Crank Angle which 50% of mass is burned;

CA90: Crank Angle which 90% of mass is burned;

CCV: Cycle to Cycle Variability;

CEQ: Chemical Equilibrium;

CFD: Computational fluid dynamics;

CI: Compression Ignition engine;

CNG: Compressed Natural Gas;

CRF: Centro Ricerche Fiat;

CTC: Characteristic Time Combustion;

DENERG: Dipartimento di Energia of Politecnico di Torino;

DNS: Direct Numerical Simulation;

ECFM: Extended Coherent Flame Model;

ECFM3Z: Extended Coherent Flame Model with 3Z mixing model;

EVC: Exhaust Valve Closing;

EVO: Exhaust Valve Opening;

FGM: Flamelet Generation Manifold;

FIAT: Fabbrica Italiana Automobili Torino;

GRI: Gas Research Institute;

HR: Heat Release;

HRR: Heat Release Rate;

ICE: Internal Combustion Engine;

IHR: Integrated Heat Release;

IVC: Intake Valve Closing;

IVO: Intake Valve Opening;

LES: Large Eddy Simulation;

LHV: Low Heat Value;

NG: Natural Gas;

RANS: Reynolds Average Navier Stokes equation;

RIF: Representative Interactive Flamelet;

RPM: Revolution per Minute;

SA: Spark Advance;

SI: Spark Ignition engine;

STL: Standard Triangulation Language;

TDC: Top Dead Center;

TDMS: Technical Data Management Streaming;

TKE: Turbulent Kinetic Energy;

List of Figures

- Figure 2.1:** Stress components in the x-direction;
- Figure 2.2:** Examples of Fixed Embedding;
- Figure 2.3:** Adaptive Mesh Refinement (AMR) examples;
- Figure 3.1:** Engine on the test bench;
- Figure 3.2:** 4600x7.9 CH₄, Experimental Pressure plot;
- Figure 3.3:** Experimental Data zoom on the pressure peaks;
- Figure 3.4:** 4600x7.9 CH₄+H₂, Experimental Pressure plot;
- Figure 3.5:** Experimental Data zoom on the Pressure peaks;
- Figure 3.6:** 2000x14 CH₄, Experimental Pressure plot;
- Figure 3.7:** Experimental Data zoom in the Pressure peaks;
- Figure 4.1:** Engine Geometry;
- Figure 4.2:** Engine Regions;
- Figure 4.3:** GRI-Mech 3.0 partial mech.dat file;
- Figure 4.4:** GRI-Mech 3.0 partial therm.dat file;
- Figure 4.5:** GRI-Mech 3.0 partial transport.dat file;
- Figure 4.6:** Source Model;
- Figure 4.7:** Ignition model on the spark plug;
- Figure 5.1:** Pressure in Cylinder, Base simulation;
- Figure 5.2:** Pressure in Cylinder, Base simulation zoom;
- Figure 5.3:** AHRR, Base simulation;
- Figure 5.4:** AIHR, Base simulation;
- Figure 5.5:** Pressure in Cylinder with Boundary Conditions increased;
- Figure 5.6:** Pressure in Cylinder with Boundary Conditions increased zoom;
- Figure 5.7:** AHRR with Boundary Conditions increased;
- Figure 5.8:** AIHR with Boundary Conditions increased;
- Figure 5.9:** Pressure in Cylinder, SGS equal to 2 m/s;
- Figure 5.10:** AHRR, SGS equal to 2 m/s;
- Figure 5.11:** AIHR, SGS equal to 2 m/s;
- Figure 5.12:** Pressure in Cylinder, SGS equal to 1 m/s;

Figure 5.13: AHRR, SGS equal to 1 m/s;

Figure 5.14: AIHR, SGS equal to 1 m/s;

Figure 5.15: Mesh Sensitivity Pressure Comparison;

Figure 5.16: Mesh Sensitivity AHRR Comparison;

Figure 5.17: Mesh Sensitivity AIHR Comparison;

Figure 5.18: Turbulence Magnitude Comparison;

Figure 5.19: Cells in the domain;

Figure 5.20: Pressure in Cylinder, Schmidt Number equal to 0.75;

Figure 5.21: AHRR, Schmidt Number equal to 0.75;

Figure 5.22: AIHR, Schmidt Number equal to 0.75;

Figure 5.23: Pressure in Cylinder, Schmidt Number equal to 0.70;

Figure 5.24: AHRR, Schmidt Number equal to 0.70;

Figure 5.25: AIHR, Schmidt Number equal to 0.70;

Figure 5.26: Schmidt Number Sensitivity, Pressure Comparison;

Figure 5.27: Schmidt Number Sensitivity, AHRR Comparison;

Figure 5.28: Schmidt Number Sensitivity, AIHR Comparison;

Figure 5.29: Pressure in Cylinder, Reaction Multiplier equal to 1.05;

Figure 5.30: AHRR, Reaction Multiplier equal to 1.05;

Figure 5.31: AIHR, Reaction Multiplier equal to 1.05;

Figure 5.32: Pressure in Cylinder, Reaction Multiplier equal to 1.1;

Figure 5.33: AHRR, Reaction Multiplier equal to 1.1;

Figure 5.34: AIHR, Reaction Multiplier equal to 1.1;

Figure 5.35: SAGE Reaction Multiplier Sensitivity, Pressure Comparison;

Figure 5.36: SAGE Reaction Multiplier Sensitivity, AHRR Comparison;

Figure 5.37: SAGE Reaction Multiplier Sensitivity, AIHR Comparison;

Figure 5.38: Pressure in Cylinder, LHV Correction;

Figure 5.39: AHRR, LHV Correction;

Figure 5.40: AIHR, LHV Correction;

Figure 5.41: Pressure in Cylinder, Base Simulation;

Figure 5.42: Compression Phase zoom, Base Simulation;

Figure 5.43: AHRR, Base Simulation;

Figure 5.44: AIHR, Base Simulation;

Figure 5.45: Pressure in Cylinder, USC Mechanism;

Figure 5.46: AHRR, USC Mechanism;

Figure 5.47: AIHR USC Mechanism;

Figure 5.48: Pressure in Cylinder, Boundary Conditions Manipulation;

Figure 5.49: AHRR, Boundary Condition Manipulation;

Figure 5.50: AIHR, Boundary Condition Manipulation;

Figure 5.51: Pressure in Cylinder, LHV equal to 54 MJ/kg;

Figure 5.52: AHRR, LHV equal to 54 MJ/kg;

Figure 5.53: AIHR, LHV equal to 54 MJ/kg;

Figure 5.54: Pressure in Cylinder, LHV equal to 55 MJ/kg;

Figure 5.55: AHRR, LHV equal to 55 MJ/kg;

Figure 5.56: AIHR, LHV equal to 55 MJ/kg;

Figure 5.57: Pressure in Cylinder, LHV equal to 56 MJ/kg;

Figure 5.58: AHRR, LHV equal to 56 MJ/kg;

Figure 5.59: AIHR, LHV equal to 56 MJ/kg;

Figure 5.60: Pressure in Cylinder, LHV Comparison;

Figure 5.61: AHRR, LHV Comparison;

Figure 5.62: AIHR, LHV Comparison;

Figure 5.63: Pressure in Cylinder, Base Simulation;

Figure 5.64: AHRR, Base Simulation;

Figure 5.65: AIHR; Base Simulation;

Figure 5.66: Combustion Anomaly in the Chamber;

Figure 5.67: Pressure in Cylinder, New Boundary Conditions;

Figure 5.68: AHRR, New Boundary Conditions;

Figure 5.69: AIHR, New Boundary Conditions;

Figure 5.70: Pressure in Cylinder, Schmidt Number equal to 0.75;

Figure 5.71: AHRR, Schmidt Number equal to 0.75;

Figure 5.72: AIHR, Schmidt Number equal to 0.75;

Figure 5.73: Pressure in Cylinder, Schmidt Number equal to 0.70;

Figure 5.74: AHRR, Schmidt Number equal to 0.70;

Figure 5.75: AIHR, Schmidt Number equal to 0.70;

Figure 5.76: Pressure in Cylinder, Schmidt Number Sensitivity Comparison;

Figure 5.77: AHRR, Schmidt Number Sensitivity Comparison;

Figure 5.78: AIHR, Schmidt Number Sensitivity Comparison;

Figure 5.79: Pressure in Cylinder, LHV Correction;

Figure 5.80: AHRR, LHV Correction;

Figure 5.81: AIHR, LHV Correction;

List of Tables

Table 3.1: Engine Main Characteristics;

Table 3.2: Operating Points Considered;

Table 4.1: Boundary Names and Assignment;

Table 4.2: Temperature Boundary Conditions;

Table 4.3: Fixed Embedding Settings;

Table 4.4: Adaptive Mesh Refinements (AMR) Settings;

Table 5.1: New Boundary Conditions set;

Bibliography

- [1] "An Introduction To Computational Fluid Dynamics: The Finite Volume Method"; Second edition; H. K. VERSTEEG, W. MALALASEKERA;
- [2] "Computational Methods for Fluid Dynamics"; 3rd edition; J.H. FERZIGER, M. PERIC;
- [3] "Motori a combustione interna" G. Ferrari. Il Capitello, 1996;
- [4] "Internal Combustion engines Fundamentals" John B. Heywood McGraw-Hill. Inc. 1998;
- [5] "An Introduction to Combustion: Concepts and Applications", Stephen R. Turns, Second edition, McGraw-Hill Higher Education;
- [6] "CONVERGE v2.3 Manual" Richards, K. J. Senecal, P. K., and Pomraning, E., Convergent Science, Inc., Madison, WI (2017);
- [7] "Computational Fluid Mechanics and Heat transfer", Third edition, Richard H. Pletcher, John C. Tannehill, Dale A. Anderson;
- [8] "Combustion modelling of a NG engine using detailed chemistry in CONVERGE" Lorenzo Testa, Master thesis, Politecnico di Torino;
- [9] "3D-CFD Simulation of Combustion Process in a NG Engine by Adopting a LFS Submodel from Detailed Kinetic Mechanism", Prashant Goel, Master's thesis, Politecnico di Torino;
- [10] "Simulation of the ensemble and cycle-resolved combustion process in a NG-H2 engine", Paolo De Angelis, Master's thesis, Politecnico di Torino;
- [11] "<https://en.wikipedia.org/wiki/Combustion>" 2018;
- [12] "Propulsori termici notes" Federico Millo, 2018;
- [13] "Evaluation of Burn Rate Routines and Analysis Errors". In: SAE Technical Paper. 970037. SAE International, Feb. 1997, Michael F. J. Brunt and Andrew L. Emtage;